Title
Synthesis and Characterization of Colloidal Quantum Dot Ensembles with Near-Unity Photoluminescent Quantum Yields

Author
Koscher, Brent Aaron

Publication Date
2019

Peer reviewed|Thesis/dissertation

Synthesis and Characterization of Colloidal Quantum Dot Ensembles with Near-Unity Photoluminescent Quantum Yields

By

Brent Aaron Koscher

A dissertation submitted in partial satisfaction of the

requirements for the degree of

Doctor of Philosophy

in

Chemistry

in the

Graduate Division

of the

University of California, Berkeley

Committee in charge:

Professor A. Paul Alivisatos, Chair
Professor Richard J. Saykally
Professor Michael Crommie

Spring 2019

Abstract

Synthesis and Characterization of Colloidal Quantum Dot Ensembles
with Near-Unity Photoluminescent Quantum Yields

By

Brent Aaron Koscher

Doctor of Philosophy in Chemistry
University of California, Berkeley
Professor A. Paul Alivisatos, Chair

Colloidal quantum dots are semiconductors with dimensions on the nanoscale and they have remarkable size-tunable optical properties. Colloidal quantum dots have the potential to combine the scalable synthesis and processing conditions of molecular luminophore dyes with the high photoluminescence quantum yield and broad absorption of highly optimized bulk semiconductors. Quantum dots have been used in several optoelectronic applications, including light-emitting diodes and display technologies, in which the performance of the luminophore critically determines the overall efficiency. In addition, there are on-going efforts to develop luminescent concentrators and other optical cavity-based applications that are theorized to experience divergent efficiencies as the quantum yield of the luminophore approaches nearer to unity. While the performance of colloidal quantum dots has continued to improve over the years, there is a tremendous opportunity to optimize the performance of materials operating at near-unity efficiencies. To improve the performance of these materials, strategies must be developed and employed to robustly mitigate the optoelectronic consequences of optical defect states.

This dissertation presents efforts to synthesize, optimize, and characterize high quantum yield colloidal quantum dots. An emerging class of nanoscale luminophores are the cesium lead halide ($CsPbX_3$; X = Cl, Br, I) nanoparticles due to an impressive combination of optical properties and tolerance to material defects. By understanding the underlying mechanism and kinetics of anion exchange reactions, high quality $CsPbX_3$ nanocrystals of any halide composition and visible photoluminescence band gap can be reliably accessed, these ideas are developed in Chapter 2. However, the optical efficiencies of the $CsPbX_3$ nanocrystals are still hindered by non-radiative losses from optical defect states. Post-synthetic selective chemical etching can eliminate the presence of shallow electron traps from the surface of $CsPbBr_3$ nanocrystals and improve the optical performance of these materials to near-unity. The selective chemical etching of $CsPbBr_3$ nanocrystals and the mechanistic understanding of the etching reaction are developed and presented in Chapter 3. In Chapter 4, the optimization of synthetic protocols to robustly access near-unity quantum yield CdSe/CdS core/shell quantum dots is presented. Additionally, the optical characterization of the CdSe/CdS quantum dots and development of a quantum yield measurement with two orders of magnitude less uncertainty than traditional techniques are presented in Chapter 4. These investigations lay the ground work for further optimization of near-lossless materials and development of applications that employ photons as a working fluid.

Table of Contents

List of Figures

Acknowledgements

There are so many people that I want to thank for contributing far more to me than I can express in words. First and foremost, I want to thank my parents for their constant support and encouragement, especially when I needed it most throughout my life. I am so grateful for their dedication, diligent work, and choices that afforded me so many wonderful opportunities. Without them I would not be who I am today. I would also like to thank my brothers, Keith and Christopher, for reinforcing a competitive spirit and pushing me to always be and do better. I also want to thank all the friends and family who made the whole graduate school process a little more enjoyable and a little less lonely during the early mornings, late nights, and weekends.

The ability to explore, understand, and at times slowly create new knowledge while in the Alivisatos Group has been a wonderful experience that I am grateful to have had. The support and guidance from my advisor, Paul Alivisatos, allowed me to develop confidence as a developing scientist and confront new scientific challenges both big and small. For this, I thank Paul for all that he has done to shape the ways I approach science and research. I would also like to thank all the Alivisatos Group members who have made the lab an interesting place to learn, explore, and question new ideas whether scientific or frequently otherwise. Perhaps most critically, I want to thank Negest and Sherry for all that they have done keeping the Alivisatos Group organized and running smoothly.

Additionally, the opportunity to be a small part of many wonderful scientific communities including the EFRC-LMI, EFRC-PTL, and ARPAe MOSAIC has been an engaging and at times challenging experience, but always interesting. I am grateful for all the wonderful science conversations and collaborations that encouraged me to see the world of science from another perspective. I would also like to thank Linda Shimizu and Sahan Salpage from my time at U. of S. Carolina for showing me that synthetic chemistry can be intellectually rewarding, enjoyable, challenging, and has the potential to have tremendous impacts on the world. So many people have impacted my life and I want to thank them all for shaping the way that I see the world and what it might be.

Chapter 1 - Introduction

There are several optoelectronic applications that intimately rely on the absorption and emission of light, a desirable property of different classes of luminophores. Some notable examples of commercialized technology include solid-state lighting, color displays, and bioimaging. Each application has their own set of requirements – metrics such as brightness or color purity, among many others – but a common metric is the optical efficiency of the luminophore that is employed in the application. A commonly used metric to describe the optical efficiency of a luminophore is the photoluminescent quantum yield (PLQY), which can be described as the percent of photons that are emitted relative to the number of photons absorbed. The PLQY is directly related to the optical and electronic quality of a material. High-quality epitaxially deposited bulk materials with careful passivation have been shown to have optical efficiencies exceeding 99%[46,47]. There are molecular systems that have shown PLQYs in excess of 95% when in the optimal local environment[122-124], in addition to having several other advantageous properties, including scalable synthesis conditions and large-area processability.

Despite their respective advantages, molecular systems experience photostability issues compared to bulk materials, while epitaxial bulk materials are grown in non-scalable methods which makes these bulk materials costly. Developing material systems that combine both the stability and efficiency of bulk materials with the scalable synthesis and processing of molecules can provide a class of luminophores with ideal properties. Additionally, while the performance of current classes of luminophores are sufficiently high for several established optoelectronic applications, there are emerging applications are theorized to experience divergent efficiencies as the PLQY of the luminophore approaches nearer to unity. One material system that has the potential to provide this combination of properties are quantum dots, nanoscale semiconductor particles. To this end, this dissertation will focus on investigations into synthesizing and characterizing quantum dot nanocrystals that have optical efficiencies comparable to that of bulk materials.

1.1: General Background on Colloidal Quantum Dots

In recent years, investigations into the size-dependent and size-scaling of material properties has drawn considerable attention due to their potential to have enormous impacts on performance of materials and device technologies. As crystalline materials approach nanoscale dimensions the optical[1–3], electrical[2,4,5], and magnetic[6–8] properties of materials change in a predictable fashion as a result of the physical size of the crystallite. Importantly, as the dimensions of the crystallite approach the nanoscale, the surface-to-volume ratio drastically increases compared to larger crystallites. With large crystals the surface typically has a small influence on the properties of the material and instead the nature of the bulk crystal directly dictates most of the material properties. However, at the nanoscale the surface has an enormous influence on the properties of the crystal simply due to the small size of the crystallite and must be carefully controlled to achieve the desired material properties.

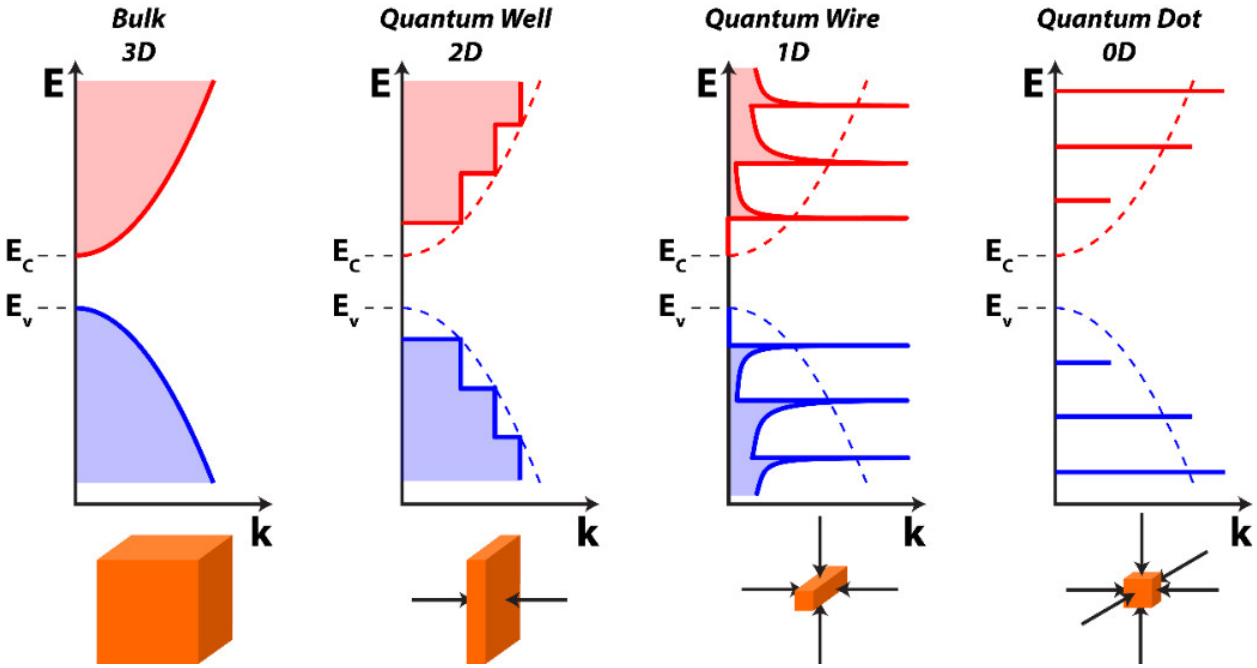

Figure 1.1: Influence of quantum confinement on the semiconductor density of states. For a semiconductor the density of states for the filled states of the valence band ($E<E_v$) are separated from the empty states of the conduction band ($E>E_c$) by a gap in the allowed electronic states called the band gap ($E_g = E_c - E_v$). Bulk semiconductors have a characteristic density of states proportional to $E^{1/2}$, quantum wells proportional to E^0, quantum wires proportional to $E^{-1/2}$, and quantum dots proportional to $\delta(E)$.

The electrons of an individual atom occupy atomic orbitals at specific energies depending on the atomic orbital that they occupy. When multiple atoms combine to make molecules or extended solids, the atomic orbitals of the individual atoms overlap and combine changing the energetic landscape states that electrons can occupy. In an extended solid, the combinations of orbitals can be so finely spaced in energy that they form an energy band, something that nearly resembles a continuum of electronic states. Semiconductors are a class of extended solids that have a characteristic energetic gap in which there are no allowed energetic states present (Figure 1.1) referred to as the band gap. Analogous to the HOMO-LUMO gap of molecules, an extended semiconductor solid has occupied energy bands (valence band) and unoccupied energy bands (conduction band) that are separated by a gap in energy (band gap) (Figure 1.1). The orbital composition that leads to the band gap depends on the material system. As the dimensions of a semiconductor approach the nanoscale, the wavefunctions of an excited electron in the conduction band and hole in the valence band (the lack of an electron from the electron-rich valence band) become confined by the physical barriers of the crystallite, referred to as quantum confinement. Depending on the degree of spatial confinement, the density of electronic states in the semiconductor changes in a characteristic way (Figure 1.1). A quantum well has one confined and two non-confined dimensions, making a two-dimensional electronic structure, with an analogous argument for the one-dimensional electronic structure of quantum wires. For the purposes of this dissertation, the class of quantum confined materials that will be the focus of the discussion are quantum dots. Quantum dots are crystalline semiconductors that have all three dimensions on the nanoscale and are a zero-dimensional object, producing, in the simplest models, a delta-function like density of states as opposed to the continuum for bulk semiconductors (Figure 1.1).

Typically, quantum dots contain tens of thousands of atoms or less in order to be small enough for the nanoparticle to experience the quantum confinement in all three dimensions that is characteristic of quantum dots[3,9–11]. In practice there are several synthetic methods that can be employed to access materials in this size regime. Bulk materials can be top-down processed by lithography, etching, or ball milling among other methods in order to access materials that are small enough to be quantum dots[12–15]. While quantum dots can be accessed using these top-down approaches, the scale and uniformity of these methods are substantial challenges. On the other hand, building quantum dots from molecular precursors offers a highly attractive route to prepare uniform materials at large scales. Molecular precursors can be built into quantum dots through a variety of synthetic chemistry techniques, including molecular beam epitaxy, vapor deposition approaches, and colloidal synthesis[16–20]. Due to the uniformity and scalability of colloidal synthesis, colloidal quantum dots have attracted enormous interest for biological imaging, display technology, light-emitting diodes, and photovoltaics among other applications. The discussions that follow in this dissertation will focus on solution-phase synthesized colloidal quantum dots.

Colloidal quantum dots are generically composed of two components: the inorganic semiconductor nanoparticle and the surface-bound ligands. The ligands can play multiple roles for colloidal quantum dots, including: solubilization of molecular precursors into the reaction solution, controlling the rate of nanoparticle growth during the reaction, passivation of dangling bonds on surface crystallite sites, providing a physical barrier to prevent the agglomeration of quantum dots into larger crystals, and changing excited state energy levels[21,22]. Ligands that have long non-polar hydrocarbon chains are employed to isolate quantum dots from the surrounding non-polar environment and other quantum dots. However, short organic ligands or even small inorganic ligands can be used to change the coupling between quantum dots which can be used to optimize the performance of quantum dots in electronic devices[18,23–25]. This dissertation will focus on colloidal quantum dots with long-chain hydrocarbon ligands in non-polar environments, although there are intense research efforts in many other directions.

1.2: Quantum Dot Confinement Regimes

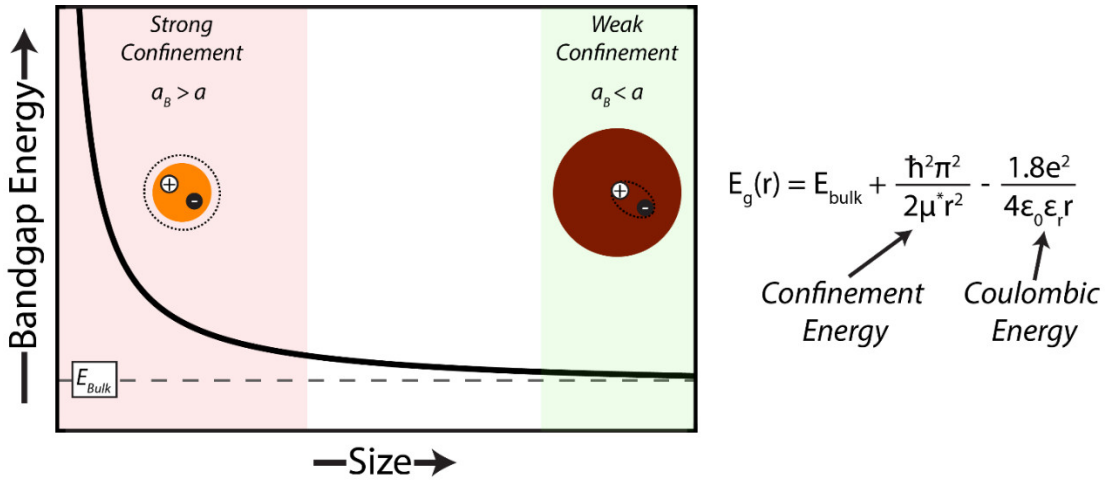

Figure 1.2: Schematic of the size-dependent quantum confinement of quantum dots. The change in bandgap energy as a function of quantum dot size. When the size of the quantum dot (a) is smaller than the Bohr exciton radius (a_B) the quantum dot experiences strong confinement, and when the quantum dot size is larger than the Bohr exciton radius the quantum dot experiences weak confinement. The bandgap energy is described by a correction of the confinement energy and the coulombic energy to the bulk bandgap energy (E_{bulk}).

When a semiconductor absorbs a photon, a negatively charged electron is excited from the valence band into the conduction band, leaving behind a positively charged hole (a hole is the void created in the electron-rich valence band). The negatively charged electron and positively charged hole are attracted together to form an exciton, a bound state that has slightly less energy than the unbound electron and hole, with a characteristic energy that depends on the material. The exciton bound state is akin to that of a hydrogen atom (Figure 1.2), except the exciton binding energy is reduced from dielectric screening and smaller effective masses of the excited electron and hole due to their electrostatic interactions with the semiconductor lattice compared to the hydrogen atom. Due to this reduced exciton binding energy compared to the hydrogen atom, the characteristic size of the bound exciton, described as the Bohr exciton radius, is typically larger than a hydrogen atom with the size depending on the exciton binding energy. In addition to the traditional hydrogenic-like equation (Figure 1.2), the energies of the quantum confined exciton states have additional contributions that depend on the size of the nanocrystal and the dielectric permittivity of the crystal. When the physical size of the nanocrystal is larger than the Bohr exciton radius, the exciton experiences center-of-mass quantization that arises from the Coulombic attraction of the electron and hole (Figure 1.2), a weak quantum confinement. However, as the physical size of the nanocrystal becomes smaller than the Bohr exciton radius, the electron and hole wavefunctions are physically compressed by the boundaries of the nanocrystal, a strong quantum confinement that has an increasingly larger contribution than center-of-mass quantization as the size of the nanocrystal further decreases (Figure 1.2).

By tuning the degree of quantum confinement, the separation of the valence and conduction band, the band gap, can be changed broadly. Since quantum dots experience a size-dependent band gap (Figure 1.2), the optical bandgap of semiconductors can be broadly tuned by varying the physical size of the nanocrystal, providing a convenient synthetic tuning of the material optical properties. The larger the nanocrystal, the smaller the band gap energy of the nanocrystal, allowing photo-generated excitons from longer wavelength photons. On the other hand, smaller

nanocrystals have larger band gaps requiring higher energy and shorter wavelength photons. The ability to broadly tune the band gap energies of these materials have created substantial interest in both fundamental and application focused research efforts.

1.3: Excited State Transition Rates

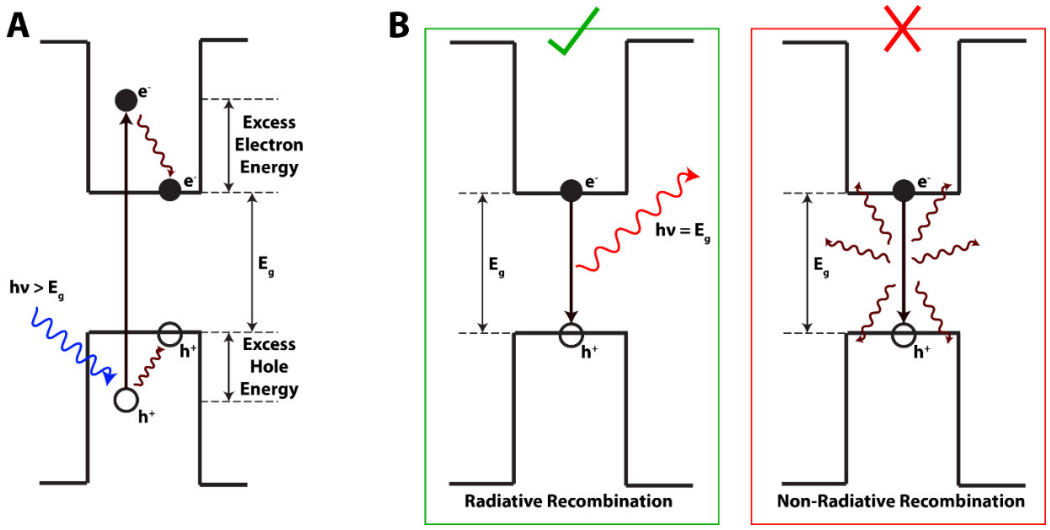

Figure 1.3: Schematic diagram of a semiconductor excited state. (A) Upon photo-excitation of a semiconductor an electron from the valence band is excited to the conduction band. If the photon has an energy larger than the bandgap of the semiconductor, the excess carrier energy is lost to the lattice through thermalization. (B) The thermalized carriers can then recombine either radiatively by emitting a photon with the bandgap energy or non-radiatively by losing the extra energy into lattice vibrations. To achieve high photoluminescence quantum yields, radiative recombination is the desirable excited state pathway.

In addition to their size-dependent band gap energies, another of the appealing aspects of quantum dots is as an emitting material with the potential to have a high PLQY. With this goal in mind, the number of photons that are emitted relative to the number of absorbed photons must be as high as possible. When a semiconductor absorbs a photon with the band gap energy of the material, the excited state of the semiconductor must relax. This relaxation can either be radiative in which photons with the band gap energy are emitted from the material, or non-radiative in which the energy is lost by emitting additional heat. The radiative pathways are those that result in the emission of light whereas the non-radiative pathways are losses in the material. Therefore, the PLQY represents the fraction of recombination events that result in the emission of band edge light:

$$PLQY = \frac{k_{rad}}{k_{tot}} = \frac{k_{rad}}{k_{rad}+k_{nrad}} \tag{1.1}$$

In Equation 1.1, the total recombination rate k_{tot} is the summation of the rates from all recombination pathways, here simplifying the possible rates to the radiative rate k_{rad} and non-radiative rate k_{nrad} which acts to capture all recombination pathways that are not radiative. In order to maximize the PLQY towards unity, non-radiative pathways must be eliminated to reduce the non-radiative recombination rate towards zero, representing a fully radiative recombination

when the non-radiative recombination is zero. For the materials that are going to be discussed in this dissertation, the highest efficiency material possible are those that emit one photon for each absorbed photon. There are other processes such as multiple exciton generation[31,32] or quantum cutting[33,34] that can create more than one excitation per absorbed photon, but these have their own challenges and are outside of the scope of this dissertation.

Although semiconductors can be photo-excited with photon energies that match the band gap energy, they can also be excited by photons with higher energies creating hot-carriers (Figure 3.1) that can lose their extra energy and reach the same band edge energy levels[26–28]. In semiconductors there are several energy levels above the conduction band and below the valence band that the electron and hole, respectively, can access by releasing discrete amounts of energy into lattice vibrations, or phonons. With phonon mediated access to the finely spaced energy levels, hot-carriers release thermal phonons into the semiconductor lattice to reach the band edge energy levels (Figure 1.3) on a femtosecond to picosecond timescale[26–28]. However, at the band edge there is no single lattice phonon (10s of meV) with enough energy to relax the carriers across the band gap (eVs). At this point the cooled carriers remain in the band edge energy levels until later recombining on a nanoseconds or longer timescale[29,30]. This final transition can either be radiative in which photons with the band gap energy are emitted from the material, or non-radiative in which the energy is lost by emitting additional heat. The balance between these two transition pathways critically determines the overall luminescence efficiency of the material.

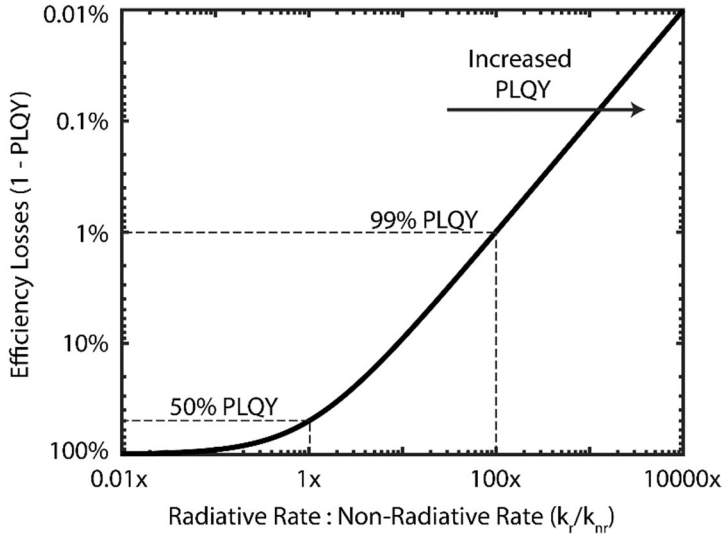

Figure 1.4: Impact of the ratio of the radiative and non-radiative rate on efficiency losses. The trend shows that when the radiative and non-radiative rate are equal the luminophore has a 50% PLQY. As the radiative rate becomes larger than the non-radiative rate, the achieved efficiency increases as the difference increases. Small absolute increases in PLQY are achieved as the difference in the rate substantially changes beyond 99% PLQY.

The rate of radiative recombination depends on the nature of the electronic states involved in the transition and the density of photon states in the environment that the exciton can emit light into. For a homogenous medium within a dipole approximation, the rate of spontaneous emission is well described by Fermi's Golden Rule:

$$k_{i\to f} = \frac{2\pi}{\hbar}|\langle f|H'|i\rangle|^2 g(\hbar\omega) \quad (1.2)$$

The spontaneous emission rate expression (Equation 1.2) indicates that the transition rate between the initial excited state $|i\rangle$ and final ground state $|f\rangle$ depends on the degree of coupling between the two states that emerges as a result of a quantized electromagnetic field[35,36]. For our purposes, the transition rate depends directly on the photon density of states $g(\hbar\omega)$ that the emitted photon can be emitted into. The density of photon states available depends on the photon energy $\hbar\omega$, so that when all other things are equal, emitters with different band gaps will not only emit different energy photons but will also emit photons at different rates. Typically, quantum dots radiatively recombine on the nanosecond timescale, although this timescale varies depending on the material system. Additionally, by intentionally changing the local optical environment and manipulating the local photon density of states, the radiative rate can be dramatically changed. In order to reach high PLQYs and very efficient materials, the number of excitations that radiatively recombine needs to be as high as possible (Figure 1.4), ideally every excitation and this represents an outstanding challenge.

Often there are other competing pathways for the exciton to recombine other than through radiative recombination. Non-radiative pathways limit the achievable PLQY, representing pathways that release heat into the crystal lattice instead of emitting band edge photons. Within perfect crystals, non-radiative transitions across the band gap are very uncommon[37,38] because there are no individual lattice phonon modes with enough energy present to facilitate the transition. However, this transition can still occur in perfect crystals through multi-phonon relaxation, although given number of phonons required for band gaps in the visible, typically 10-100 phonons, multi-phonon relaxation is a relatively rare process[37,38] and is practically negligible for currently achieved PLQYs. However, crystalline defects from non-perfect materials can mediate the non-radiative pathways by inserting electronic states within the bandgap that the electron or hole can access. The net result of these non-radiative pathways are excitations that do not result in photons emitted from the band edge. It is important to note that there are other applications that require heat to be emitted such as photothermal therapy[39] or optical heating[40] but are outside of the scope of this dissertation. Developing controlled strategies to mitigate the optoelectronic consequences of defects and reduce non-radiative recombination is critical to achieving near lossless emitters.

1.4: Defects in Quantum Dots

Within bulk crystals, the presence of lattice defects – vacancies, interstitials, dislocations, grain boundaries, precipitates, and others – are major contributors to overall performance of the material. Crystalline defects are locations where the ordered periodicity of the crystal lattice is disrupted, often introducing local electronic defect states that are within the band gap of the semiconductor to varying degrees depending on the local environment of the crystalline defect. With finely tuned synthesis and passivation conditions, semiconductors like silicon or GaAs have achieved remarkably low defect densities. However, typical defect densities in bulk semiconductors are around $10^{15} – 10^{17}$ cm^{-3}, with the potential to be lower as preparation methods are robustly refined. Given the small size of the quantum dot crystallites, many synthesized quantum dots will be defect

free assuming that the bulk internal defect concentrations remain the same per volume at the nanoscale. Due to the large surface-area-to-volume ratio of nanostructured materials, the surface plays a substantial role in determining the optical performance unlike in bulk materials. Several issues occur at the surface of quantum dots including surface strain, vacancies, and dangling bonds from under-coordinated surface atoms that arise from the abrupt termination of the crystal lattice. A substantial research effort has been put into mitigating problems at the surfaces of nanocrystals and improving material performance.

Although quantum dots can have a substantial number of dangling bonds on the surface, one of the primary roles of the surface bound organic ligand shell is passivation by forming bonds to under-coordinated surface atoms. Ligands can provide or accept extra electron density to the nanocrystal surface to not only mitigate dangling bonds but also to maintain the charge neutrality of the surface in non-polar media. As such, there is an ideal ligand packing density on the surface and amount of electron density needed to fully passivate all the surface atoms. However, the packing density can be fundamentally limited by geometrical constraints[41] and the amount of electron density provided to or removed from the quantum dot surface from a binding ligand can be insufficient to fully passivate a dangling bond. Either route results in non-negligible surface states that can trap carriers. Beyond ligand passivation, an additional passivation method is to increase the distance between the emissive states and the surface defect states, reducing the influence that the surface has on the optical performance. This is routinely accomplished in quantum dots by growing an epitaxial shell of a different semiconductor material around a quantum dot core, resulting in a geometry commonly referred to as a core/shell quantum dot. However, lattice mismatches between the core and the shell materials can introduce interfacial strain and defects into the core/shell structure. Minimizing the lattice mismatch between the core and shell material is essential to eliminate the influence of that interface.

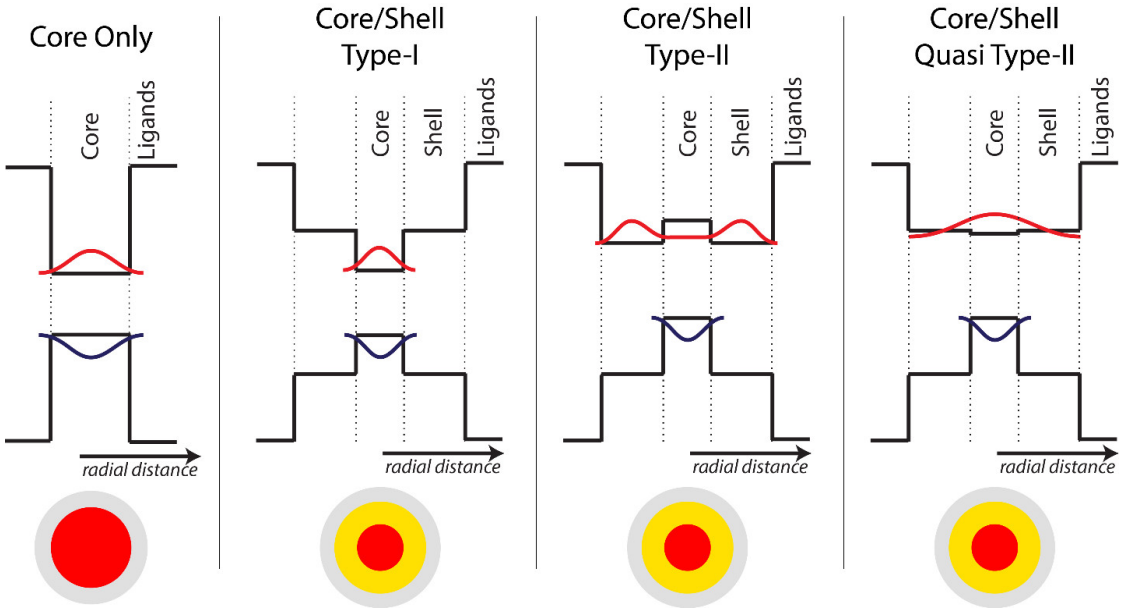

Figure 1.5: Quantum dot heterostructure band-alignments for the metal chalcogenides. Depicted in the relative band-alignment for quantum dot cores and different core/shell heterostructures. For the cores, the electron and hole wavefunction are within the semiconductor shell, surrounded by the ligands with a much larger energy gap, creating

a situation like a particle in a box. When an epitaxial shell material is grown around the core, the electron and hole wavefunctions can remain in the same region (Type-I, ex. CdSe/ZnS), in different regions (Type-II, ex. CdSe/CdTe), or with one wavefunction delocalized over the entire particle and one localized wavefunction (Quasi Type-II, ex. large shell thickness CdSe/CdS).

Additionally, the way that a core/shell quantum dot heterostructure performs depends on the relative energetic position of the energy bands of the materials, the heterostructure band alignment. For the purposes of this dissertation the focus will be on Type 1, Type 2, and quasi-Type 2 band alignments, although other variants are possible. For Type 1 quantum dots (Figure 1.5), both the electron and hole wavefunctions are localized in the core of the core/shell quantum dot, maintaining a large electron and hole wavefunction overlap. For Type 2 quantum dots (Figure 1.5), the electron and hole wavefunctions are separated into the core and shell, reducing the electron and hole wavefunction overlap causing the radiative rate to decrease. The quasi-Type 2 band alignment retains features of both Type 1 and Type 2 band alignments. In quasi-Type 2 quantum dots (Figure 1.5), one carrier wavefunction is localized in one region of the core/shell structure, whereas the other carrier wavefunction is delocalized throughout the entire quantum dot. As the shell material is increased in quasi-Type 2 quantum dots, the overlap of the electron and hole wavefunctions can drastically vary, changing the radiative rate of the material. Through careful synthetic engineering, core/shell quantum dots with surface ligand passivation can present PLQYs that approach near-unity[42–45] although the core quantum dot presents PLQYs that are less than 10%. These core/shell quantum dots are beginning to be competitive with the most efficient rare-earth doped single crystal glasses[46] and epitaxial-deposited thin films[47]. Carefully tuning the material preparation properties continues to improve the performance of quantum dots higher with the potential of pushing the efficiency of these materials for several important optoelectronic applications.

The main discussion of this dissertation is divided into three sections, highlighting different but related projects aimed to reliably access quantum dot luminophores with near-lossless performance. Two main material systems will be discussed in this dissertation: the rapidly emerging $CsPbX_3$ (X = Cl, Br, I) weakly quantum-confined nanocrystals and the traditional CdSe/CdS core/shell heterostructure quantum dots. Chapter two will focus on anion exchange reactions and kinetics that offer the potential to easily tune the composition and optical properties of $CsPbX_3$ nanocrystals. Chapter three will focus on selective chemical etching of undercoordinated lead in the $CsPbBr_3$ nanocrystals to reliably improve the optical performance of the materials to near-unity efficiencies. Finally, chapter four will focus on the synthetic optimization of CdSe/CdS core/shell quantum dots to reach near-unity quantum yields, as well as a measurement technique capable of quantifying the performance of these materials with much less uncertainty than traditional measurements.

Chapter 2 - Post-synthetic Anion Exchange of $CsPbX_3$ (X = Cl, Br, I) Nanocrystals

The following discussion is adapted from Koscher, B.A., Bronstein, N.D., Olshansky, J.H., Bekenstein, Y., Alivisatos, A.P., Surface- vs Diffusion-Limited Mechanisms of Anion Exchange in $CsPbBr_3$ Nanocrystal Cubes Revealed through Kinetic Studies, J. Am. Chem. Soc., ***2016****, 138, 12065-12068.*

2.1: Post-synthetic Chemical Transformations at the Nanoscale

Colloidal nanocrystals (NCs) with controlled composition, shape, and phase can change the optical[1–3], electrical[2,4,5], and magnetic[2,6–8] properties of the underlying material, to name a few of the material properties that change at the nanoscale. Due to the appearance of these material properties at the nanoscale, the rational synthesis of nanostructured materials has been the subject of intense academic and industrial research. To reliably obtain structures with pre-specified functionality, two general strategies have been promising routes forward: direct synthetic methods and post-synthetic transformations. The direct synthesis of NCs requires carefully tuning nucleation and growth, as well as choosing appropriate ligands to both solubilize precursors and act as nanocrystal surface ligands to direct the synthesis. Additionally, these conditions must be optimized at high temperatures sufficient to achieve phase-pure materials[42,45,48], typically requiring temperatures up to nearly 400°C or higher. As such, achieving NC with tailored composition, phase, and shape directly from synthetic reactions can be difficult due to the nature of the many interconnected parameters that dictate the outcome of NC syntheses. Understanding the interconnected nature of these synthetic parameters is critical to expanding the library of achievable nanostructured materials and will likely represent a direction of intense research effort.

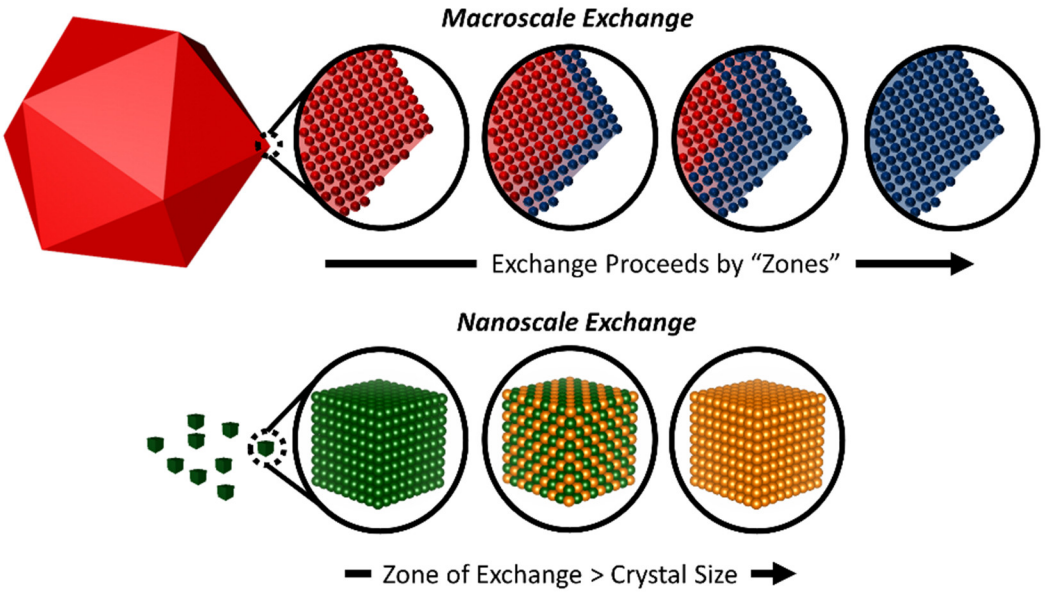

Figure 2.1: Schematic depiction of the size-dependent anion exchange trajectory. The macroscopic anion exchanges typically progress through regions limited by solid-state diffusion, creating zones of exchange that are substantially smaller than the crystallite size. On the other hand, the nanoscale anion exchange has zones of exchange that are

either comparable or larger than the crystallite size due to the nanoscale material. The nature of nanoscale crystallites enables several post-synthetic transformations.

On the other hand, post-synthetic transformations can utilize the refined synthetic protocols of existing NCs as frameworks to access materials with compositions, phases, and shapes that are challenging or not yet possible to realize with direct synthesis. At the nanoscale, several post-synthetic transformations have been effectively used to post-synthetically transform NCs including the Kirkendall effect[49,50], galvanic replacement[51,52], and ion exchange[53,54]. These methods can be more facile at the nanoscale and NCs tend to exhibit qualitatively distinct kinetics for these solid-state chemical transformations compared to their larger-scale material counterparts[53,55]. The facile nature of post-synthetic transformations arise from high surface-to-volume ratios and short diffusion path lengths inherent with NCs. Of interest to the following discussion is nanoscale ion exchange. For solid-phase ion exchange reactions, typically the exchange reaction front extends several atomic layers into the material, on the order of nanometers. In bulk extended materials, the exchange must then proceed through many sequential reaction zones, with ions needing to diffuse long distances[56–58]. For nanoscale materials, due to the small number of atomic layers, the width of the reaction zone can become comparable to the overall size of the crystal, greatly reducing the difficulty for ions to exchange in NCs (Figure 2.1).

At this point several selective ion exchange reactions have been reported in NCs, but these exchange reactions have predominately focused on cation exchange reactions[53,54,59–65]. Some notable examples include CdSe to Ag_2Se[53,65], Cd_3P_2 to InP[59], CdS to PbS nanorods[61], PbE (E = S, Se, Te) to core-shell PbE/CdE[62], $Cu_{2-x}S$ to $CuInS_2$[63], and $Cu_{3-x}P$ to InP[64]. In these cation exchange reactions, the anionic sub-lattice of the material remains relatively fixed, allowing for partial or complete replacement of the cations. As a result of this stationary anionic sub-lattice, the shape and crystallographic phase of the parent NC can be maintained following cation exchange. Although cation exchange has been shown to be a useful method to post-synthetically transform materials, the analogous anion exchange has far fewer reports and is more commonly associated with drastic morphological changes to the overall NC[52,66]. To this end, developing material systems that can be finely and arbitrarily controlled represents an important goal of post-synthetic transformations and is an area of active research. To develop high levels of control in these reactions, the underlying mechanisms and kinetics are necessary pieces of information to broadly apply these methods to other classes of materials.

2.2: Synthesis of $CsPbX_3$ Nanocrystals

An emergent class of luminophore materials at the nanoscale are the lead halide perovskite salts, with research interests driven in a large part due to the overall impressive optoelectronic performance, potentially important materials for several important applications[67,68]. At this point, several synthetic protocols have been reported for the synthesis of the all-inorganic cesium lead halide perovskite nanocrystals ($CsPbX_3$; X = Cl, Br, I). The large degree of acceptable synthetic conditions highlights the material system's overall versatility and ease of synthetic access to the materials. The following discussion uses nanocrystals synthesized based on synthetic protocols from Protesescu et al.[69] with minor modifications towards the optimization of the synthesis and isolation of the synthesized materials.

2.2.1: Chemicals Used in the Synthesis of $CsPbX_3$ Nanocrystals

Lead chloride ($PbCl_2$, 99.999%, Sigma Aldrich), lead bromide ($PbBr_2$, 99.999%, Sigma Aldrich), lead iodide (PbI_2, 99%, Sigma Aldrich), cesium carbonate (Cs_2CO_3, 99.9%, Sigma Aldrich), octadecene (ODE, 90% tech grade, Sigma Aldrich), oleic acid (OA, 90% tech grade, Sigma Aldrich), oleylamine (OLA, 70% tech grade, Sigma Aldrich), hexanes (mixture of isomers, anhydrous 95%, Sigma Aldrich), toluene (anhydrous 99%, Sigma Aldrich), ethyl acetate (anhydrous 99.8%, Sigma Aldrich), and methyl ethyl ketone (99%, Sigma Aldrich) were purchased and used without further purification.

2.2.2: Synthesis of $CsPbX_3$ Nanocrystals

First a stock solution of Cs-Oleate was prepared by adding 2.5 mmol Cs_2CO_3 and 2.5 mL OA into a three-neck round-bottom flask containing 40 mL ODE. The solution was dried and degassed under high vacuum for between 1-2 hours at 120 °C. The solution was then heated to 150 °C under dry argon gas and maintained until all Cs_2CO_3 was solubilized by OA. The resulting solution was then cannula transferred into another container for storage inside an argon-filled glovebox. The solution was then subsequently heated, and a small volume taken for use in reactions.

To synthesize the $CsPbX_3$ nanocrystals, 5 mL ODE and 0.188 mmol of the desired lead halide salt was added into a three-neck round-bottom flask. Only one type of lead halide salt was added to achieve pure composition materials, whereas mixtures of halide salts were added to achieve mixed halide compositions directly from the synthesis. The solution of ODE and lead halide salt was degassed under high vacuum at 120 °C for 1-2 hours. Afterwards, the solution was put under argon gas, 0.5 mL of pre-degassed OA and 0.65 mL of pre-degassed OLA were injected, and the solution temperature was raised to 140 °C. Following dissolution of the lead halide salts, the temperature was adjusted to between 140 – 160 °C before the injection of 0.5 mL of the previously prepared Cs-Oleate solution was injected. The average size of the nanocrystal ensemble depends on the injection temperature. Following injection, the reaction mixture is cooled after 5-10 seconds quickly by an ice-water bath.

Three isolation methods work with high efficacy for $CsPbX_3$ samples. In the first method, the crude solution is first centrifuged at 4000 RPM or lower for 3 minutes to remove excessively large aggregates and a small quantity of brown-colored by-products, keeping the supernatant. The supernatant is then centrifuged at 10000 RPM for up to 10 minutes at low-temperatures (0 – 10 °C), re-dispersing the isolated nanocrystals in anhydrous hexanes for storage. While this method results in samples with good optical performance, the samples have a large excess of ligand and ODE present. In the second method, the crude solution is first centrifuged at 4000 RPM or lower for 3 minutes to remove the un-wanted by-products, keeping the supernatant. By adding anti-solvent, either ethyl acetate or methyl ethyl ketone, and centrifuging at 8000 RPM for 5 – 10 minutes the particles are effectively isolated from the reaction solution. Samples are then re-dispersed in anhydrous hexanes for storage. While this method very effectively cleans the excess organics and isolates even small nanocrystals, the optical performance of the samples is hindered

by the anti-solvent addition. In the third method, around 5 mL of anhydrous hexanes is added to the crude reaction solution and centrifuged at 4000 RPM to remove unwanted by-products. Since ODE is not a great solvent for the $CsPbX_3$ nanocrystals, the hexanes can be evaporated from the solution in step-wise fashion to isolate different sizes of nanocrystals from the reaction mixture by centrifugation and then re-dispersing the nanocrystals in anhydrous hexanes. This method isolates reasonably clean samples with high optical efficiency and very narrow size distributions, although it is not able to isolate the smallest particles. Either method results in nanocrystal samples that are reasonably stable over long-terms and can be stored in a glovebox or in air. Depending on the size, composition, and quality of the nanocrystal ensemble desired, different isolation methods of the three detailed above are employed to access the best-possible quality ensembles.

2.2.3: Optical Properties of the As-Synthesized $CsPbX_3$ Nanocrystals

The lead halide perovskites have received substantial interest due to their exceptional optoelectronic properties. Of interest to this dissertation discussion, the $CsPbX_3$ nanocrystals have narrow linewidths, strong absorption coefficient, fast radiative recombination rates, and high photoluminescence quantum yield – without the need for the overgrowth of an epitaxial passivating semiconductor shell. These remarkable properties arise from the materials unusually high tolerance to material defects[70–72].

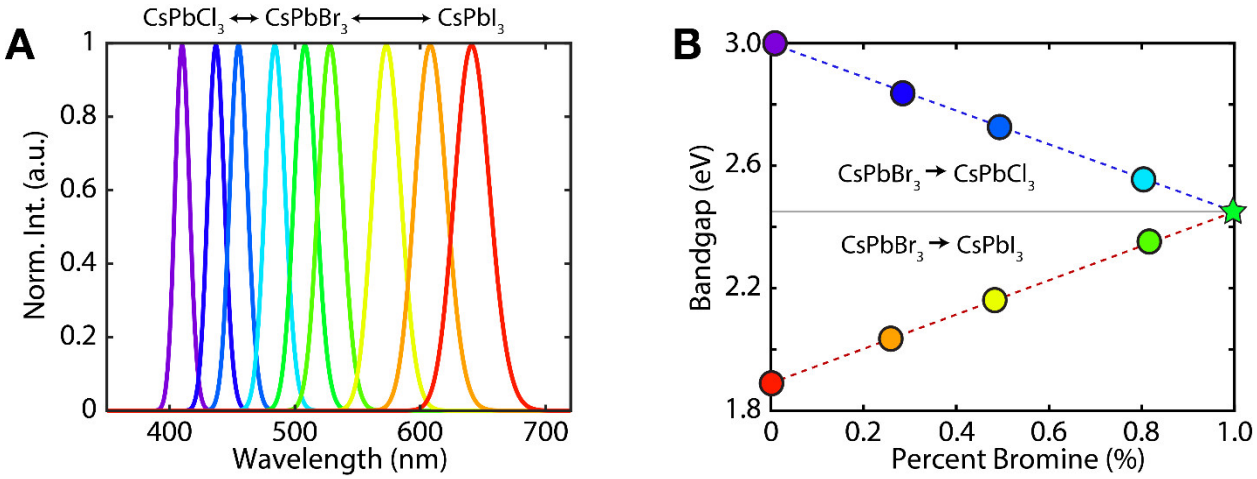

Figure 2.2: Composition dependent band gap of the $CsPbX_3$ nanocrystals. (A) The photoluminescence spectra for a series of samples with pure halide compositions (Cl, Br, and I) and mixed halide compositions (Cl/Br, and Br/I), spanning the visible from 400 – 700 nm. Each of the samples presents a narrow photoluminescence spectrum that is limited by the size-distribution of the sample. (B) Change in the photoluminescence band gap and the halide with different halide compositions for nanocrystals with the same number of average unit cells. Shown in the linear trend for the mixed Cl/Br compositions between 2.5 eV and 3.0 eV, and the mixed Br/I between 1.9 eV and 2.5 eV. The star represents the pure phase $CsPbBr_3$ nanocrystals that were anion exchanged to yield the series of exchanged samples represented with circles.

Analogous to other quantum confined materials, the bandgap energies of $CsPbX_3$ NCs can be tuned through quantum confinement effects, although the range is somewhat limited compared to other material systems. Typically, experimental reports employ $CsPbX_3$ NCs that are around 10 nm or greater and in this size regime the NCs are weakly quantum confined[69] if at all, with sizes

comparable or larger than their Bohr exciton diameter ($CsPbCl_3$ – 5 nm, $CsPbBr_3$ – 7 nm, $CsPbI_3$ – 12 nm). In the weak quantum confinement regime, there are only small quantum confinement effects that emerge from size changes which limits the bandgap tunability from size changes. However, the $CsPbX_3$ NCs have an additional tunable parameter, the halide composition which allows ready tuning across the entire visible spectrum between 400 and 700 nm (Figure 2.2). The mixed halide compositions of $CsPbX_3$ NCs can be readily obtained by adjusting the ratio of halides present during the synthesis. For example, introducing a 1:1 ratio of chlorine to bromine during the synthesis yields a nanocrystal ensemble with a halide composition that approximately corresponds to the introduced 1:1 halide ratio. With this approach solid-state alloys of chloride/bromide and bromide/iodide can be obtained directly from the synthesis. However, consistent with bulk phase diagrams[73], solid-state alloys of chloride/iodide are not obtained, but instead phase separated $CsPbCl_3$ and $CsPbI_3$ NCs are obtained[74,75]. Conveniently, the halide composition of the NC ensemble can be quickly determined by measuring the PL spectrum of the NC ensemble and linearly extrapolating between the bandgap of the two pure materials (Figure 2.2).

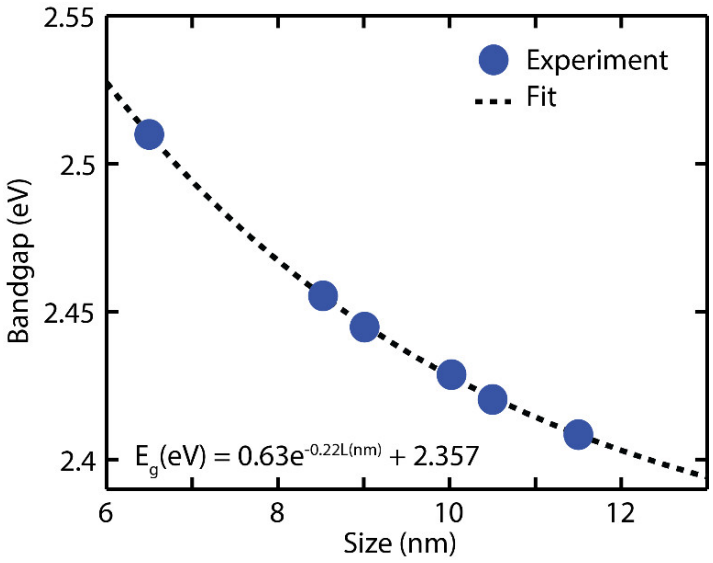

Figure 2.3: Size-dependent band-gap of the $CsPbBr_3$ nanocrystals. Although the $CsPbBr_3$ nanocrystals that are typically accessed are in the weak confinement regime, the measured photoluminescence band gap of the material is a direct reporter of the size of average size of the nanocrystal ensemble. Displayed is an empirical equation that allows easy determination of the size of the ensemble from the optical band gap, although the physical interpretation of all the expression's constants is yet unknown.

Despite the potential for each of the material compositions to be highly efficient luminophores, there has been a large research effort devoted to the $CsPbBr_3$ nanocrystals. This is partly due to the stability advantage over the equally efficient $CsPbI_3$ composition and efficiency advantage over the equally stable $CsPbCl_3$ composition. As such, much of the preceding discussions will focus on using the $CsPbBr_3$ nanocrystals as the starting material to employ. Fortunately, due to the optical properties of quantum dots, the average size of the $CsPbBr_3$ nanocrystal ensemble can be quickly determined by the optical band gap (Figure 2.3). The small change in bandgap with large change in size of the nanocrystal ensemble originates from a combination of weak quantum confinement and likely the emergence of substantial dielectric confinement[76] due to the highly

ionic nature of the material system. Regardless, the $CsPbBr_3$ nanocrystals provides perhaps the most robust starting material for investigating the cesium lead halide perovskite nanocrystal optoelectronic properties.

2.3: Facile Colloidal Solution Anion Exchange in $CsPbX_3$ Nanocrystals

Despite their impressive as-synthesized properties, there has been a significant effort to expand the functionality and tailor the optoelectronic properties of the $CsPbX_3$ nanocrystals through post-synthetic modifications. Due to the nanoscale morphology, anion exchange might be an efficient method to arbitrarily tune the overall halide composition of the nanocrystal ensemble, offering the potential for more facile approach to access these material compositions. As opposed to the traditional covalently bound quantum dot materials (i.e. CdSe, InP, etc.), the lead halide perovskites are known to have a large anionic mobility[77,78] within the lattice with a relatively small barrier to solid-state anion diffusion, suggesting the potential for halide anions to easily move throughout the lattice. Also supporting this notion, the lead halide perovskites have a relatively rigid cationic sub-lattice instead of a rigid anionic sub-lattice seen in other material systems, enabling a room-temperature anion exchange in $CsPbX_3$ NCs using mild anion exchange sources while also maintaining the shape of the parent NC ensemble.

2.3.1: Steady-State Anion Exchange Reaction Conditions

First anion exchange stock solutions were pre-prepared using similar conditions to the chemical synthesis of the nanocrystal to minimize the perturbative nature of the exchange. Into a scintillation vial, 5 mL of anhydrous toluene or anhydrous hexanes, 0.188 mmol of pure lead halide salt ($PbCl_2$, $PbBr_2$, or PbI_2), 0.5 mL OA, and 0.65 mL OLA were added within an argon atmosphere glovebox. The resulting heterogeneous solution was stirred at elevated temperatures (100 °C for toluene or 50 °C for hexanes) within an argon atmosphere until the complete dissolution of the lead halide salt occurs, up to several hours for hexanes. The resulting stock solution is long-term stable at room temperature but was stored at room temperature to maintain the dryness and integrity of the stock solution over time.

To conduct the steady-state anion exchange reactions, a known concentration of the previously prepared anion exchange solution was added to a known concentration of $CsPbX_3$ nanocrystals. The relative concentration of the stock solution and nanocrystals were adjusted to achieve the desired material composition. Each of the reactions were conducted at room temperature and equilibrated for several minutes to ensure the nanocrystal solutions reached steady-state compositions. Once the steady-state compositions are reached, the anion exchange is halted, affording an opportunity to characterize the resultant nanocrystals as the nanocrystals do not change their average halide composition further and are long-term stable. The steady-state materials were characterized through traditional optical and structural techniques.

2.3.2: Results of Steady-State $CsPbX_3$ Anion Exchanges

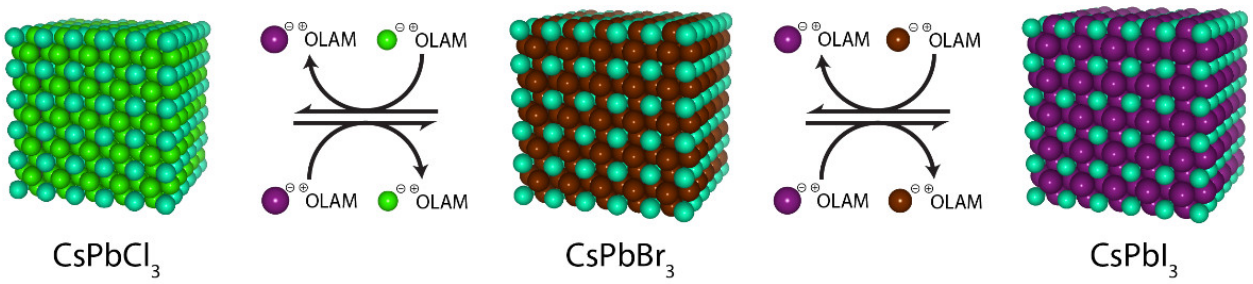

Figure 2.4: Overall schematic of the anion exchange reactions of $CsPbX_3$ nanocrystals. Although it is possible to use several different halide sources, the oleylammonium halides were chosen as a facile and minimally perturbative halide source for the anion exchange. The anion exchange reactions can reversibly access solid-state mixtures of Cl/Br and Br/I through the addition of the appropriate halide source, whereas the Cl/I phase materials are not accessible consistent with the bulk-phase material.

Anion exchange reactions in the $CsPbX_3$ NCs are accomplished by adding a halide source (lead halide salts[74,75], ammonium halide salts[55,74,75,79], organometallic Grignard reagents[74,75], or trimethylsilyl halides[80] among other sources) with the desired halide to exchange. A series of $CsPbX_3$ NC ensembles with different halide compositions can be obtained from direct chemical synthesis but require separate chemical reactions, whereas the entire series can be obtained from the same parent NC ensemble using anion exchange. This ensures that all obtained NC solid-state alloys have the same overall NC shape and crystallite quality, enabling systematic study of different alloys while minimizing the role that subtle crystallite differences have on the optical performance of these materials. It should be noted that the $CsPbX_3$ NCs are particularly sensitive to polar solvents and moisture, which does place practical limitations on the types of halide sources that can be employed while still achieving the best quality anion exchange results. For the purposes of the following discussion, all exchanges are conducted in either anhydrous hexanes or toluene, along with dry halide precursors to prevent additional undesirable side-reactions from polar solvents. Additionally, while the anion exchange can be conducted with a variety of halide sources, this discussion will focus on using oleylammonium halide (OLAM-X) species, generated by solubilizing PbX_2 salts with the same concentration of oleic acid and oleylamine as employed for the nanoparticle synthesis (Figure 2.4). The OLAM-X anion exchange precursors were selected because the species is used to synthesize the NC ensemble and therefore already present in solution, representing the species that would be the least perturbative to the system. Additionally, the OLAM-X species is soluble in non-polar solvents resulting in relatively quick and reliable exchange reactions compared to other species[55,74,75,79].

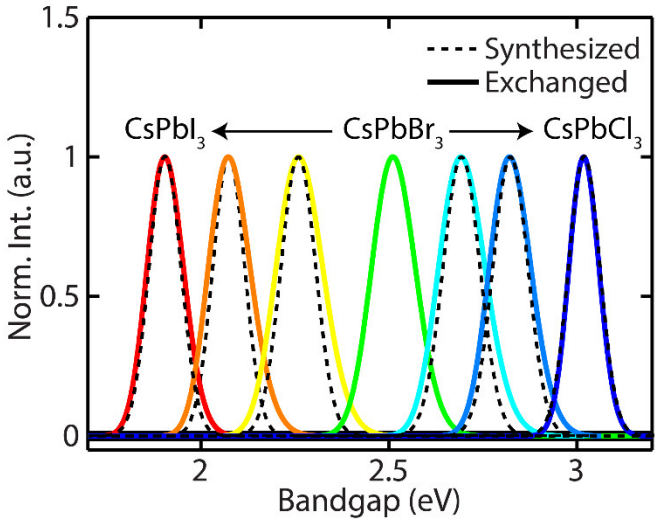

Figure 2.5: Comparison of the as-synthesized and exchanged photoluminescence linewidth. Each of the deliberately partial anion exchange solution were chosen to have the same optical band gap as the as-synthesized samples, although the accessible band gaps far exceed those displayed.

As a result of the anion exchange reactions, the optical bandgap of the NC ensemble shifts corresponding to a material with a composition including both the halide from the parent NC and the target exchange halide, as expected for such a halide anion exchange in these materials. The anion exchange of $CsPbX_3$ NCs can be nearly complete or deliberately partial, yielding ensembles with similar optical properties compared to the as-synthesized particles. Importantly, the PL linewidth, measured as the full width at half maximum, of the anion exchanged particles is comparable to the as-synthesized NCs (Figure 2.5). However, the initial size distribution of the sample directly influences the linewidths of the anion exchanged particles, as each subtly different sized nanocrystal in the ensemble size distribution contributes subtly different band gap energies to the overall linewidth based on their single-particle PL linewidth[81,82].

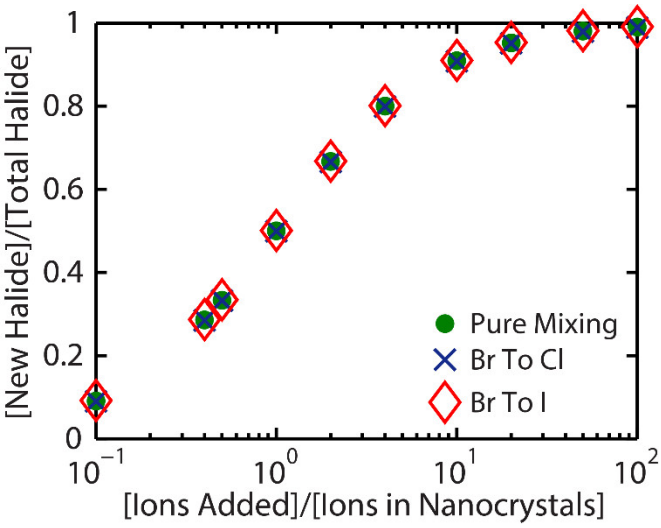

Figure 2.6: Steady-state anion exchange halide composition of $CsPbX_3$ nanocrystals. The resulting halide fraction of the steady-state alloys depend on the fraction of the new halide added relative to the older halide to exchange present

within the nanocrystal ensemble. Each of these exchange reactions were conducted on the same starting $CsPbBr_3$ nanocrystal sample at room temperature.

When considering the trajectory that an ion exchange reaction will take, the expected distribution of ions following exchange can be rationalized by the balance of cohesive crystal energies and solvation energies of the ion complexes in solution[54,60]. For a pure mixing scenario, the result of the exchange is dictated by entropic considerations instead of enthalpic ones, favoring the formation of solid-state alloys representing the average composition of ions present in solution. The presence of enthalpic contributions will cause deviations from the pure mixing scenario, favoring the inclusion of one ion over the other within the crystal lattice. For the halide anion exchange reactions in $CsPbX_3$ NCs, there are no significant thermodynamic equilibrium differences that favor one halide ion over another within the material, strongly aligning with a pure mixing scenario (Figure 2.6). For example, adding a 1:1 molar ratio of chloride ions relative to bromide ions present in a $CsPbBr_3$ NCs solution results in an equilibrated NC sample that contains 50% bromide and 50% chloride, with a bandgap that corresponds to a $CsPbCl_{1.5}Br_{1.5}$ ensemble. This is a consistent trend that emerges for both Br/Cl and Br/I composition gradients. This suggests that the entropic contribution for these anion exchange reactions is much larger than the enthalpic contribution, yielding highly predictable steady-state alloy compositions that can be probed by an optical measurement of the quantum dot ensemble bandgap (Figure 2.6). It should be noted that small thermodynamic differences between the different halides have been measured in bulk studies[83], suggesting that there might be an enthalpic contribution to the exchange reaction introducing small halide-dependent thermodynamic differences that beyond the sensitivity of this experimental work.

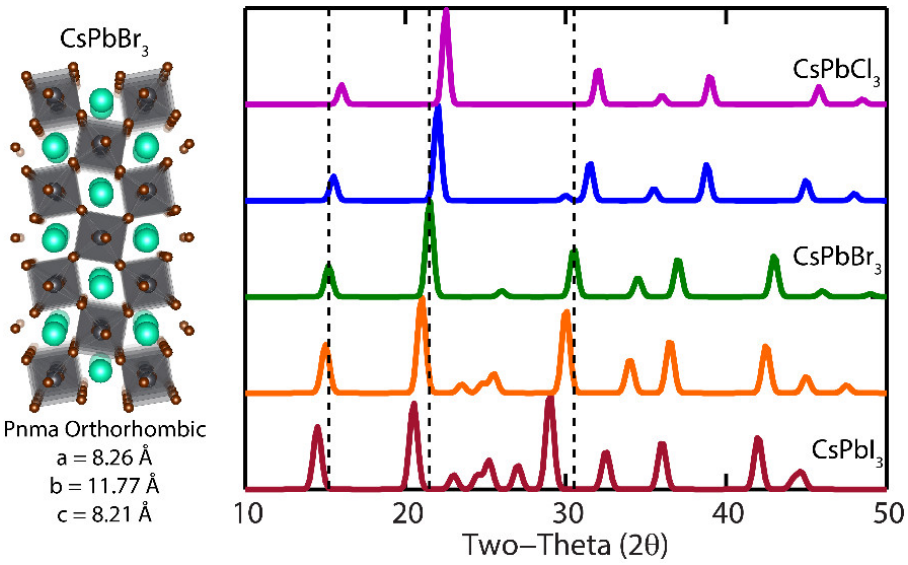

Figure 2.7: XRD characterization of anion exchange samples of $CsPbX_3$ nanocrystals. The composition dependent x-ray diffraction pattern for the exchanged particles, with each exchange starting from the $CsPbBr_3$ nanocrystal sample and going to either $CsPbCl_3$ or $CsPbI_3$ nanocrystals. The diffraction peaks appear as expected for the materials exchanging halides, consistent with the as-synthesized materials.

Additionally, the crystal structure of the parent NC is maintained following partial or near-complete exchange of the parent halide, presenting XRD patterns that are consistent with the

directly synthesized materials[69,74,75]. This ability of the $CsPbX_3$ NCs to maintain their crystallographic phase throughout the anion exchange is attributable to a relatively stationary cationic lattice, analogous to the nanoscale cation exchange reactions studied in other materials. For these materials, the activation barrier for halide vacancy diffusion (200-300 meV depending on halide) is much lower than the barrier for lead (~2.3 eV) or cesium (~1 eV) diffusion[77,84,85]. Consistent with expectations, the unit cell dimensions depend on the halides present in the NC ensemble with the unit cell expanding upon incorporation of iodide ions and shrinking upon incorporation of chloride ions, well-aligned with reported values for pure halide materials (5.6 Å for $CsPbCl_3$; 5.9 Å for $CsPbBr_3$; and 6.3 Å for $CsPbI_3$; each of the values are for the Pm-3m simple cubic crystal structures whereas the Pnma orthorhombic structures are slightly distorted versions with comparable average unit cell dimensions) (Figure 2.7).

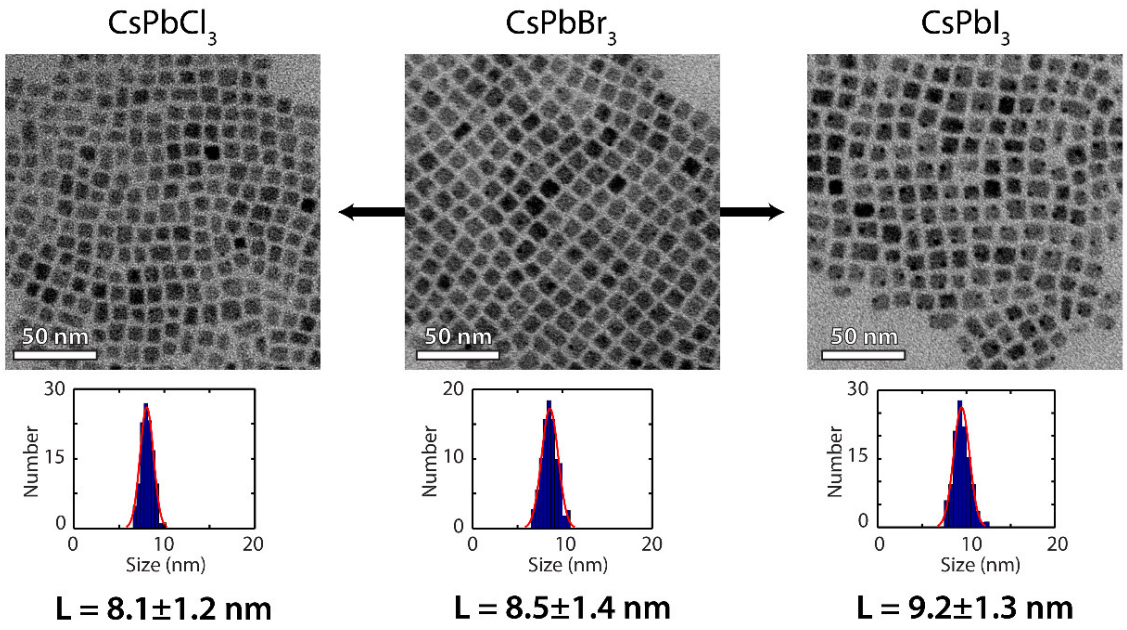

Figure 2.8: Nanocrystal size and morphology following the anion exchange reaction. The TEM images and sizing distributions are for anion exchange reactions that started from the same $CsPbBr_3$ nanocrystal sample and were exchanged to either $CsPbCl_3$ or $CsPbI_3$ using the appropriate OLAM-X precursors.

The changing unit cell dimension manifests itself as changes in the overall size of the nanocrystal throughout the anion exchange reaction (Figure 2.8). For example, a $CsPbBr_3$ NC ensemble that is initially 8.5±1.4 nm in edge length shrinks slightly to 8.1±1.2 nm when fully exchanged to $CsPbCl_3$ and expands slightly to 9.2±1.3 nm when fully exchanged to $CsPbI_3$. Although the size of the NC changes slightly to accommodate halide ions with different sizes, the overall morphology of the nanocrystal ensemble does not change (Figure 2.8), highlighting the mild nature of the anion exchange relative to previously reported anion exchange efforts in other material systems[51,52,66]. If the ion exchange reaction is sufficiently perturbative to the NC structure, the overall shape of the NC can rearrange to minimize its surface area or drastically change its overall morphology[51,52,66]. Although the focus of this discussion is on $CsPbX_3$ NC cubes, the mild nature of the exchange reaction is also readily extended to $CsPbX_3$ NCs with different morphologies, such as nanoplates that maintain their shape following the anion exchange[79].

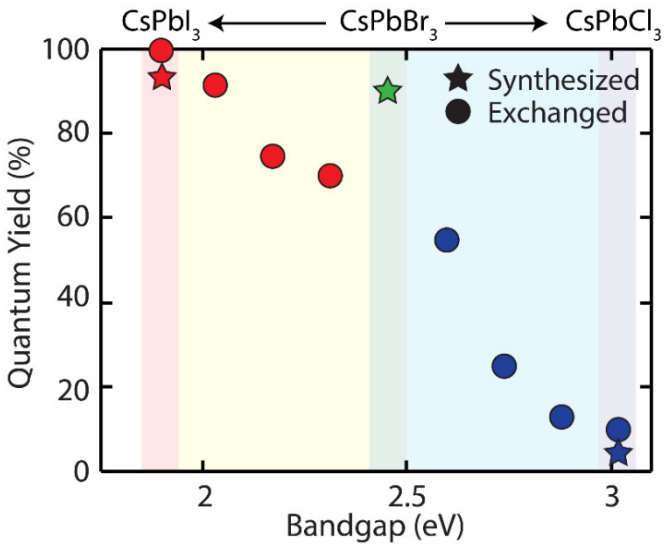

Figure 2.9: Composition dependent quantum yield of $CsPbX_3$ nanocrystals. Shown are the pure phase materials that were obtained directly from synthesis (stars), as well as the composition series obtained from anion exchange (circles) starting from the same $CsPbBr_3$ sample including samples with the same band gap as the as-synthesized materials.

An important consideration for post-synthetic transformations, including ion exchange reactions, is the potential to introduce non-negligible structural and surface defects into the material, an undesirable consequence of some reported NC ion exchanges[51,52,66,86]. By inspection of the resulting ensembles, the anion exchange does not appear to introduce significant numbers of optically-active defects into the material, if any, maintaining the impressive optical properties of the $CsPbX_3$ material system following the exchange. Typically, the as-synthesized materials present photoluminescent quantum yields (PLQYs) ranging from 5-95% depending on the NC halide composition (Figure 2.9), with the lowest values measured for $CsPbCl_3$ NCs and comparable values measured for both the $CsPbBr_3$ and $CsPbI_3$ NCs consistent with literature reports[69]. Although a composition series can be obtained by synthesizing several individual batches with different halide ratios, small differences in the growth kinetics can make it difficult to obtain a full composition series. Anion exchange offers an appealing method to obtain a full composition series from a single $CsPbBr_3$ NC sample without requiring the fine tuning of synthetic conditions at elevated temperatures. Even though the anion exchange reaction is conducted at room temperature with mild reagents, the anion exchanged composition series compares very favorably to the synthesized composition series. The PLQY of the ensembles obtained from anion exchange are comparable, if not slightly higher than the corresponding as-synthesized ensembles (Figure 2.9). This further suggests that the anion exchange using OLAM-X exchange species does not introduce substantial numbers of defects, if any, into the material as the optical performance of semiconductors is highly sensitive to optically active defects. This result is not achievable with all the reported anion exchange species and some result in substantial degradation of the NC ensemble and inferior optical performance[74,75,80]. This ultimately highlights the importance of selecting exchange precursors that are not overly aggressive to achieve the best possible results from these exchange reactions.

Post-synthetic transformations of colloidal NCs offer the potential to finely tune the NC ensemble properties without the need to rely on highly tailored direct synthetic routes. Owing in large part to the defect tolerance and high halide ion conductivity of the $CsPbX_3$ material system, facile anion exchange affords the ability to finely tune the optical bandgap of the NC ensemble across the visible spectrum at room temperature using mild reagents. Impressively, the anion exchange reaction yields NC ensembles with optical properties at least as good, if not better, as the corresponding as-synthesized samples. Additionally, the $CsPbX_3$ NCs maintain their shape and crystallographic phase following the anion exchange, due to a relatively rigid cationic sub-lattice. This facile halide ion exchange presents a tantalizing possibility to extend the lessons learned from this exchange to other halide-containing material systems. However, in order to more finely control these reactions and expand their applicability, a deeper understanding of the underlying kinetics and local mechanism of the exchange process is needed.

2.4: Kinetics of Anion Exchange in $CsPbX_3$ Nanocrystals

Although the phenomenological observation of anion exchange in $CsPbX_3$ NCs offers a facile exchange that is distinct from other nanoscale anion exchanges reported[51,52,66], to fully understand how to broadly apply it to other classes of materials, a detailed study into the mechanism and kinetics is needed. The $CsPbX_3$ NCs are a model system to study nanoscale anion exchange, as the strong luminescence and absorption is maintained at all halide compositions, even while the NCs are actively exchanging halides. The optical properties of the material (Figure 2.2) act as a direct reporter of the material composition throughout the exchange, affording the potential to monitor the dynamics of the exchange with millisecond time-resolution by monitoring the optical properties of the ensemble. By resolving the underlying kinetics of the reaction, a deeper understanding of the process can be gained, potentially identifying other material systems that also undergo similarly facile anion exchanges.

2.4.1: Kinetic Anion Exchange Reaction Conditions

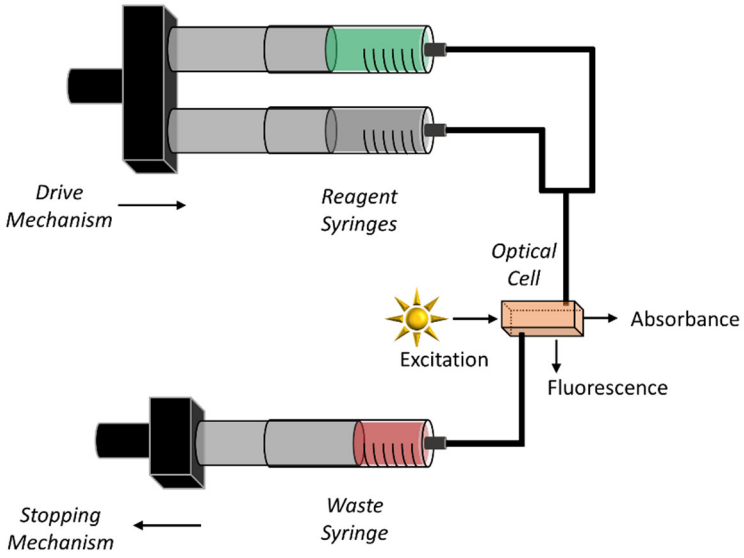

Figure 2.10: Schematic diagram of the SX20 stopped-flow spectrometer. There are two reagent syringes that are driven by a pneumatic cylinder rapidly forcing both solutions through the optical cell. The installed optical cell for the anion exchange kinetics experiments is a 20 µL cell volume.

For the kinetic studies, the nanocrystal synthesis and exchange solutions employed are identical to those for the steady-state anion exchange reactions. The kinetic studies of the anion exchange were conducted within a stopped-flow spectrometer (Applied Photophysics SX20) shown schematically in Figure 2.10. To conduct a kinetic study on these materials, the solution of nanocrystals and the anion exchange solution must be quickly mixed, on timescales faster than the reaction, to ensure a homogeneous reaction environment. Inside a stopped-flow instrument, both solutions are rapidly forced through a mixing chamber and then quickly stopped. Inside the small volume of the mixing chamber, the two solutions can quickly mix with a sub-millisecond mixing time, much faster than the seconds to minutes required for the complete anion exchange. An additional advantage of the stopped-flow spectrometer is that there is an equipped temperature-controlled water bath to stabilize the temperature between 15 °C and 40 °C for these exchanges, within 0.1 °C of the set-point. The water-bath can reach a larger range of temperatures, but the freezing point of the ligands in solution sets the lower bound while the upper bound is determined by the sealing rings used in the stopped-flow spectrometer.

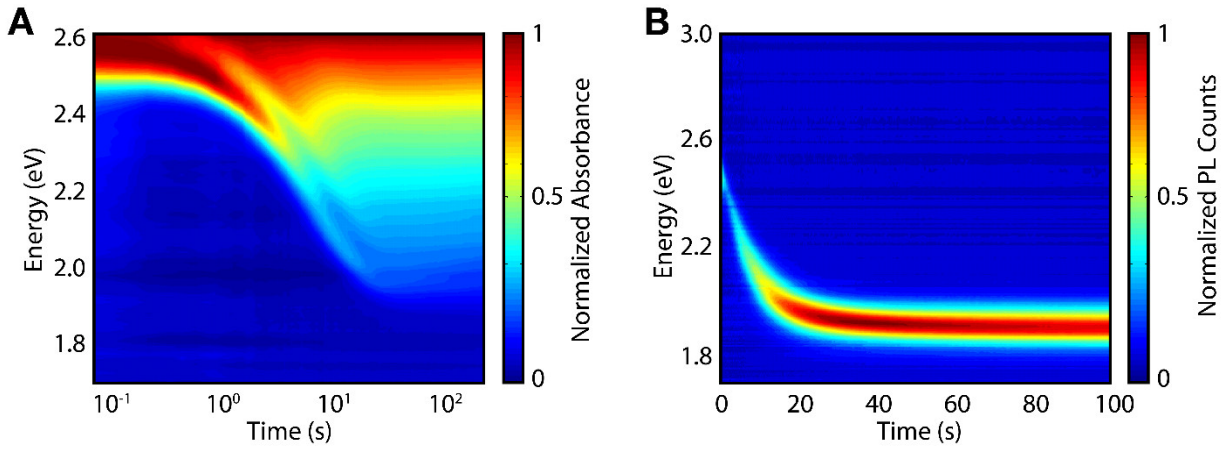

Figure 2.11: Kinetic trajectory of the iodide exchange on $CsPbBr_3$ nanocrystals. (A) Iodide exchange trajectory of $CsPbBr_3$ nanocrystals resolved by monitoring the transient absorption spectrum, with a spectrum collected every 100 milliseconds. (B) Iodide exchange trajectory of $CsPbBr_3$ nanocrystals resolved by monitoring the background free photoluminescence spectrum upon continuous excitation at 375 nm with a spectrum collected every 50 milliseconds.

The combination of sub-millisecond initial mixing times, millisecond spectral acquisition, and strong optical signatures allows reliable resolution of the anion exchange using either absorption or photoluminescence (PL) (Figure 2.11). Although the strong optical properties of the NCs throughout the anion exchange make it possible to monitor the time-evolution by either absorption or PL, the absorption spectra can include significant contributions from scattering. In addition, the weakly quantum-confined nature of the $CsPbX_3$ NCs further complicate interpretations using the measured absorption spectra. Instead, this discussion will focus on using the back-ground free PL of the NC ensemble as the optical handle to monitor this reaction. Interpretations from the time-resolved changes in the PL spectrum will focus on changes in PL position and PL linewidth under UV-excitation at 365 nm, rather than the PL intensity as our current instrument setup is not able to normalize for changes in absorption. For these exchanges, like the direct synthesis[69,73–75], transient NPs with halide compositions of Br/Cl or Br/I can be observed in both the forward and reverse directions, whereas the Cl/I are not miscible in the solid-state and unable to be observed optically.

2.4.2: Kinetics of $CsPbX_3$ Nanocrystal Anion Exchange Discussion

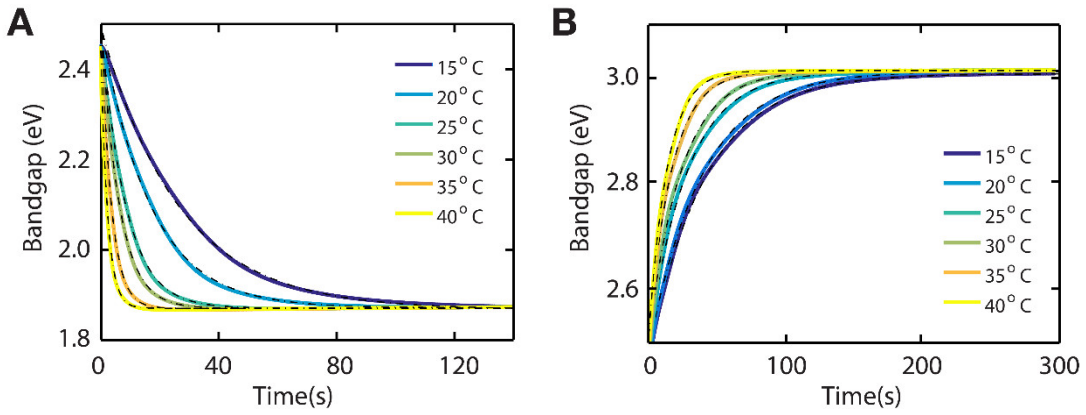

Figure 2.12: Temperature-dependent time progression of the anion exchange. (A) Band gap change over time during the iodide exchange of $CsPbBr_3$ nanocrystals monitored between 15 and 40 °C, in which dotted lines represent a single exponential fitting equation. (B) Band gap change over time during the chloride exchange of $CsPbCl_3$ nanocrystals monitored between 15 and 40 °C, in which dotted lines represent a bi-exponential fit. Both reactions were monitored until completion of the exchange reaction and excited at 375 nm.

The transformation of a sample of $CsPbBr_3$ NCs to either $CsPbCl_3$ or $CsPbI_3$ can be monitored to resolve how the anion identity influences the local exchange dynamics with a time resolution on the scale of 10s of milliseconds, limited by the read-out speed of the silicon-CCD spectrometer used for these measurements. Each anion exchange presents a rich dataset to analyze and resolve the underlying exchange dynamics, including the position and width of the PL spectrum, both providing useful details about the exchange. By first focusing on the trajectory that the average NC in the ensemble takes during the exchange, plots of the exchange can be made by monitoring the evolution of the PL peak position at varying temperatures (Figure 2.12). The iodide exchange presents a systematically red-shifting bandgap with time that can be well-fit by a single-exponential equation, whereas the chloride exchange displays the expected systematically blue-shifting bandgap over time but is not as well-described by a single exponential fit (Figure 2.12).

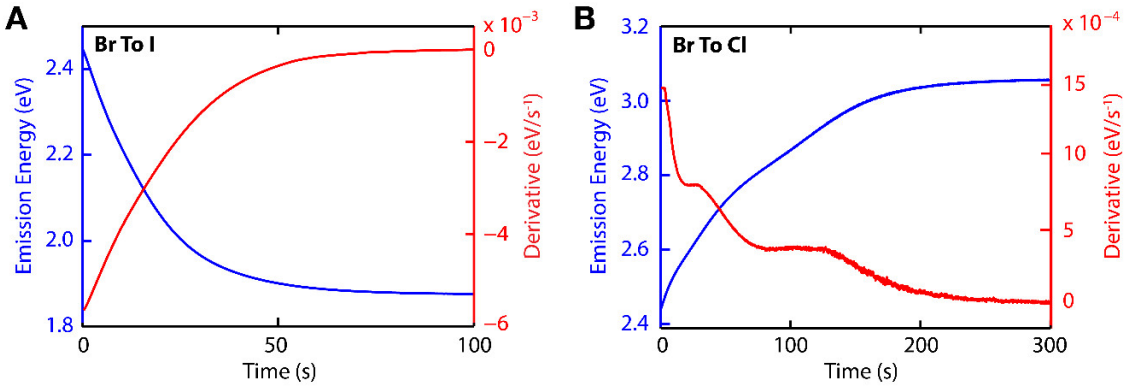

Figure 2.13: Time progression of the band gap throughout the anion exchange reactions. (A) Time-dependent band gap of a $CsPbBr_3$ to $CsPbI_3$ anion exchange reaction overlaid with the derivative of the exchange, displaying an exponential function. (B) Time-dependent band gap of a $CsPbBr_3$ to $CsPbCl_3$ anion exchange starting with the same initial nanocrystal sample, also overlaid with the derivative of the exchange, displaying regions with constant band gap change.

Although the deviations can be subtle when observing the change in the band gap over time, the disparate nature of these exchanges can be more clearly seen in the rate of band gap change, the first derivative of the band gap trajectories in (Figure 2.13). From these plots it is apparent that the derivative for the iodide exchange trajectory is yet another exponential (Figure 2.13), the expected result for the single exponential nature of the trajectory. However, the chloride exchange presents a more complicated exchange trajectory derivative with discrete constant slope regions with differing rates of exchange (Figure 2.13).

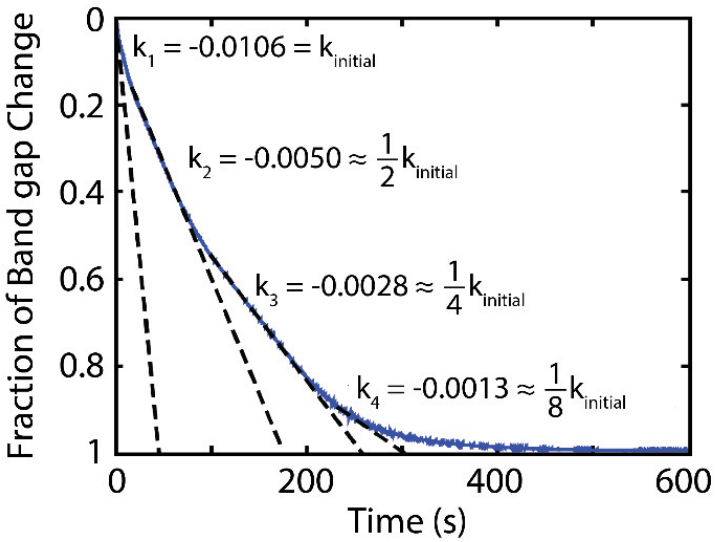

Figure 2.14: Constant rate regimes of the chloride exchange reaction. The exchange curve is overlaid with lines associated with the constant rate of band gap change regions. There is an approximate rate scaling, in which a constant rate region has a rate that is one-half the previous constant rate region. The data shown is for a 11.5 nm average sized sample for ease and clarity, although this trend also occurs for all tested sizes of $CsPbBr_3$ nanocrystal samples between 6.0 and 11.5 nm edge lengths, the typical region that are being actively researched.

Particularly notable is the rate scaling of the constant bandgap change regimes, in which a constant exchange rate regime is one-half of the preceding regime (Figure 2.14). For the exchange trajectory shown in (Figure 2.14), there are four distinct rate regimes present that have transitions that occur after 4%, 36%, and 67% respectively. The specific origin of these rate transitions still needs further investigation to identify their origin. However, the orderly fashion that the rate changes suggests that there are systematic differences in the energetics of different sites within the NCs, such as what might be expected for successive layers within a NC or for differences in energies of corner, edge, and surface sites within these materials.

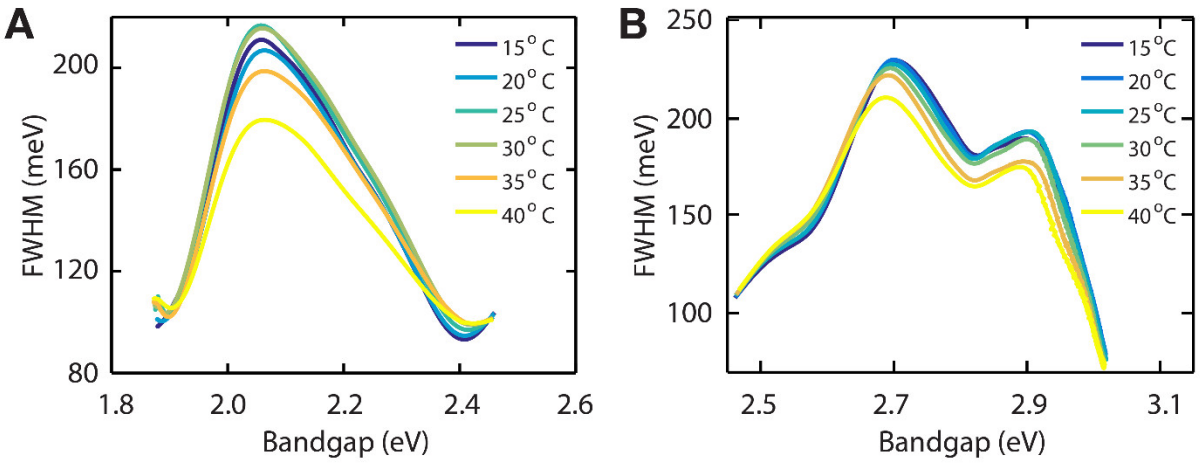

Figure 2.15: Temperature-dependent change in the PL linewidth during the anion exchange. (A) PL linewidth change over time during the iodide exchange of $CsPbBr_3$ nanocrystals monitored between 15 and 40 °C. (B) PL linewidth change over time during the chloride exchange of $CsPbCl_3$ nanocrystals monitored between 15 and 40 °C. Both reaction sets were monitored until completion of the exchange reaction and excited at 375 nm for the same initial sample of $CsPbBr_3$ nanocrystals.

While the preceding discussion focused on the trajectory that the average NCs of the ensemble take during the anion exchange, the change in the ensemble PL linewidth is indicative of changes that occur to the whole ensemble throughout the exchange reaction. For the iodide exchange there is a single prominent broadening event, once again consistent with a single rate-limiting step to the exchange (Figure 2.15). The presence of the two small linewidth narrowing events before and after the single prominent broadening are related to the size-dependent nature of the exchange and will be explained by a model later in the text. As opposed to the iodide exchange, the chloride exchange has several distinct broadening events, consistent with the notion of a more complicated multi-step exchange reaction (Figure 2.15). However, the same features appear irrespective of temperature tested, suggesting a consistent sequence of reaction steps that take place during the exchange reactions.

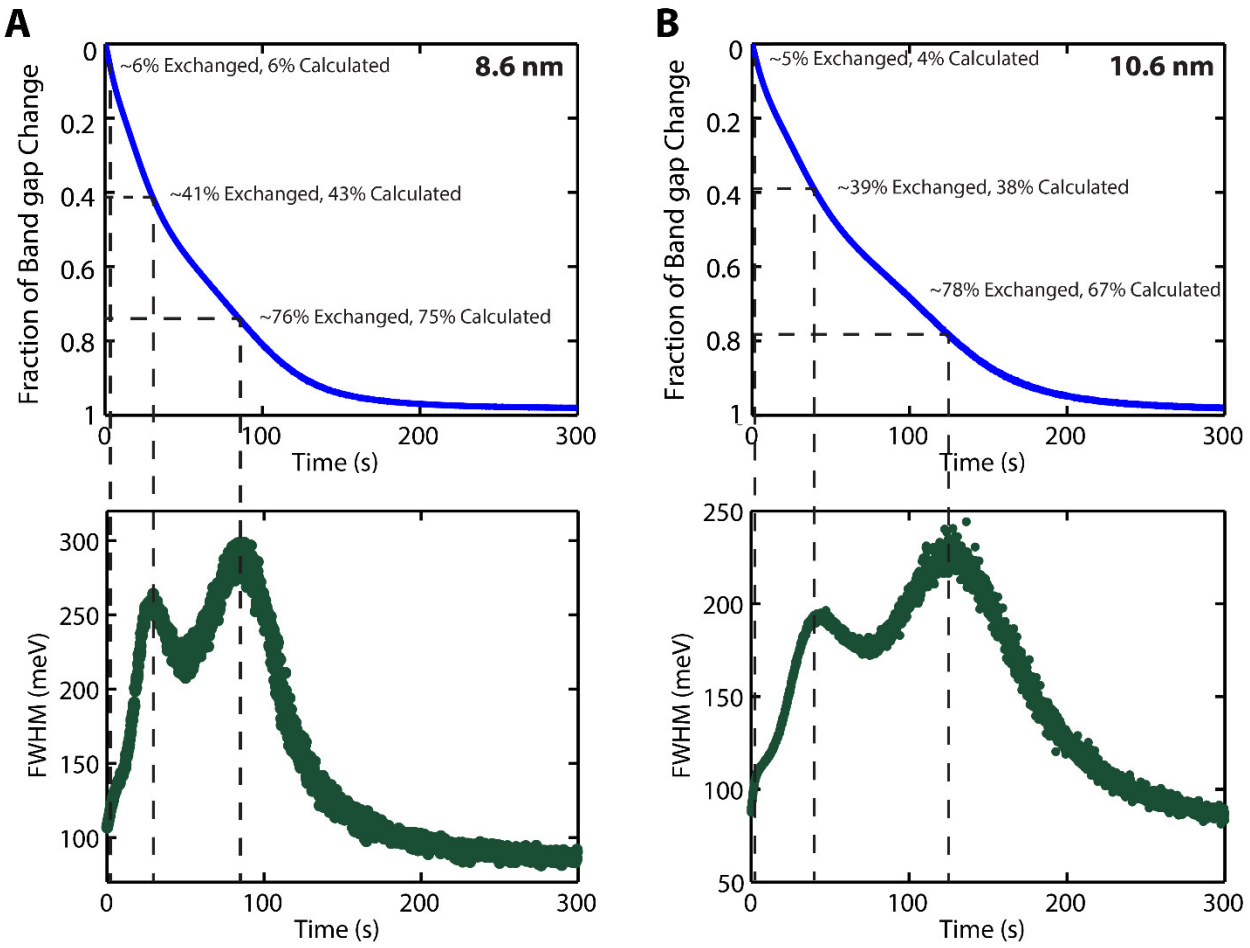

Figure 2.16: Time progression of representative chloride anion exchanges. Shown are a chloride exchange trajectory for an (A) 8.6 nm average size $CsPbBr_3$ and (B) 10.6 nm average sized $CsPbBr_3$ nanocrystals. Plotted are the change in bandgap with time and the derivative overlaid. Shown are the correlations between the constant bandgap regions and the change in the PL linewidth with time. Dashed lines are guides to the eyes.

The distinct changes in the ensemble PL linewidth for the chloride exchange occur when the rate of exchange transitions from one constant rate of exchange regime to the next constant rate of exchange regime (Figure 2.16), at least for the sizes of NCs tested. The appearance of this correlation suggests that the underlying exchange mechanism of the chloride exchange of $CsPbBr_3$ nanocrystals occurs over multiple steps. However, since the exchange presents the same features irrespective of temperature (Figure 2.15) or size (Figure 2.16), other than changing the rate of exchange slightly, suggests that the anion exchange reactions proceeds via the same mechanism, allowing comparisons to be reasonably drawn. The disparate nature of these two exchange trajectories likely stems from differences in anion size and mobility, a model that probes this exchange interpretation is presented later.

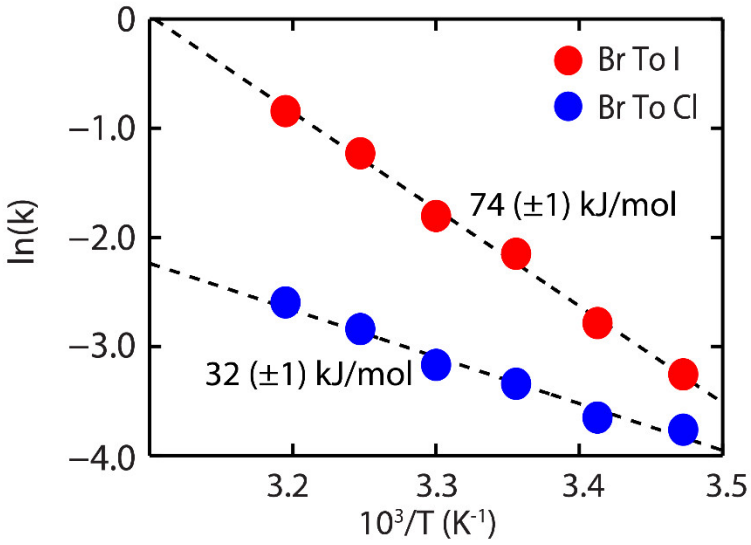

Figure 2.17: Arrhenius plot fit for the temperature-dependent rate of anion exchange. Shown are the rates of exchange for the chloride and iodide exchange of $CsPbBr_3$ nanocrystals between 15 and 40 °C. The Arrhenius plot fit is shown by the dashed line and the extracted activation energy is shown in the plot for each exchange.

Since there is a consistent set of mechanistic steps, the kinetics of the exchange can start to be probed to gain a deeper insight into the exchange mechanism. Both the iodide and chloride anion exchange of $CsPbBr_3$ NCs were conducted on a set of samples from the same NC synthesis batch and monitored at a series of temperatures between 15 and 40 °C to probe the activation energies of the anion exchange routes. From each of the temperature-dependent exchange reactions the rate of the exchange was extracted. The iodide exchange was fit with a single-exponential equation and the rate constant directly extracted, whereas the chloride exchange was fit with a bi-exponential equation and the weighted average of the exponential components used as the rate of the exchange. Although the initial rate of bandgap changes increases by a factor of 5 between 15 and 40 °C, the extracted temperature-dependent rates of exchange are well-described by an Arrhenius relation (Figure 2.17). Both exchanges present a positive activation energy, 32 (±1) kJ/mol for the chloride and 74 (±1) kJ/mol of the iodide exchange. It is important to note that the measured rates are for the change in the ensemble band gap, an imperfect description for fully understanding the kinetics. With the rapid solid-state diffusion in the iodide exchange, a linear correlation to the actual reaction rate can be made, whereas a more complicated, non-linear, dependence exists for the chloride exchange which prevents a conversion to the actual reaction rate. However, while the interpretation of complex reaction activation energies is not straightforward without a detailed kinetic model of the many atom, multistep exchange process, the presence of a positive activation energy is telling. A positive activation energy suggests that the mechanism of exchange does not involve activated complexes or surface adsorption equilibria, both situations that present negative apparent activation energies[87].

To begin to build up the necessary multi-atom, multistep exchange process to make interpretations of the exchange thermodynamics, careful investigations of the transient distributions of halide ions within the NC throughout the exchange are highly informative to the underlying processes. Though informative, detailed structural characterization of the transient

exchanging NCs in real-time is currently not possible using conventional structural characterization techniques due to the low barrier to solid-state diffusion and negligible thermodynamic difference between different halide ions within the lattice. Accordingly, exchanges cannot be quenched and isolated for careful characterization because the barrier for diffusion is so low[77,78,84] that only homogenously steady-state alloys can be observed at room temperature.

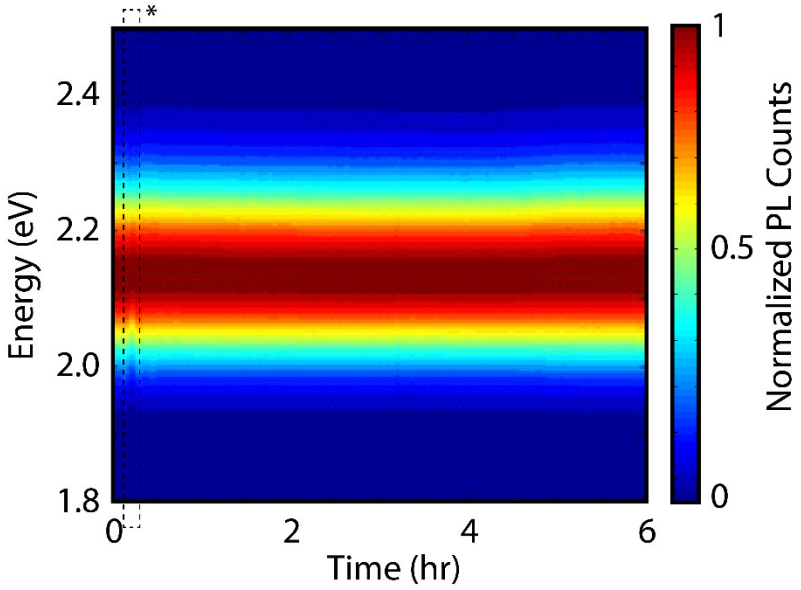

Figure 2.18: Kinetically trapped exchanging nanocrystals at cryogenic temperatures. Although the low barrier to solid state diffusion allows for rapid alloying, by rapidly quenching to cryogenic temperatures the transient particles can be trapped. Shown is the photoluminescence spectra over a period of six hours. Initially the sample was pure phase $CsPbBr_3$, presenting an emission at around 2.4 eV. Enough iodide exchange solution was added for a nearly complete exchange to $CsPbI_3$ with nearly a 1.9 eV emission. The sample was quenched during the exchange to 80 K and left at that temperature while PL spectra were collected under 375 nm illumination. After the test, the sample was warmed to room temperature and the exchange continued resulting in the expected ensemble with a 1.9 eV band gap. After an hour there is a small optical feature (*) that appeared due to a change in the optical collection efficiency of the fiber optic setup when the liquid nitrogen bath was re-filled, an optical artefact that does not emerge from a change in the ensemble.

However, since alloying is a solid-state diffusion process, the kinetic structures can be trapped by first initiating the exchange reaction and then rapidly quenching to cryogenic temperatures (80 K) (Figure 2.18). Although given enough iodide to nearly fully exchange the $CsPbBr_3$ NC ensemble at room temperature (2.5 eV to 1.9 eV), by quenching to cryogenic temperatures an intermediate composition that would not be possible at room temperature can be isolated and remain stable for many hours (Figure 2.18). Once the sample is warmed back to room-temperature the exchange continues to completion, meaning that we have only slowed down the anion exchange to a stand-still instead of completely changing the trajectory that the exchange takes. These kinetically trapped NCs can be investigated to look for optical signatures of kinetic structures, namely distinct changes in the PL lifetimes. Importantly, in order to ensure that the measured PL lifetimes were representative of changes in the NC structure and not simply differences in the nonradiative pathways, the cryogenic PLQY of the kinetic structures and equilibrium structures were measured. Comparing the measured cryogenic PLQYs of the kinetically trapped and steady-state allows with that have the same optical bandgap, there are no

distinct difference in the measured efficiencies. This shows that the nanocrystals do not suffer from any additional optically active defects caused by the exchange itself, consistent with the mild nature of the exchange.

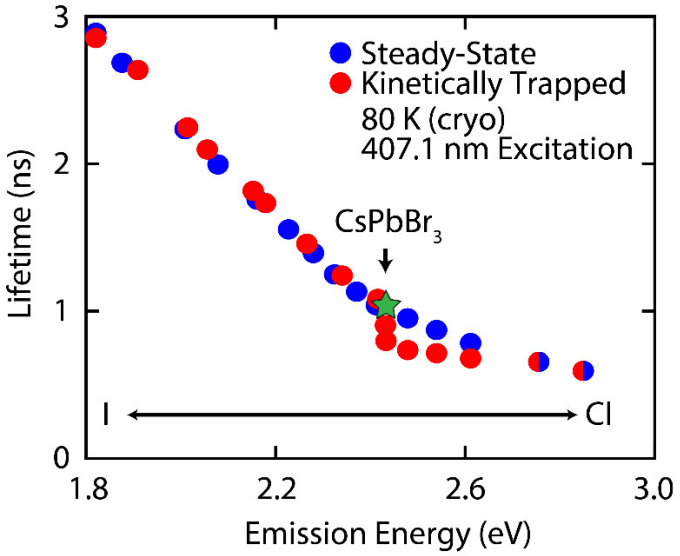

Figure 2.19: Cryogenic lifetimes of steady-state and kinetically trapped nanocrystals. Shown is the composition dependent lifetime under pulsed 407.1 nm excitation at cryogenic temperatures (80 K) for both a set of steady-state alloys and kinetically trapped nanocrystals.

Observing the PL lifetime at different points along the exchange, there are no significant differences between the PL lifetimes of the kinetically trapped and steady-state alloys for the iodide exchange (2.5 eV to 1.8 eV), even though the NCs are actively exchanging halides when they were cryo-quenched and kinetically trapped (Figure 2.19). Therefore, during the iodide exchange of $CsPbBr_3$, the NCs can rapidly alloy on timescales faster than the anion exchange yielding NCs that are solid-state alloys, meaning ultimately that the iodide exchange reaction is not limited by solid-state diffusion but instead by surface reactions. This behavior is along the lines expected for typical ion exchanges at the nanoscale[53,54,59–65], a behavior consistent with a reaction zone that has a size comparable to the size of the NC, if not larger. In contrast to the iodide exchange, the chloride exchange of $CsPbBr_3$ shows distinct deviations of the kinetically trapped NCs compared to the steady-state alloys (2.5 eV to 2.9 eV) (Figure 2.19). This deviation suggests the transient structure during the anion exchange is not a solid-state alloy but instead a more complicated, yet undetermined, kinetic structure. Surprisingly, during the chloride exchange the PL lifetime of the ensemble changes by 20% before the PL bandgap of the ensemble changes at all.

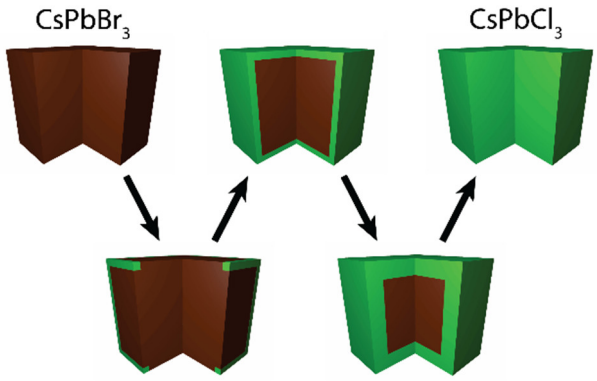

Figure 2.20: Schematic depiction of the chloride zone-by-zone anion exchange. In this schematic diagram the chloride reaction front begins at the nanocrystal surface and proceeds in ward, replacing bromide as it progresses.

This behavior suggests that the chloride exchange is diffusion-limited with a reaction zone that is smaller than the size of the NC (Figure 2.20), even NCs with edge lengths less than 6 nm show the same behavior. A diffusion-limited exchange is analogous to previously described extended surface reactions in bulk crystals[53,56–58] as opposed to the surface-limited exchanges typically described for nanoscale exchanges. The emergence of a reaction zone during the chloride exchange suggests that the reaction zone is at most 3 nm, but perhaps smaller, is surprising for a nanoscale crystallite. It is notable that the nanoscale anion exchange differs kinetically depending on the targeted halide of interest, despite the analogous nature of the thermodynamic steady-state alloy structures.

One potential explanation for the mechanistic difference is a change in the lead-halide bond strengths, specifically that chloride forms a stronger bond than iodide to lead[77,78]. This strength might be able to dictate how easily a halide ion can diffuse through the lattice. An alternative explanation is that this mechanistic discrepancy arises due to the difference in size of the target halide entering the lattice compared to the size of the halide already present in the lattice. For these exchanges, the incoming iodide is 13% larger (206 pm) than the bromide (182 pm), causing the lattice to likewise expand to accommodate the iodide anions. On the other hand, the incoming chloride is 8% smaller (167 pm) than the bromide (182 pm), causing the lattice to contract. By contracting the lattice, the chloride anion exchange might become non-cooperative in nature, presenting a barrier for new chloride ions from solution to insert into the lattice and for bromide ions already in the lattice to be extracted from within the interior of the nanocrystal. Therefore, given that the reaction front progresses from the outer regions of the NC and progresses inward (Figure 2.20), the discrete transitions in the exchange rate can be interpreted with a reaction zone-based model, in which zones are created by layers of material with different halide richness throughout the crystal.

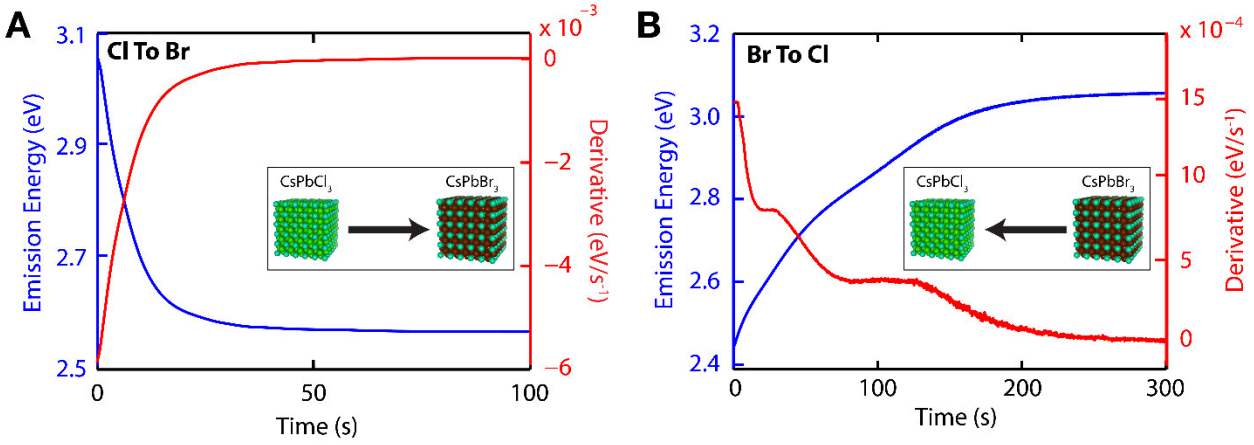

Figure 2.21: Time progression of the band gap throughout the bromide exchange of $CsPbCl_3$. Shown is a comparison of the (A) bromide exchange of $CsPbCl_3$ and the (B) chloride exchange of $CsPbBr_3$. The comparison highlights the dissimilar nature of the anion exchange depending on the halide within the lattice and the halide to be exchanged.

For a reaction zone-based mechanism that arises from differences in anion size, it is not the identity of the halide that matters but rather the relative difference in halide size. Under this interpretation, there should be a distinct difference in the exchange trajectory depending on the direction of the exchange reaction, i.e. a chloride exchange of $CsPbBr_3$ compared to a bromide exchange of $CsPbCl_3$ would look different. Consistent with this interpretation, the bromide exchange of $CsPbCl_3$ follows an analogous trajectory to the iodide exchange of $CsPbBr_3$ (Figure 2.21), with the trajectory of the exchange well described by a single-exponential fit. Given the similarity of the bromide exchange of $CsPbCl_3$ and the iodide exchange of $CsPbBr_3$, this suggests that the change in exchange trajectory arises critically from changes to the local lattice size during the anion exchange rather than the chemical identity of the halide. The influence that different bond strengths from the different halide species have on the trajectory cannot be conclusively ruled out and will need to be further investigated to understand the extent of their relevance to the anion exchange. Regardless of the origin, depending on the conditions of the exchange reaction, the exchange mechanism can be changed from surface-reaction limited to diffusion limited, a surprising observation for a nanoscale crystallite. Under this interpretation, $CsPbX_3$ NCs with non-thermodynamic distributions of halide, i.e. NCs that do not present solid-state alloys, can be accessed. These non-alloyed materials are inaccessible materials from direct synthesis methods, representing a unique aspect of the anion exchange reactions.

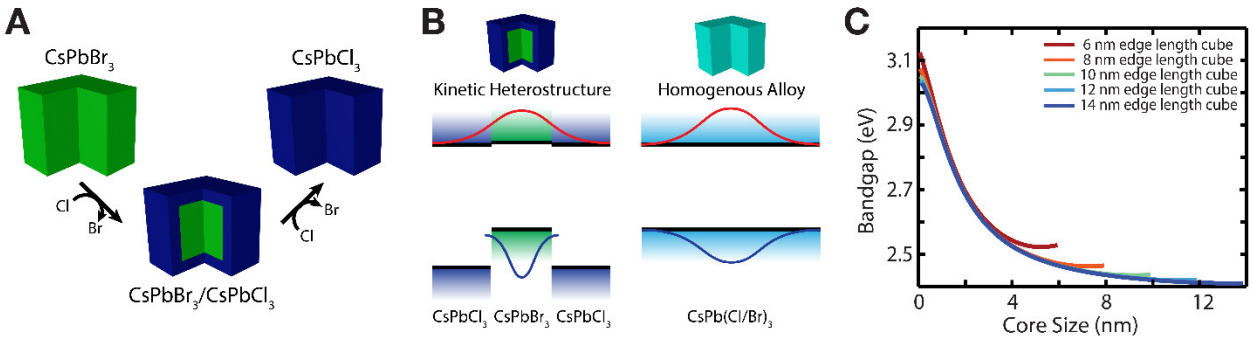

Figure 2.22: Proposed transient heterostructures formed during the chloride exchange. (A) Schematic depiction of the transient formation of $CsPbBr_3/CsPbCl_3$ core/shell heterostructures as a result of the anion exchange reaction. (B) Band alignment of the proposed kinetic heterostructures compared to the homogeneous alloy, not shown to scale. (C) Expected change in the ensemble band gap with changing the core and shell thickness.

A potential non-alloy transient structure that might be formed consistent with the chloride exchange interpretations is a core/shell heterostructure with the core composed of predominately $CsPbBr_3$ and the shell composed predominately of $CsPbCl_3$ (Figure 2.22). The band alignment of this potential heterostructure has not been previously described but would likely represent a quasi-type II band alignment[88] in which the electron wavefunction is delocalized over the whole nanoparticle whereas the hole wavefunction is largely localized in the $CsPbBr_3$ core (Figure 2.22). For such a structure, the resulting core/shell particles can be modeled using an effective mass model assuming hard interfaces at the core/shell interface, consistent with the schematic depiction in (Figure 2.22). The change in the bandgap as a function of core size presents a characteristic shape (Figure 2.22), showing that the bandgap would change very little as the core begins to shrink, a result of the charge carriers having a slightly higher effective mass in the shell and the NCs being in the weak confinement regime. However, this relatively simple toy model assumes hard-well potentials, neglects electron-hole interaction, and completely ignores spin (a potentially significant effect for lead based semiconductors), whereas the exchange probably proceeds through an alloyed interface. These effects would represent corrections to the extreme case of hard-interface core shells, but qualitatively the formation of heterostructures would still result in a non-linear change in the optical properties with composition. The formation of transient heterostructures might help to explain how the optical properties evolve during the $CsPbBr_3$ to $CsPbCl_3$ anion exchange reaction, and these transient structures might have interesting optical properties that can be further investigated to understand the photophysics of these materials further.

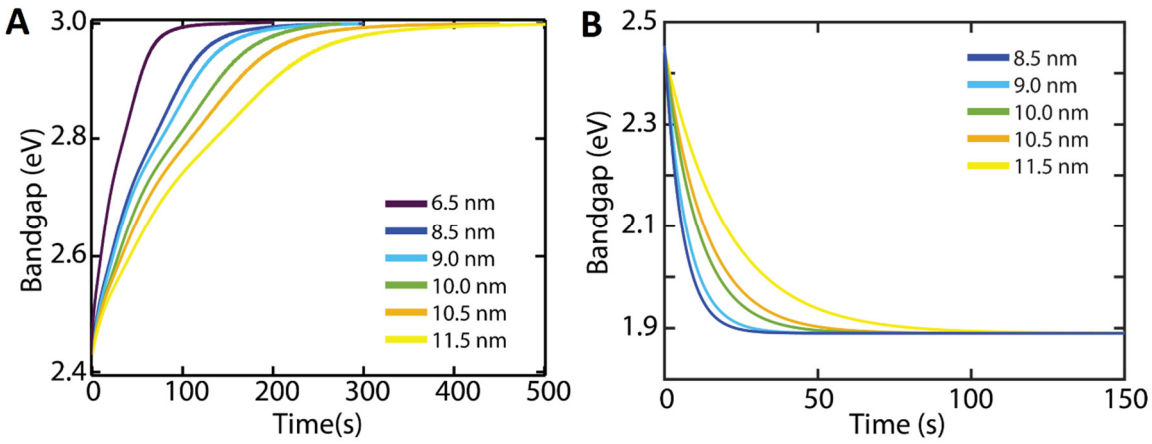

Figure 2.23: Size-dependent bandgap trajectories during the anion exchange. Shown are the changes in band gap during the anion of exchange of $CsPbBr_3$ to (A) $CsPbCl_3$ and to (B) $CsPbI_3$. Each of the exchanges were conducted at the same concentration of nanocrystals and anion exchange solution, while maintaining a constant temperature of 20 °C for the anion exchange reactions.

Although the kinetic descriptions start to explain how an individual NC evolves during the exchange reaction, it does not fully capture the details of what the ensemble does throughout the exchange. By understanding the size-dependence to the exchange rate, the origin of the broadened kinetic regime linewidths (Figure 2.23) can be further investigated, checking to see if a simple model can grant insight into the rather complicated observed trajectories. In general, the size distribution of the equilibrium NC ensemble dictates the ensemble PL linewidth, with each differently sized NC emitting at a slightly different energy with their single particle PL linewidth[81,89]. Due to quantum confinement effects, the smallest quantum dots will also have the highest energy bandgap in the ensemble, and likewise the largest quantum dots will have the lowest energy bandgap in the ensemble. As such, the linewidth of the actively exchanging NC ensemble will also change as a result of the size-dependent exchange rate (Figure 2.23), in which smaller NCs exchange faster than larger NCs.

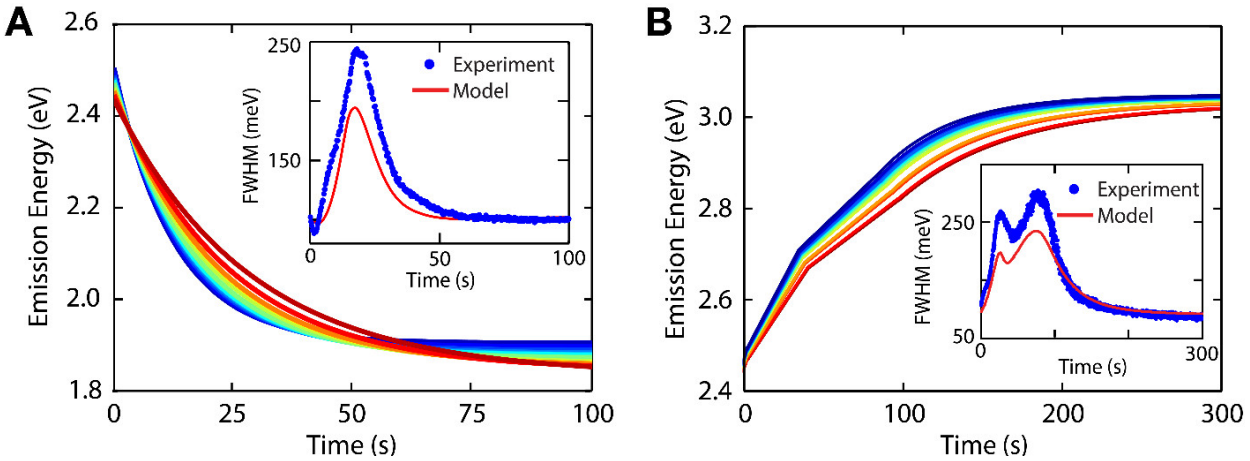

Figure 2.24: Model of the anion exchange reactions. Shown are the model results compared to the experimental results for the $CsPbBr_3$ exchange to (A) $CsPbI_3$ and to (B) $CsPbCl_3$. Both figures contain an inset figure comparing the experimental and model linewidth changes, whereas the main figure shows the single particle exchange trajectories that are consistent with experimental results.

A model of the exchange can be constructed to understand how these size-dependent factors manifest themselves in the changing ensemble during the anion exchange. For this model, the size-dependent characteristics, including the single particle linewidth[81,89], are assigned to a normal distribution of particle sizes in accordance with the observed size distributions from TEM sizing. The normal distribution of particles is then allowed to exchange halide ions with a rate consistent with the measured size-dependent exchange rates. From these simulated exchange trajectories, the experimentally observed change in band gap position and PL linewidth is qualitatively reproduced (Figure 2.24). The model suggests that during the iodide exchange, the band gap of the smaller and more quickly exchange NCs overlap the larger and more slowly exchanging NCs, resulting in a minimum in the PL linewidth at early times (Figure 2.24). The maximum linewidth in the iodide exchange occurs when the smallest and largest NCs have as different of a bandgap as possible, again the result of size-dependent anion exchange rates. Finally, when the smaller NCs are fully exchanged, reaching their steady-state band gap, the larger NCs are still actively exchanging. The second minimum occurs as the band gap of the larger NCs overlaps the smaller NCs and the linewidth returns to the expected value based on the size distribution (Figure 2.24). The story is analogous for the chloride exchange, expect the bandgap of the smaller NCs does not overlap with the larger NCs at any point during the exchange. The local minima and maxima of the linewidth change occurs when the chloride exchange transitions between constant exchange rate regimes. By transitioning through these regimes there are periods where the bandgap of the smallest and largest NCs in the ensemble are closer and further apart from each other. The size-dependent exchange rate can provide context for how the ensemble changes throughout the exchange (Figure 2.24). Importantly, the ability for these relatively simple models to capture the rather complicated exchange trajectories suggests that most of the chemistry of the system is captured without needing to employ more complicated models.

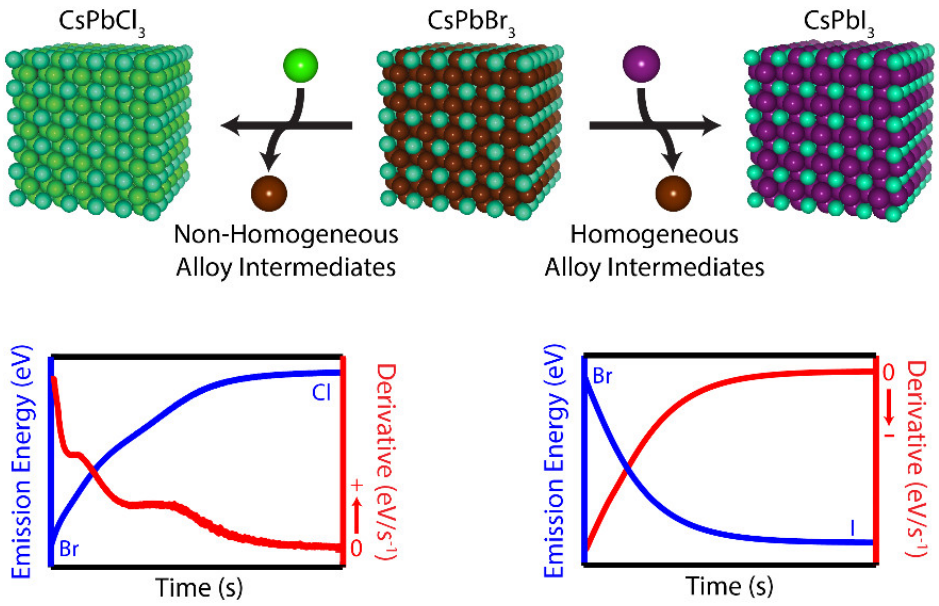

Figure 2.25: Schematic depiction of the anion exchange results. Shown are the different pathways that emerge from the anion exchange reactions of $CsPbX_3$ nanocrystals depending on the size of the incoming halide relative to the existing halide in the lattice.

In conclusion, the excellent optical properties of the $CsPbX_3$ NCs even while actively exchanging halide anions allow the exchange trajectory to be monitored in situ by optical methods. Optical measurements on the millisecond timescale resolve the reaction kinetics and provide insight into the exchange dynamics. Exchanges in which larger halide anions enter the lattice, such as the iodide exchange of $CsPbBr_3$ NCs, present surface-limited reactions allowing the NC to alloy on timescales faster than the anion exchange (Figure 2.25). On the other hand, exchanges in which smaller halides enter the lattice such as the chloride exchange of $CsPbBr_3$ NCs, present diffusion-limited reactions leading to the emergence of zones of exchange analogous to bulk materials (Figure 2.25). This disparate nature appears to arise from the relative sizes of the target halide versus the lattice halide instead of an intrinsic difference in cohesive binding energies. However, as a result of these zones of exchange, transient structures are created with optical properties that are disparate from steady-state alloys with the same band gap energy. This provides a possible path to kinetically trapped structures that are not possible in the steady-state due to a low barrier to solid-state diffusion in the materials.

2.5: Future Directions

It has been shown that depending on the relative sizes of the target exchange halide and the existing halide within the crystal lattice, two distinct exchange mechanisms occur. In one a kinetic structure is created that is distinct from the steady-state alloys. These transient structures could be interesting materials to investigate further to better understand the photophysics of these materials and the impact that non-uniform halide distributions have on the optical properties. Additionally, although the structural characterization of these transient NCs is not currently possible with conventional techniques, a detailed understanding of the time-evolution of the halide distribution within the material could be very informative and might be possible using structural characterization techniques at cryogenic temperatures. The unique nature of the anion exchange in $CsPbX_3$ NCs places the material in a unique and favorable position for detailed mechanistic studies of nanoscale ion exchange. While these experimental measurements suggest that there is no thermodynamic preference to have different halide ions in the lattice, small thermodynamic differences between the different halides have been measured in bulk studies. Systematically investigating this difference using much more sensitive measurement techniques might further yield interesting thermodynamic insights into these reactions and increase the level of control over these reactions. Lessons learned from these anion exchanges can inform rational approaches to exchanges in other halide perovskite materials and other halide-containing materials in general, likely the subject of future investigations.

Chapter 3 - Post-synthetic Selective Etching of $CsPbBr_3$ NCs for Near-Unity Emitters

*The following discussion is adapted from Koscher, B.A., Swabeck, J.K., Bronstein, N.D., Alivisatos, A.P., Essentially Trap-Free $CsPbBr_3$ Colloidal Nanocrystals by Postsynthetic Thiocyanate Surface Treatment, J. Am. Chem. Soc., **2017**, 139, 6566-6569 and from un-published results.*

3.1: Optical Performance of As-Synthesized $CsPbBr_3$ Nanocrystals

Lead halide perovskites are being intensely researched as promising optoelectronic materials for photovoltaics[90,91], photodetectors[92,93], and light-emitting diodes[94,95]. The excellent optoelectronic properties and facile synthetic preparation of these materials have led to the rapid emergence of cesium lead halide ($CsPbX_3$; X = Cl, Br, I) nanocrystals (NCs) as important potential materials for next-generation optoelectronic devices. Additionally, the fast-radiative rate and narrow linewidths of some compositions are potential candidates for controllable and wavelength-tunable single photon sources[81,89]. Using colloidal synthesis techniques, $CsPbX_3$ NC ensembles have been synthesized displaying photoluminescence quantum yields (PLQYs) of up to 90%[55,69] and narrow emission line widths without requiring the overgrowth of an epitaxial shell typically required for high PLQY metal-chalcogenide NCs[42]. The unusually quick success in producing $CsPbX_3$ NC ensembles with 90% PLQYs is overall very encouraging, but this also naturally raises questions regarding the remaining efficiency loss pathways present in the material and what is currently limiting the luminescence efficiency. There is an outstanding opportunity to investigate the non-radiative losses of these materials at the atomic level to understand how the local atomic environment influences the optical performance and then further employ synthetic chemistry technique to reliably improve the optical performance.

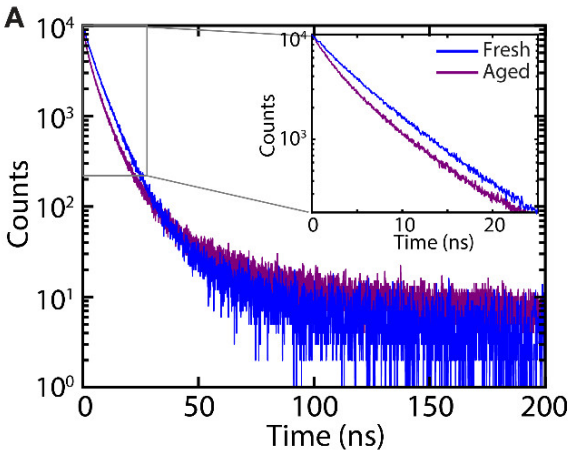

Rates and Efficiencies

	QY (%)	τ (ns)	k_r (ns^{-1})	k_{nr} (ns^{-1})
Fresh Sample	92±2	5.55	0.165±0.004	0.014±0.004
Aged Sample	63±2	4.44	0.142±0.004	0.083±0.004

Figure 3.1: Time-resolved PL lifetimes comparing fresh and aged $CsPbBr_3$ samples. (A) Shown is the change in the ensemble lifetime as the $CsPbBr_3$ sample ages with inset highlighting the difference that emerges in the early decay time region. (B) Table comparing the quantum yield (QY), lifetime (τ), radiative (k_r), and non-radiative (k_{nr}) recombination rates of the fresh and aged samples.

There has been an on-going debate in the literature attempting to understand the origin of the excellent optical performance in the $CsPbX_3$ NCs. Most explanations point to an unusual defect

tolerance that arise from either the ionic nature of the material or the orbital composition that are responsible for the optical transitions[70–72]. However, it has become clear that while the lead halide perovskites are defect tolerant, they are not defect impervious[96–99], as several theoretical and experimental studies have suggested the potential presence of non-negligible defects. The impact of these defects can be readily seen in the sub-unity PLQYs and extended multicomponent excited state photoluminescence decay dynamics[55,67–69,98], typical of the as-synthesized ensembles (Figure 3.1). Due to the large surface-area to volume ratio, the impact of surface defects at the nanoscale can severely influence the optical performance of NCs. Something as simple as letting the $CsPbBr_3$ NCs age in solution causes the PLQY to drop from 90% to 70% or lower (Figure 3.1) after only a few months.

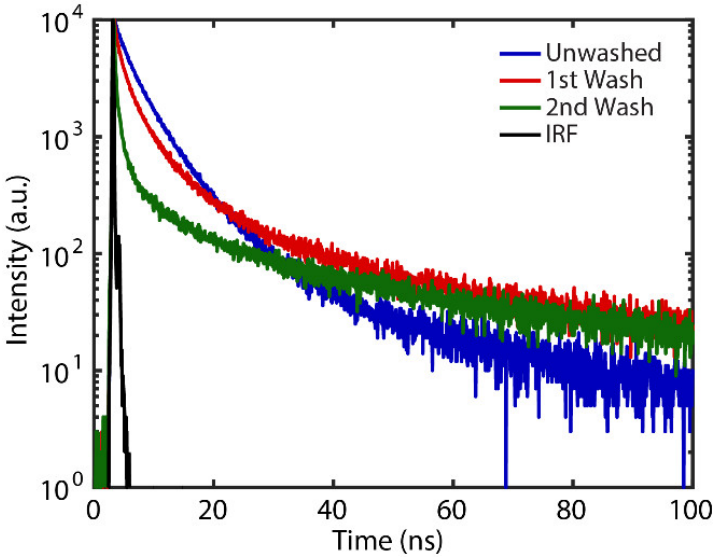

Figure 3.2: Change in the ensemble PL lifetimes through sequential cleaning steps. Shown are the lifetimes for ensembles that are washed with anhydrous ethyl acetate to remove excess ligand and ODE from solution. Through sequential washing steps the long-lifetime component of the overall decay becomes pronounced. Between the unwashed and second washing of the ensemble, the quantum yield has decreased by nearly a factor of 1000x, strongly convoluted with the instrument response function (IRF). A third washing step was attempted but the sample was not measurable optically.

One critical difference between the lead halide perovskites and the typical metal-chalcogenide NCs is the strength of the surface bound ligand passivating species. The oleylammonium halide surface ligands, are significantly more dynamic and weakly bound to the lead halide perovskite NC surface than the ligands of metal-chalcogenide NCs[41,100,101]. As such, post-synthetic processing such as the traditional anti-solvent-based purification approach caused the PLQY to drop by a factor of 1000x, precipitating with ethyl acetate and re-suspending in hexanes, after just two cleaning cycles (Figure 3.2). This PLQY deterioration is indicative of inadequate surface passivation that naturally becomes worse over time, something that might ultimately limit the widespread usage of these materials. In order to access materials performing near their efficiency limits, the development of robust chemical passivation strategies that are capable of mitigating the optoelectronic consequences of these optical defects are important to improve the performance of these materials above the as-synthesized efficiencies.

Although the weak internal chemical bonding of the lead halide perovskites enables facile synthesis under mild conditions and contributes to unusually high ionic mobilities[55,77,78], it also results in long-term stability issues and increases the material susceptibility to defect formation[70,71,96]. This susceptibility is further increased as a result of the lead-rich synthesis conditions, which calculations suggest changes the enthalpy of formation of the potential defects present in the material making a bromine vacancy the easiest defect to access[70,96], in addition to the lability of surface-bound oleylammonium halide[100], which over time decreases the number of halides on the NC surface. Given the overall conditions that the NCs are exposed to, the presence of a lead-rich NC surface that arises from the presence of halide vacancies would not be surprising and is quite likely. A bromine vacancy is problematic because it leaves behind an under-coordinated lead atom, a defect that has been calculated to introduce a somewhat localized shallow electron level below the conduction band[70,96]. With this intuition, a systematic investigation of the surface chemistry can be conducted to investigate the presence and role of surface defects in the material. The following discussion will focus on the $CsPbBr_3$ NC cubes, although the methodology should be generalizable and able to be applied to other compositions or shapes.

Currently the proposed methods to mitigate the effects of undercoordinated lead atoms fall in three categories: shifting the dynamic surface equilibrium towards increased surface-bound halide[44,100,102,103], ligand passivation of surface states[97,104], and etching of under-coordinated lead from the NC surface[43,105]. The first two strategies can work well in some circumstances, improving the PLQYs of $CsPbBr_3$ NC ensembles up to nearly 95%[44,97,100,102–104]. However, these strategies also require introducing a significant excess of ligands or bromide sources to shift the dynamic surface equilibrium towards passivation and achieve good results. Moreover, the addition of excess non-conductive species to the colloidal solution is an unappealing prospect for using such treated NCs as building blocks for optoelectronic films. Irrespective, these two strategies ultimately encounter steric or entropic limitations that hinder un-restricted access to the NC surface, making it difficult to fully passivate all surface defects present in a controlled manner. To access $CsPbBr_3$ NCs with the highest optical performance, a different strategy without the same limitations is desirable. A potential chemical strategy that does not encounter the same limitation is selective chemical etching.

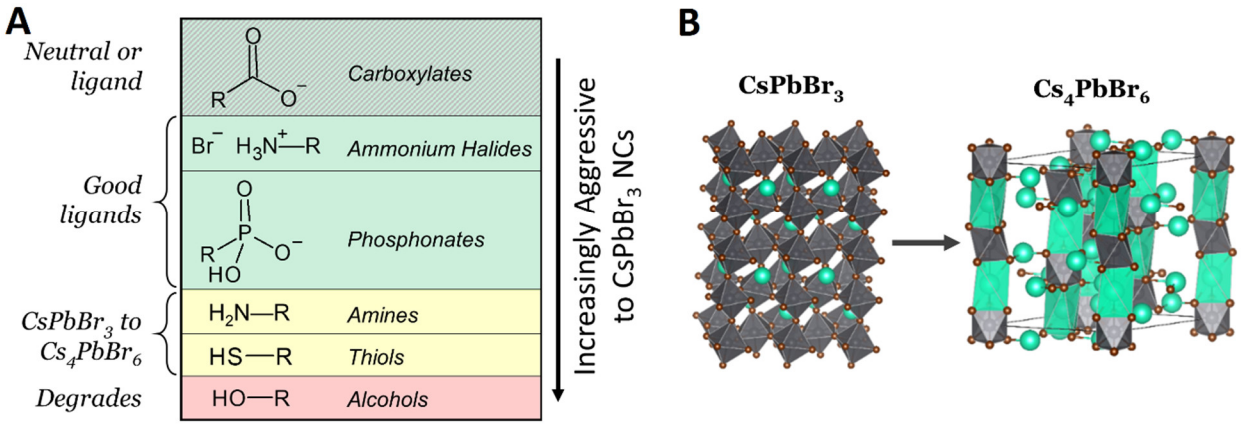

Figure 3.3: Ligand induced transformation of $CsPbBr_3$ nanocrystals. (A) Table that briefly summarizes the classes of ligands that are neutral, beneficial, substantially removes lead converting $CsPbBr_3$ to Cs_4PbBr_6, and substantially

degrades the materials. (B) Change in the crystal structure that arises from substantial removal of lead from the $CsPbBr_3$ and the conversion of the related Cs_4PbBr_6 material system.

Selective chemical etching of semiconductors to tailor the optoelectronic performance is not a new concept, it has been successfully used to carefully control the surface properties of thin film semiconductors and for epitaxial liftoff processing[47,106,107]. The critical parameter that determines the level of success with selective etching is the etchant strength, which needs to be finely tuned to optimize the target etching pathway and avoid problematic side reactions. In principle, atoms within different local bonding environments have different cohesive binding energies, even for subtly different atomic sites within an extended crystal. The difference in the cohesive energy of local atomic environments can be exploited to preferentially target a specific local atomic environment. A chemical method to selectively target optical defects and selectively remove them from the NC while leaving fully-coordinated atoms untouched is a potentially powerful tool that can be used to improve the optical performance of quantum dots. To this end, the relatively weak internal chemical bonding of the lead halide perovskites is advantageous, enabling room temperature etching reactions with mild reagents (Figure 3.3). However, this weak bonding also restricts the available chemical library as the conversion of $CsPbBr_3$ to Cs_4PbBr_6 (Figure 3.3), a related non-perovskite lead depleted-phase material with poor optical performance, has been shown to be possible through the addition of some chemical etchants such as thiols[108]. Although these strong chemical etchants, like thiols, are too strong for the relatively weakly bound $CsPbBr_3$ NCs, removing nearly 75% of the lead present in the NC, they represent an important starting point from which to identify a more appropriate etchant. A softer chemical etchant is more appropriate to exploit the energetic difference in the different $CsPbBr_3$ NC sites to achieve higher degrees of etching selectivity. In principle, the appropriate etching conditions can provide reliable access to $CsPbBr_3$ NCs with near-unity luminescence efficiency by chemically controlling the number of defect sites present on the surface.

3.2: Selective Chemical Etching of $CsPbBr_3$ Nanocrystals

3.2.1: Chemicals Used in the Selective Etching of $CsPbBr_3$ Nanocrystals

Lead bromide ($PbBr_2$, 99.999%, Sigma Aldrich), cesium carbonate (Cs_2CO_3, 99.9%, Sigma Aldrich), octadecene (ODE, 90% tech grade, Sigma Aldrich), oleic acid (OA, 90% tech grade, Sigma Aldrich), oleylamine (OLA, 70% tech grade, Sigma Aldrich), hexanes (mixture of isomers, anhydrous 95%, Sigma Aldrich), toluene (anhydrous 99%, Sigma Aldrich), ethyl acetate (anhydrous 99.8%, Sigma Aldrich), methyl ethyl ketone (99%, Sigma Aldrich), ammonium thiocyanate (NH_4SCN, 99.99%, Sigma Aldrich), sodium thiocyanate (NaSCN, 99.99%, Sigma Aldrich), ammonium bromide (NH_4Br, 99.99%, Sigma Aldrich), lead nitrate ($Pb(NO_3)_2$, 99.0%, Sigma Aldrich), lead thiocyanate ($Pb(SCN)_2$, 99.5%, Sigma Aldrich), guanidinium thiocyanate (GSCN, 99.0%, Sigma Aldrich), didodecyldimethylammonium bromide (DDAB, 98%, Sigma Aldrich), octanedithiol (ODT, >97%, Sigma Aldrich), sodium diethyldithiocarbamate (>99%, Sigma Aldrich), potassium thioacetate (98%, Sigma Aldrich), potassium selenocyanate (>99%, Sigma Aldrich), and tetramethylthiourea (98%, Sigma Aldrich) were purchased and used without further purification.

3.2.2: Thiocyanate Chemical Etching Conditions

The ensembles of $CsPbBr_3$ nanocrystals were prepared following the same synthetic protocols highlighted previously in this dissertation (Chapter 2.2). The surface treatments were conducted on both freshly synthesized and aged samples with results being very consistent for treatments either conducted inside or outside of an argon glovebox. For etching reactions, the thiocyanate salt was dried and degassed, if needed, to ensure that the $CsPbBr_3$ samples were not exposed to additional unnecessary moisture and then was stored in nitrogen dry boxes. This step can be essential considering the highly hydroscopic nature of many thiocyanate salts, particularly the ones that were employed herein. The dry thiocyanate salts were added directly into the nanocrystal sample in excess, although the nanocrystal exposure was limited due to the limited solubility of the ionic salts in the nanocrystal sample solution. Due to the limited solubility some of the thiocyanate salt remains and sinks to the bottom of the nanocrystal sample solution. To ensure the nanocrystals experienced a consistent etching environment, the mixture was stirred at room temperature, with most of the changes to the sample occurring in 20 minutes or less. The remaining salt was removed from the solution by either centrifugation followed by decantation or by using a PTFE syringe filter. The isolated samples were then ready for use in further characterization.

3.2.3: Thiocyanate Chemical Etching Discussion

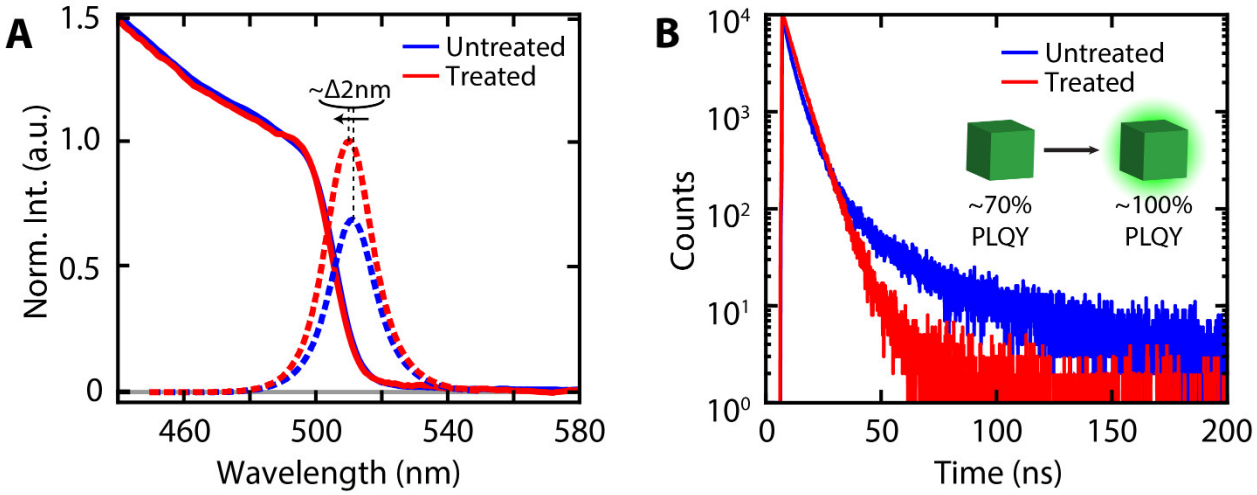

Figure 3.4: Optical properties before and after thiocyanate-based chemical etching. (A) Shown are the absorption (solid lines) and photoluminescence (dotted lines) of a representative as-isolated ligand concentration $CsPbBr_3$ nanocrystal sample dispersed in hexanes before and after thiocyanate etching. The photoluminescence spectra are normalized to the measured quantum yield from the integrating sphere setup. (B) Shown are the time-resolved photoluminescence excited state decays under pulsed 407.1 nm excitation at room temperature for an untreated sample (initially 70±2.5%) and the same sample after thiocyanate etching (afterwards 100±2.5%).

One strategy to get a softer chemical etchant is to employ a sulfur-based chemical etchant that has less electron density present on the sulfur atom. With this strategy in mind, several chemical species were investigated, and it was determined that thiocyanate-containing powders, both ammonium thiocyanate (NH_4SCN) and sodium thiocyanate (NaSCN), could be promising candidate etchants. To conduct the etching reactions, dry thiocyanate salt powder was added

directly into the as-synthesized $CsPbBr_3$ NC solution, a solution of NCs that were isolated and maintained in anhydrous hexanes. The etching of as-synthesized ensembles typical finishes after 30 minutes, although most of the change occurs in the first few minutes. After etching, there is largely no change in the absorption spectrum (Figure 3.4), but a significant change in the NC ensemble PLQY does occur, approaching near-unity efficiencies (from 70±2.5% to 100±2.5%). The observed change in PLQY arises from a reduction in the non-radiative recombination rate ($0.083\pm0.004\ ns^{-1} \rightarrow <0.001\pm0.005\ ns^{-1}$), changing the time-resolved excited state decay dynamics from a multi-exponential trajectory to a single exponential trajectory (Figure 3.4). The observation of multi-exponential excited state decay trajectories is not unique to the $CsPbBr_3$ NCs but is instead a common feature of many quantum dots. The appearance and nature of a multi-exponential decay is difficult to interpret without a well-defined kinetic model that accounts for all present excited state decay pathways, and still the interpretation may still be non-trivial and nuanced. However, from a qualitative view point, a multi-exponential decay suggests that many states with different rates take part in the excited state decay. On the other hand, the appearance of a single-exponential decay trajectory after chemical etching suggests the presence of a single rate-limiting step in the decay process, more reminiscent of a two-level system rather than a multi-level system. The transformation of the excited state decay dynamics suggests that the chemical etching substantially changes energy levels that participate in the NC excited state.

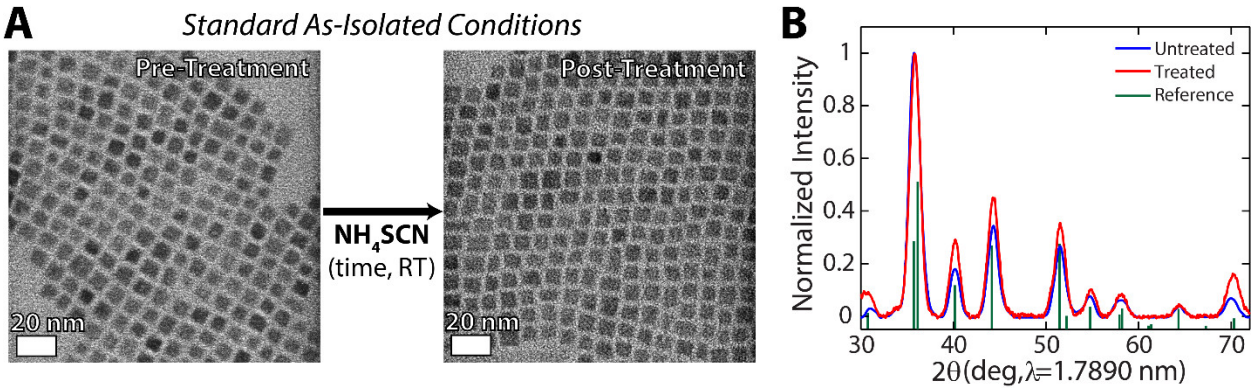

Figure 3.5: Structural characterization of samples before and after thiocyanate etching. (A) Set of representative TEM micrograph images of the $CsPbBr_3$ nanocrystal samples before and after treatment for both fresh and aged samples, in which the scale bar represents 20 nm. (B) X-ray diffraction patterns of the untreated and treated aged nanocrystal samples, with feature positions that overlap, and additionally the Pnma crystal structure reference for the $CsPbBr_3$ nanocrystals showing high agreement.

Although changes in the optical properties of the ensemble were used as a handle to screen potential chemical etchants, it is equally important to ensure that there are no drastic changes to the structure of the NC that are responsible for the non-radiative rate reduction. This structure characterization is critical considering the weak nature of the lead halide perovskites that enables the substantial reported structure changes that emerge when exposed to several other chemical species[108,109]. Unlike those species, both before and after the thiocyanate-based etching, the NC ensemble presents a uniform size distribution and regular cube-like morphology (Figure 3.5). Furthermore, the powder X-ray diffraction pattern peak positions and widths of the NC ensemble remain unchanged as a result of the treatment, with peaks consistent with either the Pm3m or Pnma crystal structure[69,110]. Although there is an on-going debate on the specific crystal structure of the

$CsPbBr_3$ NCs, it is apparent that the material has not changed to a different composition[108,109] (Cs_4PbBr_6, $CsPb_2Br_5$, etc.). Taken all together, there are no substantial changes to the overall inorganic crystal that might convolute the observed improvements, suggesting that the change is likely occurring on just a handful of atoms on the NC surface.

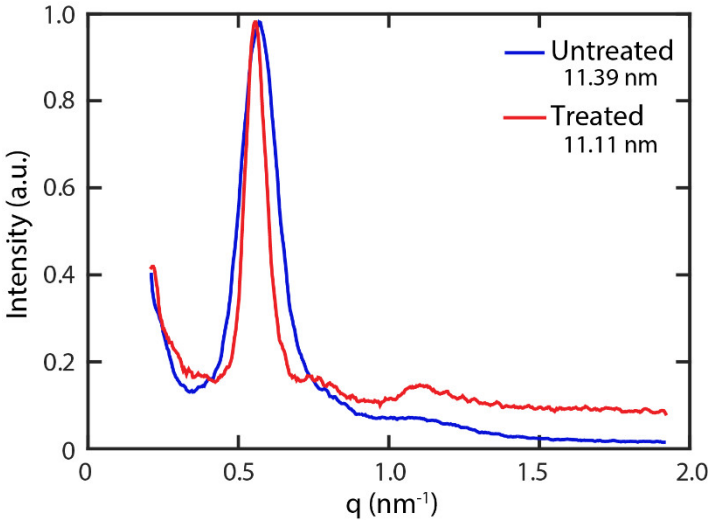

Figure 3.6: Small angle x-ray scattering patterns of $CsPbBr_3$ nanocrystal samples. Shown are the SAXS patterns for the aged $CsPbBr_3$ nanocrystal sample before and after etching with thiocyanate. The periodic spacing of the dried samples before etching was 11.39 nm and after etching was 11.11 nm. The SAXS patterns were taken under vacuum at room temperature in a Bruker NanoStar SAXS instrument equipped with a Cu target.

Additionally, the spacing between neighboring NCs remains unchanged (2.5±0.1 nm → 2.5±0.2 nm), indicating minimal, if any, change to the overall organic ligand shell as a result of etching. The spacing of neighboring NCs by TEM and overall little change to the organic ligand shell of the $CsPbBr_3$ nanocrystal ensemble is then further supported by small-angle X-ray scattering (Figure 3.6) showing that before etching the periodic spacing of a dried film was 11.4 nm and afterwards the treatment was 11.1 nm. This shows that the organic ligand shell surrounding the NCs is also not substantially affected by the etching reaction. Overall from a structural point of view, the etching reaction does not substantially perturb the NC while significantly improving the optical performance, consistent with the notion of a gentle etching reaction.

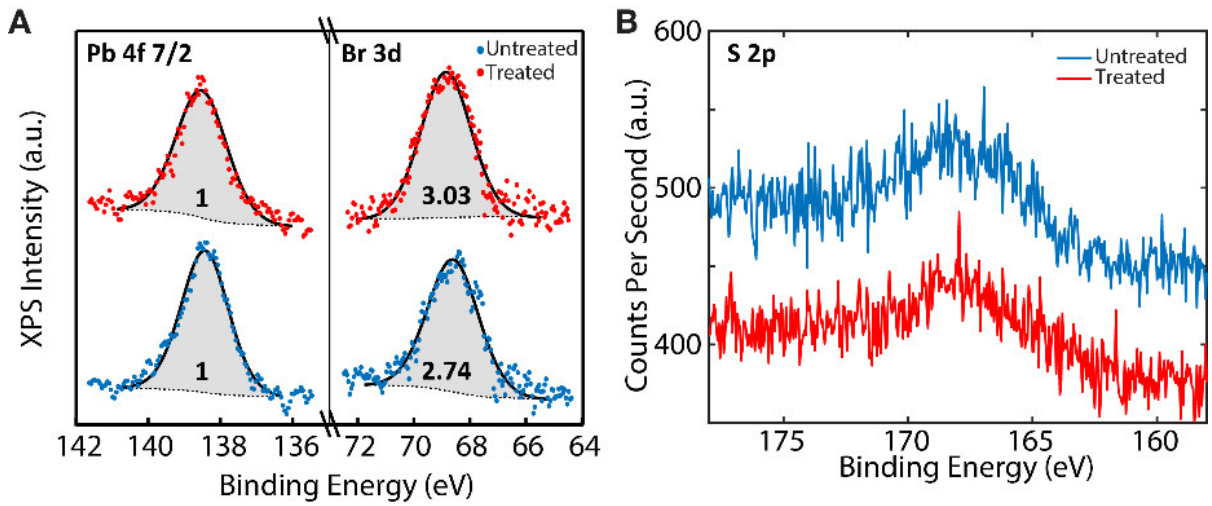

Figure 3.7: X-ray photoelectron spectroscopy composition of the $CsPbBr_3$ nanocrystals. (A) Shown are the XPS spectra of the lead region (Pb 4f 7/2) and bromine region (Br 3d) regions of interest for both the untreated and treated $CsPbBr_3$ nanocrystal samples. Included in the spectra are the elemental ratios present relative to the integrated energy sensitivity corrected lead region. (B) XPS spectra of the sulfur region (S 2p) for both the untreated and treated aged sample of $CsPbBr_3$ nanocrystals. The two spectra are offset for clarity, but there is not a significant difference for the region following thiocyanate etching.

Since the improvements in the optical performance of the material does not arise from the macroscopic scale, understanding how the local atomic environment at the surface of the $CsPbBr_3$ NCs manifests itself on larger scales can be quite informative about the underlying chemical reactions that are occurring. The local surface of the NCs can be effectively probed with X-ray photoelectron spectroscopy (XPS), a measurement technique that can probe the elemental composition within nanometers of the surface. For the $CsPbBr_3$ NCs, focusing on the Pb 4f 7/2 and Br 3d binding energy regions will provide the most direct insight into the etching reactions. Prior to the thiocyanate etching, the aged NC sample presented a Pb:Br ratio of 1:2.7 (Figure 3.7), consistent with a surface with an excess of lead present that has since been observed and appreciated in other investigations[44,111]. Following the etching, we find that the NC sample presents a Pb:Br ratio of 1:3.0 (Figure 3.7), closer to the ideal ratio for the $CsPbBr_3$ perovskites without a lead-rich surface. The observed elemental ratios are highly consistent with a reduction in the number of local undercoordinated lead atoms on the NC surface, a situation that was suggested to be shallow electron levels below the conduction band[70,71,96] and has since been the subject of additional reported investigations[44,105,111]. Consistent with the lack of structural change in the overall NC, the changes in the elemental ratios suggest that there is a change in at most 15% of the surface lead atoms present. The small quantity of surface defect sites can be difficult to observe with other experimental techniques, particularly when the number of under-coordinated lead atoms decrease further. Optical studies however are particularly sensitive to the presence of these electronic defect sites and offers the potential to probe the impact of small numbers of sites. Although a change occurs in the lead binding energy region, there is not an accompanying change in the sulfur region (Figure 3.7), suggesting that the thiocyanate etching fully removes the undercoordinated lead from the surface. The complete removal of a chemical species can be directly probed to grant insight into the etching process itself.

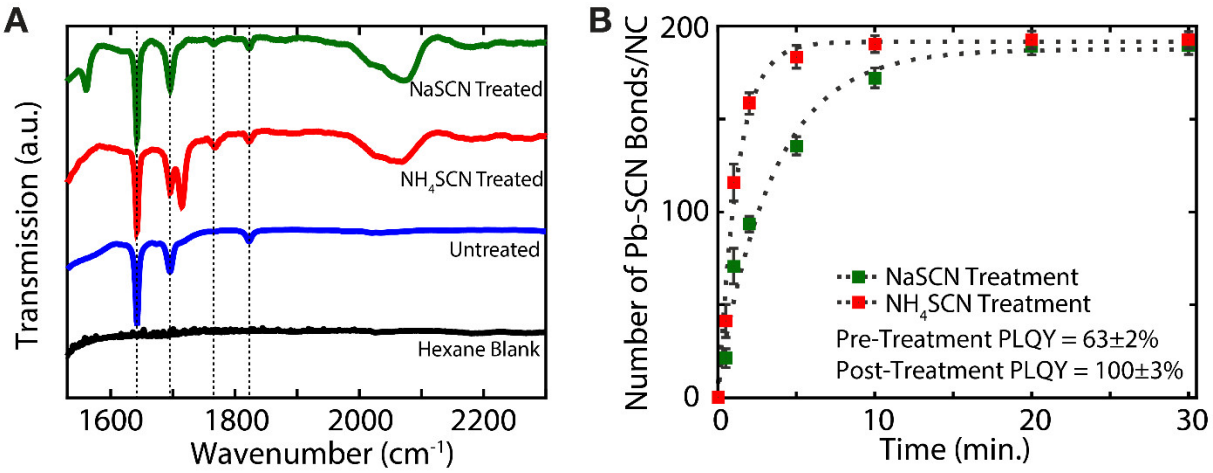

Figure 3.8: Liquid sample cell infrared spectra of the $CsPbBr_3$ samples. (A) Shown are the FTIR transmission spectra using a liquid sample cell within the vacuum environment of a Bruker IFS 66v/S vacuum FTIR. Spectra include the hexanes matrix, untreated $CsPbBr_3$ nanocrystal solution in hexanes, and treated $CsPbBr_3$ nanocrystal solutions in hexanes with NaSCN and NH_4SCN. The IR region of interest for the carbonyl stretches and thiocyanate stretches are highlighted, between 1550 cm^{-1} and 2300 cm^{-1}. (B) Time-dependent change in the number of lead-thiocyanate bonds per nanocrystal determined by focusing on the integrated C≡N stretch centered at 2060 cm^{-1} for both the NaSCN and NH_4SCN treated samples over the course of 30 minutes. Each sample was isolated from the thiocyanate salt source by centrifugation and measured to ensure minimal unintended etching.

An easily accessible and commonly employed technique to study the bonds present in a NC ensemble solution is by using infrared (IR) spectroscopy. Moreover, by employing a liquid cell IR sample holder, the NC ensemble can be studied in its native solution environment within the vacuum of the IR beam path. However, IR signatures that are spectrally separated from other signals are critical to be able to investigate chemistry that is occurring in the native liquid environment. Conveniently, the cyano-stretch has a characteristic IR frequency that is spectrally separated and presents distinct characteristic frequency shifts when bound to different atoms[112]. Following the thiocyanate etching, a relatively broad IR peak appears at 2060 cm^{-1} (Figure 3.8), a position consistent with the bond frequency shift for C≡N when thiocyanate is bound to lead with a Pb-S bond[112]. It is worth noting that the thiocyanate salts are not soluble in pure hexanes, even in boiling hexanes there is no IR peak consistent with thiocyanate observed (Figure 3.8), meaning that these thiocyanate IR signals are related to the thiocyanate species that have interacted with the nanoparticle in some way. Furthermore, while the etching with either NH_4SCN or NaSCN both yield a thiocyanate peak at 2060 cm^{-1}, there are distinct peaks that appear depending on the counter-ion present. Etching with NaSCN results in a peak at 1560 cm^{-1}, attributed to the C=O stretching of sodium oleate (Figure 3.8), while etching with NH_4SCN yields a peak 1712 cm^{-1}, consistent with the C=O stretching of oleic acid. The interaction of the counter-ion (Na, NH_4) with oleate species present in solution while the thiocyanate interacts with lead nanoparticle are important interactions for the etching chemical mechanism that is discussed later. Consistent with other characterization that suggests a limited interaction, the intensity of the C≡N IR peak quickly increases and levels off (Figure 3.8), ultimately only representing a fraction of the number of lead atoms present in each NC. Understanding the origin of the asymptotic behavior will be critical to applying this selective etching to other compositions and geometries. This limiting behavior will also be further explored later in this dissertation.

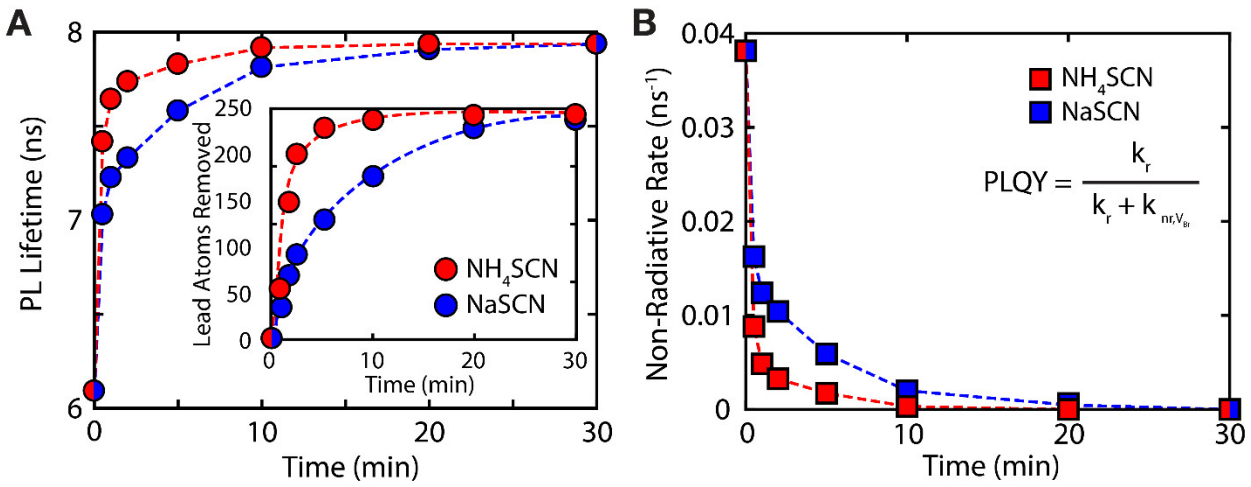

Figure 3.9: Non-radiative contribution per bromine vacancy determination. (A) Combination of photoluminescent excited state lifetime and the number of lead atoms removed from the $CsPbBr_3$ nanocrystal sample throughout the etching reaction. Data is shown for both the NaSCN and NH_4SCN etched nanoparticle samples. (B) The combination of excited state lifetime, number of lead atoms removed, and the photoluminescence quantum yield allows the non-radiative rate to be determined at the isolated time fractions throughout the etching reaction. There is an assumption that the defect sites are independent, i.e. that they linearly contribute to the non-radiative rate, a decent approximation for low density defects. For the linear nature to be consistent, there are more lead atoms removed from the nanocrystals than under-coordinated lead atoms present. The combination of the measurements affords the opportunity to determine the non-radiative contribution of an individual bromine vacancy within the nanocrystal.

With the distinct IR signature for the lead-thiocyanate bonds providing a handle to quantify the number of lead atoms removed, the time-evolution of the reaction can be monitored by measuring a time-series of samples. The combination of quantitative IR spectroscopy, photoluminescence lifetime, and PLQY can be used in conjunction to determine the number of under-coordinated lead atoms present throughout the etching reaction and contribution to the overall non-radiative recombination rate on a per under-coordinated lead atom basis. For the $CsPbBr_3$ NC ensembles, the presence of an under-coordinated lead atom is a direct reporter of the number of bromine vacancies due to the nature of the local atomic environment at those vacancies. This approach can be repeated for both ammonium and sodium thiocyanate (Figure 3.9), particularly informative since those etching reactions proceed at different rates. Under the assumption that the optical defect sites act independently of each other, i.e. they linearly contribute to the overall non-radiative rate ($k_{nr,total} = N_{V_{Br}} k_{nr,V_{Br}}$), the contribution of each site can be determined. In order to capture the change in the PL lifetime with a linear contribution of each bromine vacancy, it becomes apparent that more lead atoms are removed from the NC ensemble than under-coordinated lead atoms present, indicative of an etching reaction that is not fully site-selective, but it is a substantial step towards the right etching strength. By combining these measurements, it was determined that there were nearly 90 bromine vacancies per NC for an ensemble that initially presented a 70±2.5% PLQY with each bromine vacancy contributing 0.0006±0.0003 ns^{-1} to the overall non-radiative rate. The contribution is small relative to the radiative rate, each defect only contributing an amount 200 times smaller than the radiative rate (0.013 ns^{-1}), but the cumulative effect of several vacancies adds together to significantly affect the overall performance of the ensemble. In fact, a single bromine vacancy can reduce the PLQY to

99.5%, close to the highest value that was recently measured for CdSe/CdS colloidal quantum dots thermally[45], an efficiency potentially below the value required for some advanced energy harvesting applications. The presence of a defect state that only contributes a small amount to the overall non-radiative recombination rate is very consistent with the notion of a highly defect tolerant material. For the $CsPbBr_3$ nanoparticles, it is not that there are no defects present; the defects that are present result in small optical losses. However, further investigations into the composition and size-dependent trapping dynamics and cross-sections of individual defects are needed to fully understand the nature of defects in these materials.

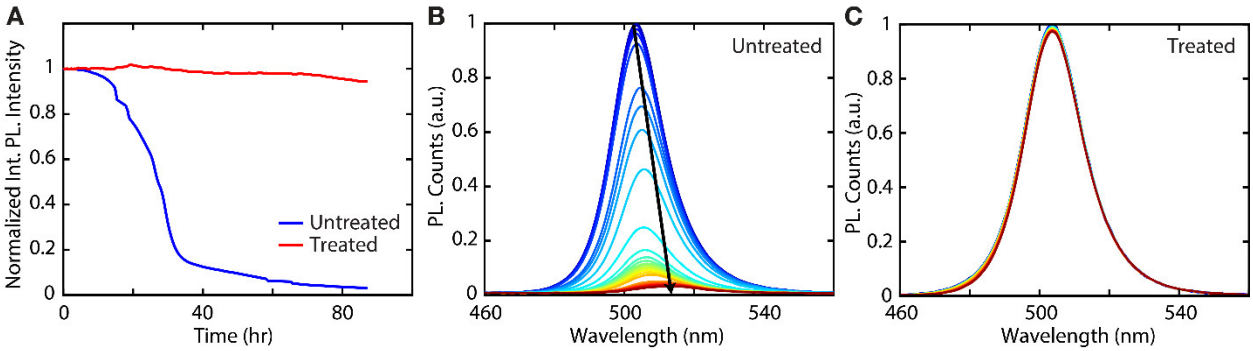

Figure 3.10: Change in the optical stability of the nanocrystal ensemble after etching. (A) Shown are the integrated PL intensity trajectories throughout continuous 365 nm illumination for the treated and untreated $CsPbBr_3$ nanocrystal samples normalized to time zero. Initially the untreated sample presents an 81±2.5% quantum yield and the treated sample presents a 99±2.5% quantum yield. (B) Change in the PL spectrum of the untreated nanocrystal sample with continuous illumination, with the quantum yield decreasing to 10% after ~90 hours of continuous illumination. (C) Change in the PL spectrum of the treated nanocrystal sample with continuous illumination, with the quantum yield decreasing to 88% after ~90 hours of continuous illumination.

When NC semiconductors have surface defect sites, the influence of carrier trapping sites can dramatically change the photo-stability of the NC by presenting a location for photo-induced degradation to occur. For example, the combination of charge carrier trapping sites and access to the external environment has been suggested to be the key player in the degradation of lead halide perovskite photovoltaics[113–115]. By reducing the number of surface defects on the NC through etching, the photo-induced degradation of the material is also expected to substantially slowdown, which is observed (Figure 3.10). The untreated $CsPbBr_3$ nanocrystal sample not only presents a substantial decrease in quantum yield but also presents a distinct red-shift in the PL position, a trend that is not observed for the treated sample (Figure 3.10). The increase in photo-stability following thiocyanate-based chemical etching is substantial. Selective chemical treatments that remove optoelectronic defects might be able to improve the performance of perovskite photovoltaics by reducing interface and grain boundary charge carrier trapping sites.

The ability for a simple thiocyanate salt-based etching reaction to improve the optical performance of $CsPbBr_3$ NCs by reducing the non-radiative recombination rate highlights the importance of surface defects to the overall efficiency of the material. For the as-synthesized conditions, there is little structural change in the NC ensemble with the change in optical performance arising from interacting with a small number of the surface lead atoms. The apparent self-limiting nature of the etching reaction, even when an excess of thiocyanate salt is present in solution is surprising. To understand the origin of this limiting nature and how to further modulate

the selectivity of the etching reaction, a deeper investigation into the mechanism is needed. Fully understanding the etching reaction will likely allow the selective etching reaction to be robustly extended to other shapes and compositions.

3.3: Mechanism of Chemical Etching in $CsPbBr_3$ Nanocrystals

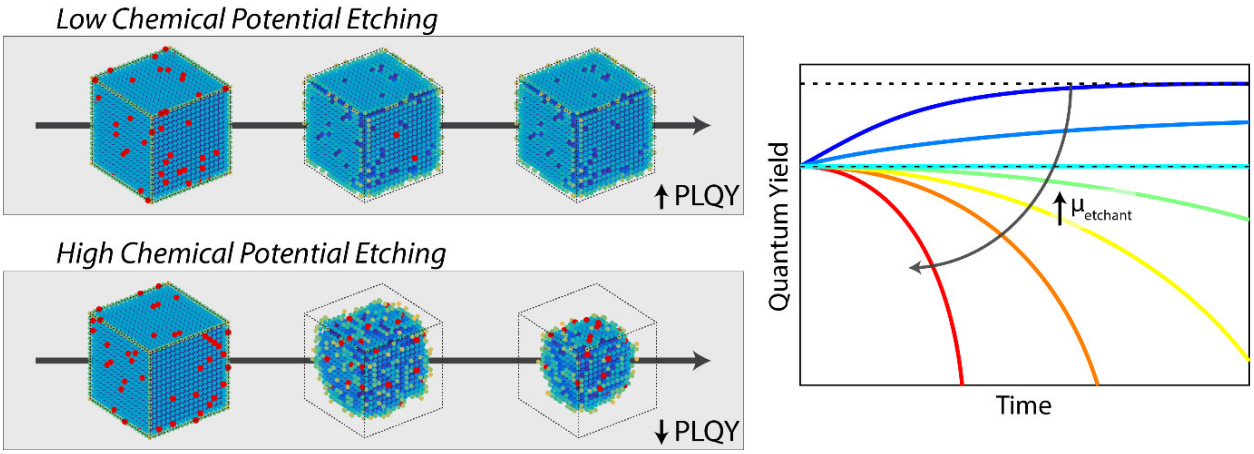

Figure 3.11: Schematic depiction of the different etchant chemical potential regimes. Shown are the results of a model of the etching reaction (left) that reproduces the experimental results (right). The model changes the relative probability of removing different lead atoms as the etchant chemical potential is changed, with the under-coordinated lead atoms being significantly easier to remove under normal etching conditions.

The conditions of the as-synthesized $CsPbBr_3$ NCs appear to allow the thiocyanate etchant to interact with a limited number of surface sites in the material. However, the etching reaction is not driven exclusively by energetic differences between differently coordinated sites since both under-coordinated and fully-coordinated lead atoms are removed during the etching reaction (Figure 3.11). Given the weak nature of bonding in these materials, it is likely that there are a few necessary chemical equilibria and subtle differences in etching kinetics that are responsible for the etching selectivity. In this interpretation, atoms that are slightly less strongly bound to the crystal because they have fewer bonds are removed at a faster rate, whereas fully coordinated atoms are removed at a slower rate. The interpretation of the etching reaction in these terms is analogous to other selective chemical etching reactions[116–119], in which the coordination of the atom to be etched determines the rate that the atom is removed from the nanocrystal and the etchant chemical potential effectively tunes the relative rates for differently coordinated atoms. Fully understanding the mechanism of etching is essential to improve control over the etching reaction and expand this approach to other shapes and compositions.

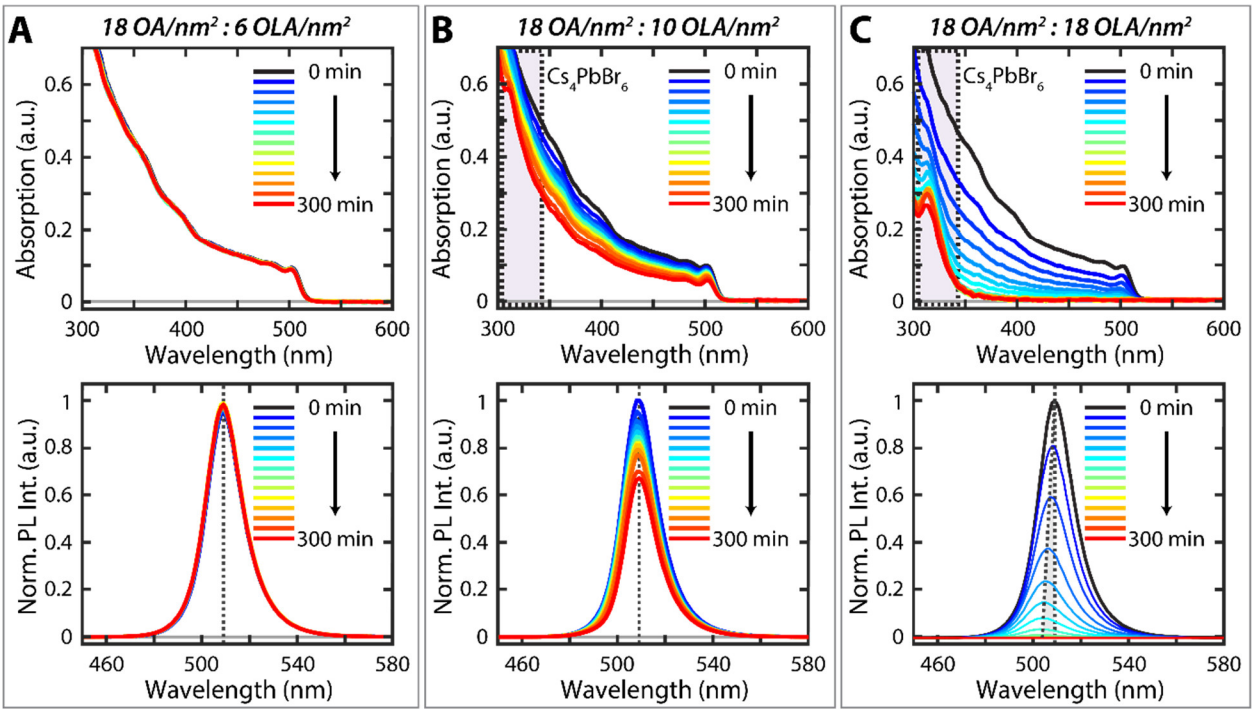

Figure 3.12: Evolution of the absorption and PL spectrum throughout thiocyanate etching. Shown is the time evolution of the absorption and PL spectrum for a $CsPbBr_3$ nanocrystal sample with (A) 18 oleic acid and 6 oleylamine ligands per square nanometer of nanocrystal surface area, (B) 18 oleic acid and 10 oleylamine ligands nm^{-2}, and (C) 18 oleic acid and 18 oleylamine ligands nm^{-2}. The two spectroscopic regions of interest are centered at 313 nm and around 505 nm, for the lead-depleted phase material Cs_4PbBr_6 and the $CsPbBr_3$ phase material respectively. The dashed line in the PL spectra are guides to the eye, showing the PL center position at time zero and the blue-shift of the spectrum throughout the etching reaction.

Long-chain hydrocarbon ligands not only play an important role in maintaining the colloidal properties of the NC ensembles, but also drive many post-synthetic transformations through relatively strong ligand interactions. Therefore, understanding the role that ligands play in dictating the outcome of reactions is often critically important to understanding colloidal nanoscale properties. For the $CsPbBr_3$ NCs, there are two ligands present in solution during the etching, oleic acid and oleylamine, and both play important roles in colloidal synthesis of the NC ensemble. Although there is an ideal packing density of ligands on the NC surface[44,100] (~2.9 nm^2), after the synthesis there are more ligands present in solution (~12 nm^2) than required to fully passivate the surface in the as-synthesized sample used for the typical etching experiments (Figure 3.12). At typical ligand concentrations used for the etching reactions, the addition of extra oleic acid or oleylamine does not increase the observed extent of etching compared to the as-isolated conditions. However, the coincidence of both ligands results in substantial changes in the observed etching trajectories (Figure 3.12). Instead of maintaining an essentially unchanged absorption spectrum as seen for the as-synthesized conditions, there are systematically larger decreases in the number of $CsPbBr_3$ NCs present as the concentration of ligands present increases (Figure 3.12). For the larger ligand concentrations (Figure 3.12), an absorption feature near 313 nm appears consistent with the lead-depleted phase (Figure 3.12), Cs_4PbBr_6, showing that the thiocyanate-based etching is also capable of removing large percentages of the lead present in the NCs, although on a longer timescale than other aggressive etchants such as thiols[108]. The conversion to the lead-depleted

phase has also been shown to be possible by increasing the ligand concentration[109], however, at the ligand concentrations that are being employed no etching is observed without introducing thiocyanate. This suggests that the concentration of oleate-oleylammonium ion pairs present in the solution have an important role in dictating the outcome of the etching reaction.

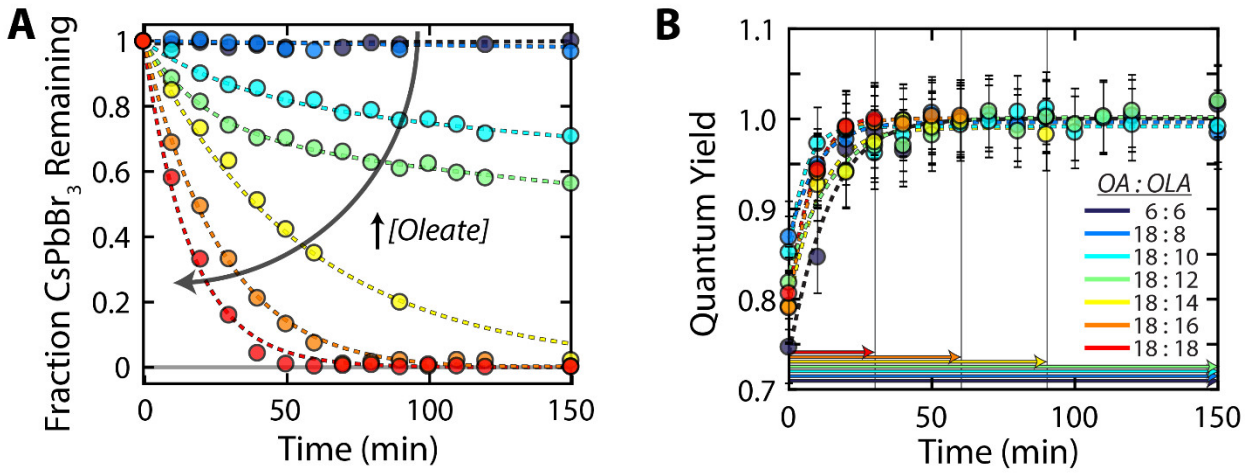

Figure 3.13: Etchant chemical potential dependent ensemble optical properties. (A) Shown is the fraction of $CsPbBr_3$ phase material remaining throughout the etching reaction measured away from the band edge at 425 nm to avoid quantum confinement effects at the band edge. Each of the etching reactions were conducted at varying oleylammonium-oleate ion pair concentrations present in solution, with the arrow showing increasing concentration for clarity. (B) Time-evolution of the ensemble quantum yield throughout the etching reaction at different etchant chemical potentials. Arrows and vertical lines represent the time in which the ensemble absorption became too low to accurately measure the quantum yield. The relative concentrations of oleic acid and oleylamine for both (A) and (B) are shown in the legend of (B).

The overall extent of the thiocyanate-based etching can be broadly tuned by changing the ligand conditions. The as-synthesized concentrations (6 Oleic Acid: 6 Oleylamine per nm^2, Figure 3.13) results in only 3% of the lead etched per nanocrystal, whereas higher ligand concentrations (18 Oleic Acid: 18 Oleylamine per nm^2, Figure 3.13) results in the entire $CsPbBr_3$ ensemble converting to the lead-depleted phase after only one hour by removing nearly 75% of the lead from each nanocrystal. However, while the extent and rate of etching can be finely varied by modulating the oleate-oleylammonium ion pair concentration, the ensemble is still capable of reaching near-unity PLQYs (Figure 3.13) through chemical etching, showing that some degree of etching selectivity is maintained in the region of etchant concentrations in Figure 3.13. The ability to tune the extent of etching arises from tuning the thiocyanate etchant chemical potential that the $CsPbBr_3$ NCs are exposed to, accomplished by changing the number of thiocyanate species present in solution at any given time.

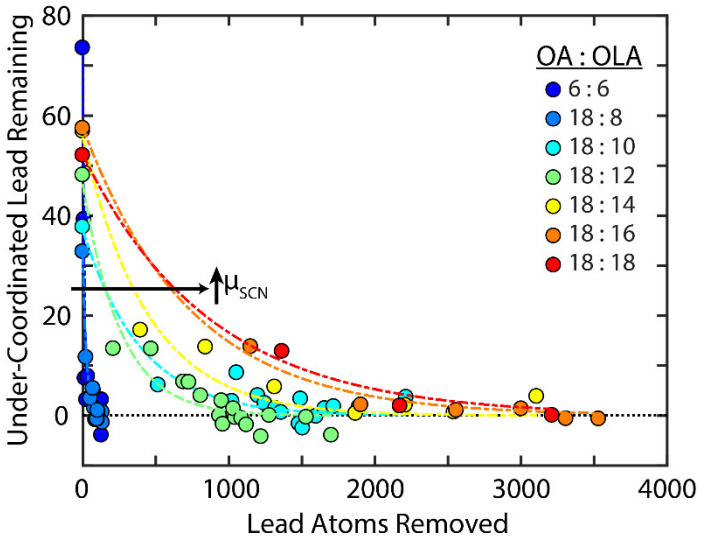

Figure 3.14: Number of under-coordinated lead atoms left throughout the etching reaction. Shown is the number of under-coordinated lead atoms removed relative to the total number of lead atoms removed from the nanocrystal ensemble while increasing the etchant chemical potential by varying the ligand ion-pair concentration.

Although there is some etching selectivity maintained while tuning the etchant chemical potential in the range presented in Figure 3.13, the degree of selectivity is dramatically reduced. The reduction in selectivity requires more lead to be removed overall from the NC ensemble before reducing the number of deleterious under-coordinated lead atoms present and improving the ensemble PLQY (Figure 3.14). This effect is most apparent in the highest chemical potential from (Figure 3.13), in which the ensemble is just able to reach near-unity PLQY before the ensemble fully converts to the lead-depleted material. This shows the importance of controlling the etchant chemical potential to maximize the number of under-coordinated lead atoms that are removed while simultaneously minimizing the number of fully-coordinated lead atoms that are removed to achieve the most selective etching results.

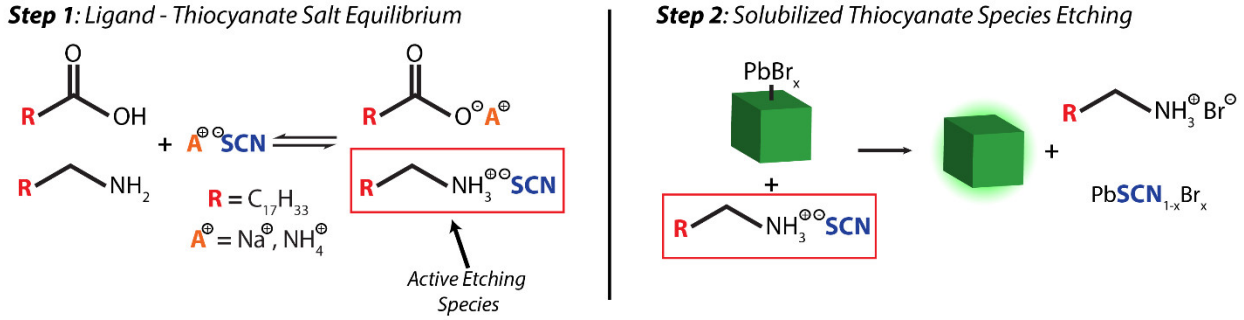

Figure 3.15: Schematic depiction of the necessary chemical equilibria. Shown is the proposed chemical equilibria necessary for the etching reaction to progress based on the different ligand concentrations employed. The first step is the creation of the active etching species, an oleylammonium solubilized thiocyanate ion. Without this step no etching is observed because the thiocyanate is not able to access the nanocrystal surface. Once the active etching species is created, the solubilized thiocyanate species can interact with the surface and remove a undercoordinated lead atom.

Despite some previous notions, the thiocyanate etchants do not possess a conveniently tuned binding strength to lead that enables selective etching, however, the observed selective nature of

the etching reaction arises from carefully controlling the etchant chemical potential. This tuned chemical potential is critically controlled by the concentration of thiocyanate etchant present in solution, dictated by the equilibrium between the ionic thiocyanate salts and the oleate-oleylammonium ion pairs present in solution (Figure 3.15). This equilibrium is apparent considering the emergence of characteristic IR signatures of these solubilized species (Figure 3.15), with different signatures depending on the thiocyanate counter-ion. Once the thiocyanate is solubilized, these species can then diffuse to the NC surface and remove lead (Figure 3.15). At modest chemical potentials (Figure 3.15), the under-coordinated lead present on the NC surface is removed at a faster rate than fully coordinated lead atoms, ultimately improving the ensemble PLQY[43,105] as the quantity of surface defects decreases. It should be noted that while the as-synthesized NC ensemble contains 6 Oleic Acid: 6 Oleylamine per nm^2 from quantitative NMR, based on the observed extent of etching only a fraction (~5%) are available as oleate-oleylammonium ions pairs while the remaining ligands are likely already surface ligands or coordinated with ions left over from the synthesis. The limitation of available oleate-oleylammonium ion pairs puts an upper bound on the achievable PLQY following etching at any ligand concentration, explaining while some samples can only achieve modest improvements. However, introducing an appropriate concentration of ligands into solution increases the etchant concentration and therefore the chemical potential in a controlled manner allowing for precise control of the etching reaction, removing just enough lead atoms to reliably reach near-unity PLQYs without etching too many atoms from the NC.

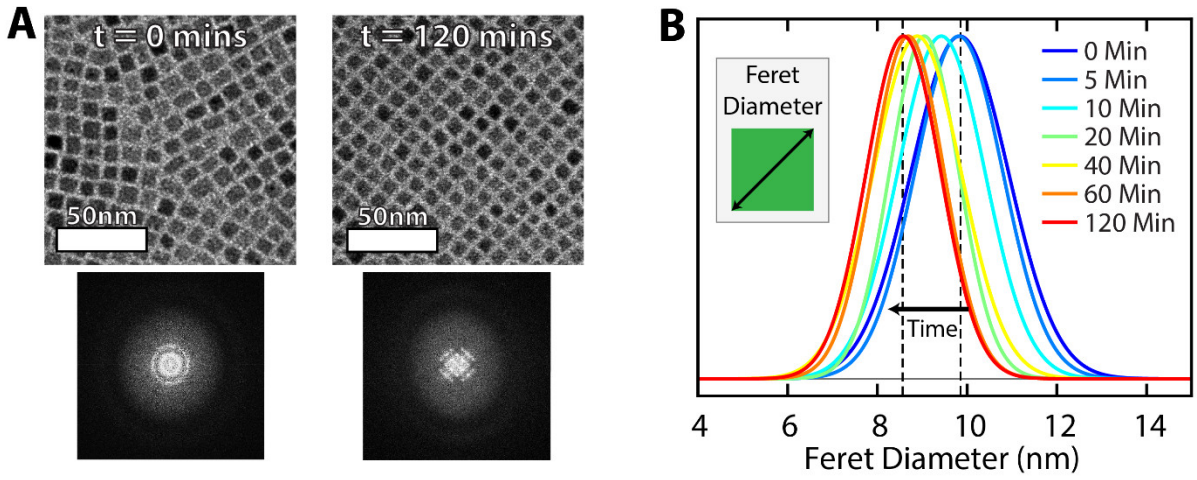

Figure 3.16: Nanocrystal structure throughout the thiocyanate etching reaction. (A) Shown are the TEM micrographs of the $CsPbBr_3$ nanocrystal cube sample showing the change in morphology following thiocyanate treatment (at t = 0 minutes and t = 120 minutes) with 18 oleic acid and 16 oleylamine ligands nm^{-2}. Also shown are the FFT of the TEM images highlighting the change in the sample uniformity following etching. (B) Time-evolution of the $CsPbBr_3$ ensemble feret diameter throughout the etching reaction, with the nanocrystal size becoming smaller with time.

Although the underlying chemical reactions dictate the extent and rate of lead removal, they are not enough to describe where spatially within the NC the lead is removed during the etching reaction. The location of lead removal starts to describe how the ensemble evolves throughout the etching reaction. At modest thiocyanate etchant chemical potentials, the $CsPbBr_3$ NCs become significantly more uniform throughout the etching reaction (Figure 3.16), presenting a more

consistent and regular cube-like morphology. In addition to a change in the NC uniformity, throughout the etching reaction at modest conditions the average feret diameter of the ensemble systematically decreases, by around 15%, and the distribution narrows (Figure 3.16). These are both specific advantages of this controlled etching method in addition to the improvement in PLQY and optical performance.

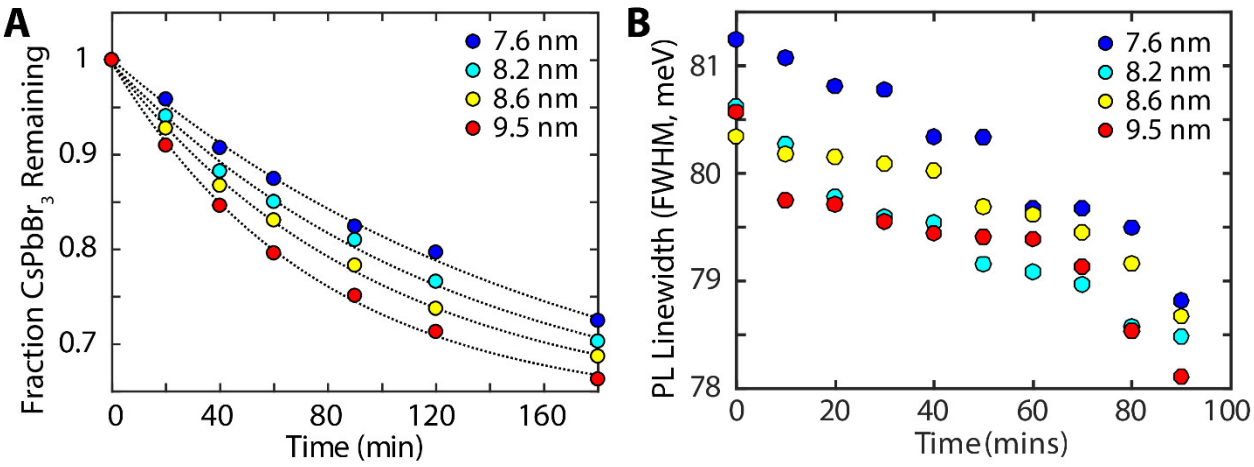

Figure 3.17: Size-dependent etching trajectories of the $CsPbBr_3$ ensembles. (A) Shown is the size-dependent etching of $CsPbBr_3$ nanocrystal cubes for an ensemble with a 7.6 nm, 8.2 nm, 8.6 nm, and 9.5 nm average ensemble size. Each of the etching reactions were conducted at the same ligand ion-pair concentration. (B) Change in the photoluminescence linewidth as a result of the size-dependent etching rate, subtlety narrowing over time and approaching closer to the single-particle PL linewidth.

The systematic decrease in size that results from the etching reaction is responsible for the blue-shifted bandgap observed in etched particles (Figure 3.12), particularly telling for the as-synthesized NC ensembles in which the blue-shift is distinct but the change in NC size is subtle (Figure 3.16). These observations add a valuable insight for similar $CsPbBr_3$ treatments in the literature[43,44,105,108] which observe bandgap blue-shifts ranging from 1 nm to 5 nm but offer varying interpretations of the origin of the shift. Although the influence of ligands coupling to the electronic states of the NC cannot be conclusively ruled out, a decrease in the NC ensemble size distribution offers a simple explanation for the observed blue-shifts. Irrespective, the systematic narrowing of the PL linewidth (Figure 3.17) arises from a size-dependent etching rate (Figure 3.17). In the etching reaction, larger NCs etch at a faster rate than smaller NCs when exposed to the same conditions normalized for the different NC sizes (Figure 3.17), ultimately causing the PL linewidth to narrow subtly as the ensemble becomes more uniform. The origin of the size dependent nature is not obvious and will require further investigation to really understand the influence that it has on the overall etching reactions.

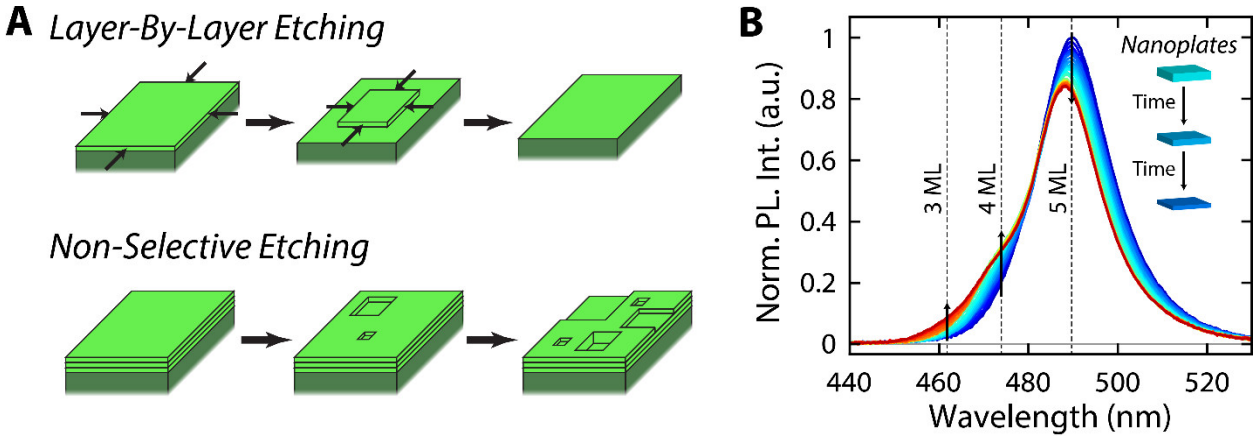

Figure 3.18: Layer-by-layer based etching mechanism. (A) Schematic depiction of the layer-by-layer etching trajectory versus a non-selective random etching trajectory. (B) Evolution of the photoluminescence spectra of $CsPbBr_3$ nanoplates throughout the thiocyanate etching reaction, beginning with a characteristic 488 nm component characteristic of 5 monolayer $CsPbBr_3$ nanoplates and proceeding with the sequential growth of both a 477 nm and 462 nm photoluminescence peak characteristic of the 4 monolayer and 3 monolayer $CsPbBr_3$ nanoplates respectively.

The change in nanocrystal shape uniformity and commensurate increase in PLQY from the thiocyanate-based etching reaction suggests that instead of lead being randomly removed, lead is removed by sequential layers of material (Figure 3.18). At modest etchant chemical potentials, under-coordinated lead atoms are etched more quickly on average than fully-coordinated lead atoms, but fully-coordinated lead atoms are still removed (Figure 3.14). An etching mechanism with a sequential nature would be consistent with a layer-by-layer etching mechanism in which layers that are already partially etched etch at a faster rate than removing material from the next complete layer below the partial layer[116–119]. Conveniently, this microscopic etching mechanism can be put to test with the quasi-2D $CsPbBr_3$ nanoplates (Figure 3.18).

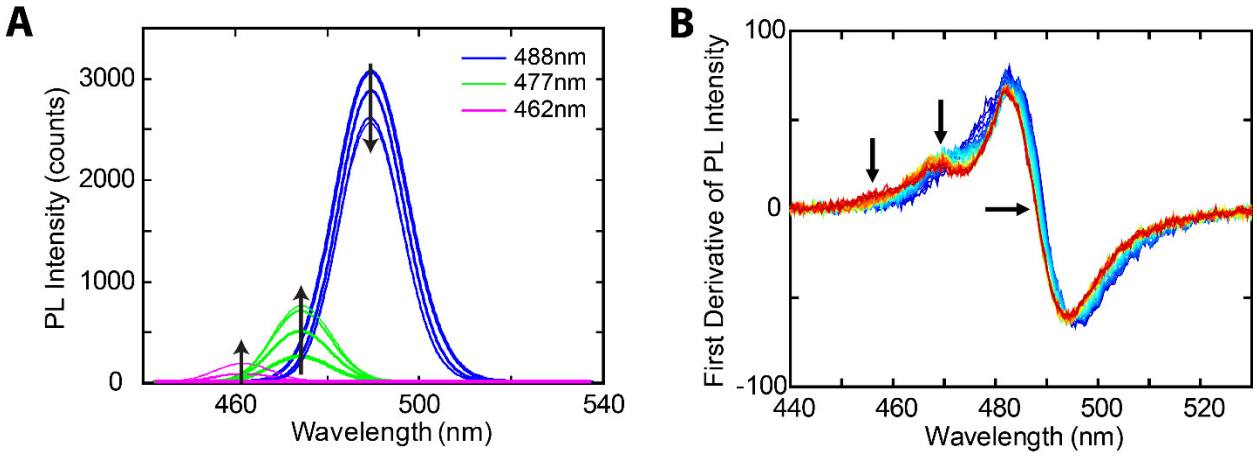

Figure 3.19: Time-dependent evolution of the $CsPbBr_3$ nanoplate ensemble during etching. (A) Shown are the PL components of the etching $CsPbBr_3$ nanoplate ensemble highlighting the emergence of a peak centered at 477 nm and 462 nm. (B) The emergence of the photoluminescence peaks throughout the $CsPbBr_3$ etching reaction highlighted in the first derivative of the PL spectra with time.

Nanoplates offers convenient optical signatures with distinct PL bandgap energies that act as direct reporters of the real-time nanoplate thickness[79] (488, 477, 462, 435, and 405 nm for the 5-,

4-, 3-, 2-, and 1-monolayer thickness nanoplates respectively). Beginning with a 5-monolayer $CsPbBr_3$ nanoplate sample (Figure 3.19), there is a systematic decrease in the 5-monolayer intensity while subsequently observing a 477 nm (4-monolayer thick sub-population) feature and then later a 462 nm (3-monolayer thick sub-population) feature appear in the PL spectra of the ensemble (Figure 3.19). The sequential appearance of the thinner nanoplate subpopulations as the thicker nanoplates etch is highly consistent with a layer-by-layer etching mechanism. This suggests that the underlying mechanism of etching $CsPbBr_3$ under modest chemical potentials through a punctured layer-by-layer mechanism, consistent with the observed outstanding optical performance. A more detailed investigation into layer-by-layer etching trajectories will likely be very informative on the energetic differences between subsequent layers of $CsPbBr_3$. It should be noted that there are currently limitations on the extent of etching with $CsPbBr_3$ nanoplates, as the nanoplates quickly aggregate substantially changing the density of states to more bulk-like instead of the quasi-2D density of states when exposed to excessive etchant chemical potentials.

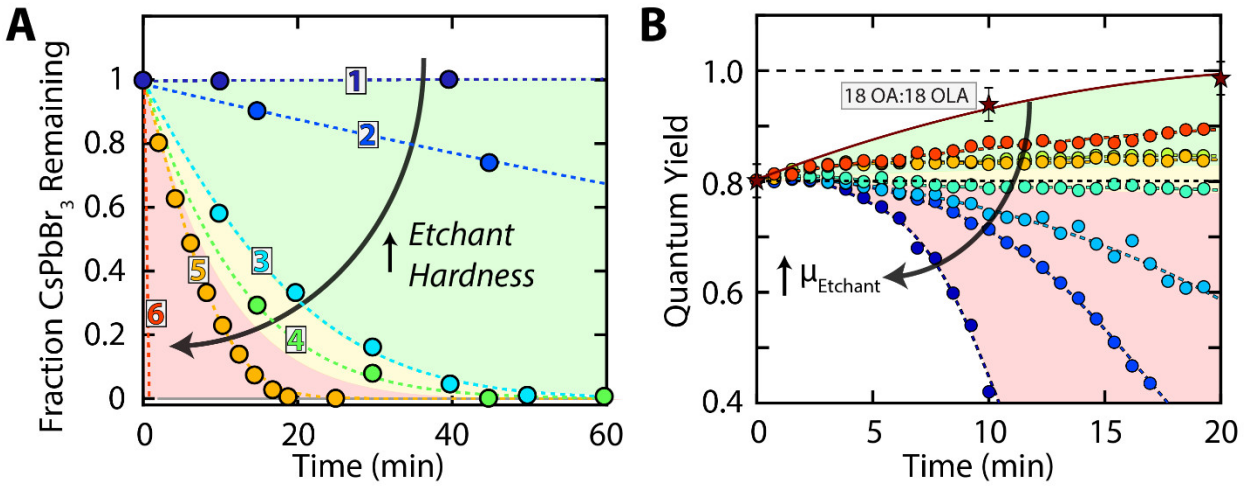

Figure 3.20: Chemical potential-dependent $CsPbBr_3$ nanocrystal cube etching regimes. (A) Change in the etching rate of $CsPbBr_3$ nanocrystal cubes by changing the hardness of the chemical etchant introduced, with each introduced at the same concentration and ligand ion-pair concentration of 18 oleic acid and 18 oleylamine ligands nm^{-2}. Shown are 1. Tetramethylthiourea, 2. Potassium Selenocyanate, 3. Ammonium Thiocyanate, 4. Potassium Thioacetate, 5. Sodium Diethyldithiocarbamate, 6. Octanedithiol. (B) Progression of the quantum yield throughout the thiocyanate-based chemical etching at different chemical potentials, showing the transition from beneficial to neutral to detrimental with increasing chemical potential.

Although the exploration of the selective etching of $CsPbBr_3$ NCs has so far focused on the underlying mechanism of thiocyanate-based etching, the selectivity does not arise from unique properties of thiocyanate as an etchant. The critical factor is the etchant chemical potential which can be more generally attained with other chemical etchants by concurrently tuning the etchant concentration and the strength of the etchant-etched atom interaction. The strength of the lead-etchant bond is determined by the electron density present on the atom that binds to lead, changing the hardness of the etchant[120]. By varying etchant hardness, with tetramethylthiourea being the softest etchant tested and octanedithiol being the hardest, the rate and extent of chemical etching changes dramatically while under nearly equal concentrations (Figure 3.20). Based on these trials, three general regions of etchant chemical potential can be identified: improvement of the PLQY

(green shading), modest if any change in PLQY (yellow shading), and deterioration of the PLQY (red shading). Consistent with this designation, by further increasing the thiocyanate etchant concentration beyond that presented in (Figure 3.20) there is a gradual but distinct transition from beneficial to neutral to detrimental (Figure 3.20). While at first the etching reaction only becomes slightly less selective, only slightly increasing the number of lead atoms that need to be removed from the NC before reducing the number of under-coordinated lead atoms present (Figure 3.20), at even higher etchant chemical potentials the etching transitions to a non-selective and detrimental region (Figure 3.20). Within this non-selective region, lead atoms are removed from the NC without regard for their local chemical environment. This transition is analogous to the roughening transitions observed for other systems[116–119]. While there might be advantages to operating in high etchant chemical potential regimes, such as a wider chemical etchant library and shorter reaction times, there are substantial tradeoffs in etching selectivity and the achievable optical efficiencies. To ensure the optimal etching outcome, a careful balance of the etchant strength and the energetics of different sites within the NC is necessary.

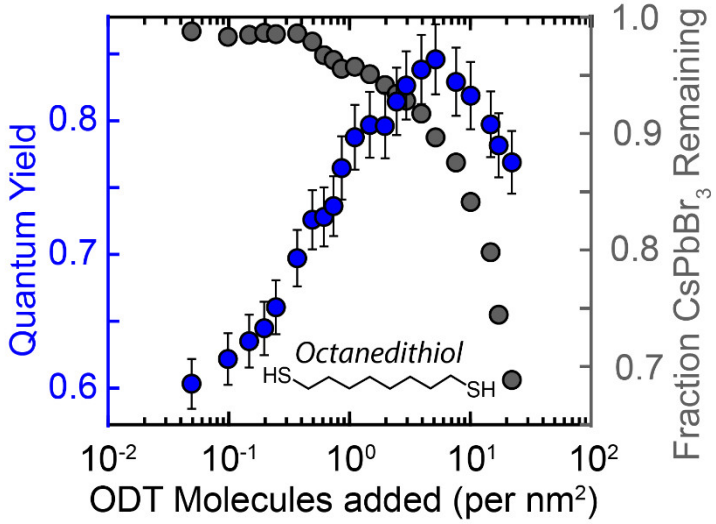

Figure 3.21: Slow-addition of octanedithiol into a $CsPbBr_3$ nanocrystal solution. Shown is the change in the $CsPbBr_3$ ensemble quantum yield by slowly introducing octanedithiol (ODT) into solution, a hard-chemical etchant for lead in the $CsPbBr_3$ nanocrystals. Aliquots were isolated after chemical etching finished for each slow injection.

Knowing that the mechanism of etching critically relies on controlling the etchant chemical potential to achieve good results, hard chemical etchants like octanedithiol can be revisited to recheck for their applicability. For strong chemical etchants, the etchant chemical potential can be kept as low as possible by carefully controlling the concentration of etchant present in solution. This is possible by slowly introducing a hard-chemical etchant like thiol into solution, representing perhaps the best-case scenario for introducing hard-chemical etchants at room-temperature. Instead of observing a rapid degradation of the optical properties of the $CsPbBr_3$ NC ensemble, by slowly adding octanedithiol the PLQY of the ensemble improves from 60±3% to nearly 85±3% (Figure 3.21). Although this does represent a step in the right direction and expands the library of usable chemical etchants slightly, achieving near-unity PLQYs with excessively hard chemical etchants is either more difficult or in some cases intractable as the etchant chemical potential is still too high even as low concentrations (Figure 3.21). Ultimately, this highlights the distinct

change in thought required to post-process these weakly bound lead halide materials. Many of the post-synthetic chemical strategies that have proved to be useful to manipulate the metal chalcogenide materials[108,121,122] are partially, if not totally, incompatible with obtaining lead halide perovskites with the best possible material quality. Therefore, while the ideas might be analogous, a new set of chemical manipulations that critically optimize chemical strengths versus the cohesive energy of the crystallite are essential to avoid undesirable outcomes and side reactions. This optimization will likely represent an on-going theme with lead halide perovskite NC post-processing going forward.

By optimizing the process engineering steps, the power-conversion efficiency of perovskite-based photovoltaics has rapidly increased beyond 22%, however they are still far from their full potential. While these materials show a high defect tolerance, the solution processed methods used to create these films also introduces a relatively large number of defects and the direct optoelectronic consequences of these defects need to be systematically addressed to continue improving the performance of devices. At the nanoscale, a similar set of challenges are being overcame and the lessons learned can help inform rational methods to improve the performance of perovskite thin-film photovoltaics. Substantial challenges are still present with the lead halide perovskites – poor photo-stability, poor chemical stability, low melting point, and facile formation of defects – but they represent a rich platform to perform post-synthetic modifications under mild and tunable conditions at room temperature. By more completely understanding the underlying mechanism of selective chemical etching in the $CsPbBr_3$ NCs, design rules have been developed to improve the etching selectivity and suggest routes to apply this approach to other compositions and shapes. Only by selecting etchants with the correct chemical potential, tunable by both concentration and binding-strength, can the performance of $CsPbBr_3$ NCs be reliably improved to near-unity. The development of rational synthetic methods to access materials near their radiative limit will enable future studies into promising optoelectronic applications operating at their upper efficiency limit.

3.4: Future Directions

The etchant chemical potential is a critical parameter that determines the number of lead atoms that are removed from the $CsPbBr_3$ nanocrystals. An optimization of the chemical potential could allow this strategy to be extended to other material compositions or shapes. Additionally, the nature of the selective chemical etching affords a convenient glimpse into the optoelectronic influence of individual defects in these materials and this insight can help inform the further optimization of these nanocrystalline materials. The ability to reliably access photo-stable and high efficiency luminophores can improve the performance of several optoelectronic applications, a promising application for this work. The selective etching approach can likely be further extended to polycrystalline thin films to help mitigate problematic sites that occurs at grain boundaries or interfaces in the thin films, potentially robustly improving the performance of perovskite based optoelectronic devices.

Chapter 4 - Near-Unity CdSe/CdS Core/Shell Quantum Dots

The following discussion is adapted from Hanifi, D.A., Bronstein, N.D.*, Koscher, B.A.*, Nett, Z., Swabeck, J.K., Takano K., Schwartzberg, A.M., Maserati, L., Vandewal, K., van de Burgt, Y., Salleo, A., Alivisatos, A.P., Redefining near-unity luminescence in quantum dots with photothermal threshold quantum yield, Science,* ***2019****, 363, 1199-1202. Synthesis methodology discovered by Kaori Takano (Tokyo Institute of Technology) to be further described in a PhD thesis in preparation.*

4.1: High-Efficiency Luminescent Quantum Dots

There has been a significant research effort to explore materials with high optical luminescence efficiency. The highest efficiency epitaxial-deposited thin films[47] and rare-earth doped glasses[46] has been 99.5% and 99.7%, respectively. There are molecular systems that have been shown to have PLQYs in excess of 95% when the molecules have optimized structures and within the correct local optical environment[123–125]. On the other hand, due to a large surface area and the potential for many surface states, the efficiencies of quantum dot-based luminophores are typically reported as being lower that high efficiency bulk materials and comparable to their molecular counterparts. However, nanocrystals have many important advantages over their bulk counterparts, including low-cost, easy selective placement, scalable processing conditions, and a widely tunable band gap. Additionally, since the excited state can be distributed over the entire nanocrystal instead of just a handful of atoms such as in molecules, nanocrystals present increased photo-stability and reduced photoluminescence blinking, as well as broad absorption and narrower emissions, compared to molecules. Given their potential advantages, quantum dots represent promising material systems to combine the scalable large-area processing and synthesis of molecules with the photo-stability and efficiencies achieved with well-passivated bulk materials.

At this point there are several open fundamental questions that will probe the impact of individual structural defects and electronic trapping sites on the overall optical performance of the material system[43,44,126–128]. The fundamental investigations into these materials can help to create a set of design rules to understand and optimize new material systems. Additionally, there are many commercial applications that rely on absorbing and then reemitting light, an important feature for the commercialization of luminophores that are being developed in tandem with increases in luminophore PLQY. The achievable efficiencies of established commercial applications like bio-imaging[42,129,130], solid-state lighting[131,132], and color displays[133,134] critically depend on the PLQY of the luminophore that is employed, changing how competitive the technology is with alternatives. Beyond the already commercialized there are several applications that become possible or experience divergent performance as the efficiency of the employed luminophore continues to approach closer to near-unity, including things like optical refrigeration[135,136], thermophotovoltaic engines[137,138], and energy storage within optical cavities[139,140]. These applications draw inspiration from classic thermodynamic cycles but instead of employing fluids as the working medium they use photons. There are many challenges left ahead as explorations of photon-based thermodynamic cycles continue. One large challenge is the development of highly efficient luminophores and the characterization of those materials, as the

reported efficiencies are currently insufficient to start to see the theorized behavior of these applications.

4.2: Luminescent Concentrator Fundamentals

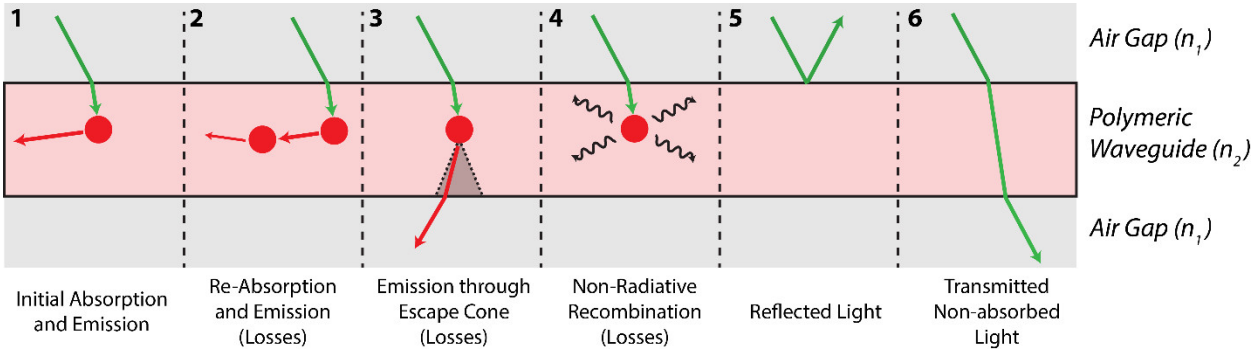

Figure 4.1: Schematic depiction of the optical pathways in luminescent concentrators. The ideal optical pathway is depicted in panel 1 in which an incoming photon is absorbed by a luminophore and then emitted into a waveguide mode that is total internally reflected. The re-absorption of luminophores in panel 2 represents a loss pathway when the luminophore quantum efficiency is not unity. Each time a luminophore absorbs or re-absorbs a photon and emits a photon there is a chance that the photon will be lost through the escape cone, seen in panel 3. Any non-radiative losses that arise from a non-perfect quantum yield are loss pathways, depicted in panel 4. Photons that are reflected, panel 5, or transmitted directly through the waveguide, panel 6, do not have the potential to be trapped within the waveguide and represent problematic optical cavity pathways.

Along with improvements in material efficiency, there has been an on-going exploration of concentration of light within optical cavities and the possibility of coupling the optical cavity to photovoltaics for luminescent solar concentration[141–145]. In a luminescent concentrator, incident photons are absorbed by a luminophore within the optical cavity waveguide and then the emitted photons are guided through total internally reflected modes throughout the waveguide (Figure 4.1). At the edges of the waveguide the concentrated light can then be collected by a solar cell and converted into energy. One of the distinct advantages of luminescent concentrators over geometric concentrators is the ability for luminescent concentrators to accept all light, including both direct and diffuse light, due to the presence of anisotropic randomly oriented absorbing luminophores, enabling the concentration of light within the waveguide when the luminophores emit into the total internally reflected modes of the waveguide instead of other potential loss pathways (Figure 4.1). However, the ability to concentrate photons within an optically cavity requires energy in order to effectively reduce the entropy of the photons. A fraction of the incident photon energy must be used to take incident photons and confine them within the geometric constraints of the waveguide. This energy difference can be the Stokes shift of the luminophore.

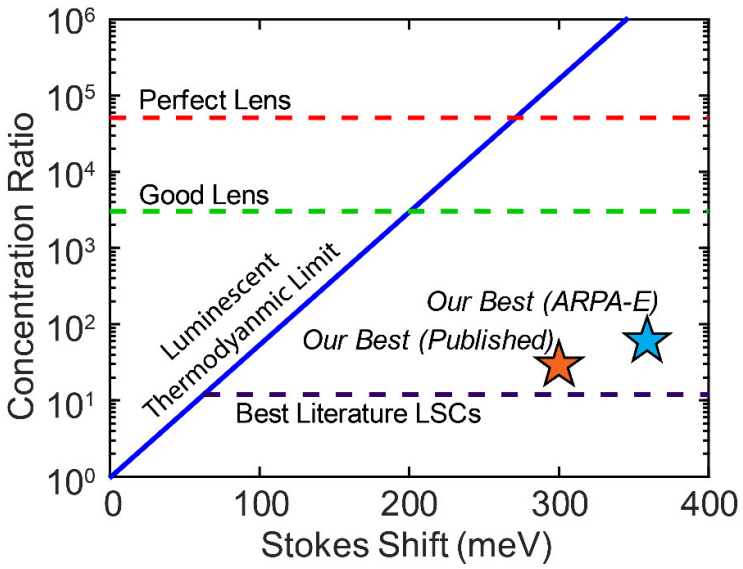

Figure 4.2: Theoretically achievable concentration ratio as a function of Stokes shift. By paying energy to reduce the entropy of light, photons can be concentrated within an optical cavity with the potential to surpass geometric concentration theoretically. Currently achievable luminescent concentrators suffer from several loss pathways from both the optical cavity quality and luminophore quality. As such there is a published[143] concentration factor of 30 and a measured concentration factor of ~60 from ARPAe MOSAIC, however these are far from the theoretical limit and represent a tremendous research opportunity.

The thermodynamics of the achievable concentration factor[146,147] was defined relative to the difference in absorption and emission energy (Figure 4.2). The expression indicates that as the Stokes shift increases, surpassing 300 meV, the achievable luminescent concentration within the waveguide has the potential to surpass even the geometric optical limit of a perfect lens while utilizing both direct and diffuse light. In addition to be able to accept light from all angles, the potential to reach concentration limits beyond the geometrical optics is another interesting theorized feature of luminescent concentrators. There are several research efforts underway to design luminescent concentrators for practical applications, with concentration ratios approaching 100x[145]. While this is a huge improvement over early luminescent concentrator designs, the achieved efficiencies are still orders of magnitude from the theoretical limit (Figure 4.2), presenting an enormous opportunity. The concentration factor has been limited from substantial parasitic losses and mitigating these loss pathways is critical to achieving extremely high efficiencies. While imperfect light trapping and scattering of propagating photons are optical cavity-based loss pathways that need to be overcome, the following discussion will focus on the luminophore performance, including non-unity PLQYs and reabsorption losses. Improving the performance of the luminophore has the potential to drastically change the achieved performance of luminescent concentrator devices.

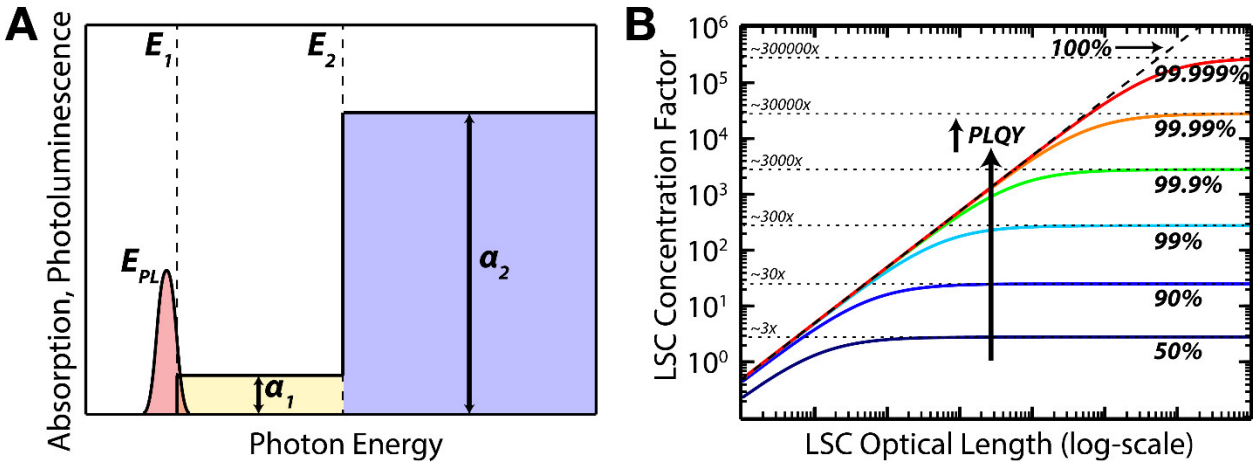

Figure 4.3: Impact of luminophore optical properties of concentrator performance. (A) Depiction of the ideal luminophore absorption spectrum for luminescent concentrators. A higher energy region (E_2) has a large absorption coefficient (α_2) and a lower energy region (E_1) has a smaller absorption coefficient (α_1) that is responsible for the photoluminescence of the luminophore, with the ideal case being α_1 having a very small absorption coefficient relative to α_2. (B) Shown is the achievable concentration factor of a luminescent concentrator over different concentrator optical lengths that experiences no optical losses from the cavity. The optical length includes many factors including the optical density, absorption coefficient of the luminophore, and physical size of the concentrator. In the diagram each line represents a different quantum yield (50%, 90%, 99%, 99.9%, 99.99%, and 99.999%) with increasing quantum yields resulting in increasingly large achievable concentration factors.

Neglecting any losses from the optical cavity itself and focusing on the luminophore performance, the impact that non-ideal luminophores have on the overall performance of a luminescent concentrator can be understood. Currently it is thought that luminophores with a step-like absorption profile is close to the ideal profile[145,146] with a large absorption coefficient at higher energies and a small absorption coefficient near the emission (Figure 4.3). Luminophores with a larger difference between the two absorption coefficients should perform better, ultimately minimizing the overlap of the absorption and emission spectra, reducing re-absorption. Each time that a photon is reabsorbed there is a chance that the photon is lost through non-radiative decay from non-perfect luminophores or emitted into a mode that is not total internally reflected[145,146]. With this motivation in mind, luminophores that have large Stokes shifts are advantageous (Figure 4.2) and are being actively developed. Several strategies have been attempted to reach large Stokes shifts while maintaining overall performance, including incorporation of intra-gap emissive defects or by using core/shell nanocrystals[143–146,148]. Quantum dots have appealing properties for use in luminescent concentrators, namely the ability to broadly tailor their absorption and emission properties through quantum confinement and by creating nanoscale epitaxial heterostructures.

In principle several material combinations might be able to achieve heterostructures with the desired absorption spectrum, but in practice very few have achieved the high PLQYs necessary to create high efficiency luminescent concentrators (Figure 4.3). A prototypical core/shell material that has been optimized to reach high PLQYs are the CdSe/CdS core/shell quantum dots, a material system that has received far more attention and optimization than other nanoscale heterostructures. By appropriately designing the quantum dot system, the focus of this discussion being the CdSe/CdS core/shell quantum dots, the difference in the idealized absorption coefficient regions can be orders of magnitude different. In these quantum dots the shell provides most of the

absorption while being spectrally separated from the CdSe core emission by >400 meV, this artificial Stokes shift produces an absorption spectrum that is close to ideal spectrum (Figure 4.1) with the potential to reach high concentration factors (Figure 4.2). As such, the focus of the following discussion will be on CdSe/CdS core/shell quantum dots and how these structures can be further optimized to reach near-unity PLQYs. As these materials continue to be optimized, they have the potential to achieve unprecedented levels of performance as luminophores in luminescent concentrator geometries.

4.3: CdSe/CdS Core/Shell Quantum Dot Material Synthesis

The cadmium chalcogenide quantum dot material systems are well-studied and synthetic protocols can reliably yield highly monodisperse nanoparticles[42,45]. There are now rational synthetic protocols to access cadmium chalcogenide nanoparticles with different shapes, including dots, rods, and plates[149,150]. Additionally, epitaxial heterostructures of different cadmium chalcogenides have a relatively small lattice mismatch, reducing the amount of interfacial strain between the two materials. For this discussion the focus is on CdSe/CdS quantum dots, and the lattice mismatch between CdSe and CdS is only 3.9%, a relatively small mismatch that can be tolerated at the interface. Using this type of geometry, quantum efficiencies have approached nearly 95% for moderate CdS shell thicknesses[42], typically maximized when growing 5 layers of CdS around highly monodisperse CdSe cores, but that efficiency begins to decrease as the shell thickness is further increased due to the quasi-type II nature of the heterostructure. The decrease in efficiency is very apparent as the shell thicknesses approaches the so-called giant shelled quantum dots[151–153], more than 15 layers of CdS, and the achieved PLQYs are typically around 30-70%. While a sample that presents nearly a 95% PLQY is impressive, the performance is insufficient to approach the performance limits in several applications that require the highest efficiency luminophores. By modifying and optimizing the synthetic protocol, the efficiencies of the synthesized CdSe/CdS quantum dot ensembles have been shown to reach as high as 99.6±0.2%, although this is not thought to be upper-bound of achievable efficiency. The ability to measure the efficiencies of these ensembles with sufficiently low uncertainty to fully characterize these highly efficient ensembles will be discussed later in this dissertation.

4.3.1: Chemicals Used in the Synthesis of CdSe/CdS

Cadmium Oxide (CdO, 99.99%, Sigma Aldrich), n-octyldecylphosphonic acid (ODPA, 99%, PCI Synthesis), tri-n-octylphosphine oxide (TOPO, 99%, Sigma Aldrich), tri-n-octylphosphine (TOP, 97%, STREM), selenium (Se, 99.999%, Sigma Aldrich), 1-octadecene (ODE, 90% tech grade, Sigma Aldrich), oleic acid (OA, 90% tech grade, Sigma Aldrich), 1-octanethiol (OctSH, 99%, Sigma Aldrich), hexanes (mixture of isomers, anhydrous 95%, Sigma Aldrich), toluene (anhydrous 99.5%, Sigma Aldrich), and methyl acetate (anhydrous 99.5%, Sigma Aldrich) were purchased and used without further purification.

4.3.2: Synthesis of Wurtzite CdSe Cores

Wurtzite cadmium selenide (CdSe) cores were synthesized according to previously reported literature procedures[154] with minor modifications reported in a published protocol[45]. Briefly, 60 mg CdO, 280 mg ODPA, and 3 g TOPO were added to a 25 mL 3-neck round bottom flask with a thermocouple adapter, a silicone septum, and a glass air condenser column connected to a Schlenk line. This mixture was heated to 150 °C under vacuum to degas the reaction for 1.5 hours. Afterwards, the reaction was heated to 320 °C under argon to complex CdO into $Cd(ODPA)_2$, typically taking between 1-2 hours to complete. Once $Cd(ODPA)_2$ complexation was completed, the reaction mixture was heated to 372 °C and a syringe of 1.5 g TOP was injected into the reaction while the temperature was ramping. After the temperature stabilized at 372 °C, a syringe with pre-prepared TOP:Se (58 mg Se dissolved in 360 mg TOP) was swiftly injected into the reaction mixture to initiate the growth of CdSe cores. The mixture reacted for between 30-60 seconds until the desired core size was reached, and then the reaction was quickly cooled to around 100 °C. To prevent TOPO precipitation, 3 mL of toluene was injected into the cooled reaction mixture and transferred into an argon-filled glovebox for air-free cleaning. The CdSe quantum dots were precipitated from the reaction mixture using methyl acetate and then resuspended in hexanes. The precipitation and resuspension were repeated another two times, finally suspending the cores in 3 mL of hexanes for further use.

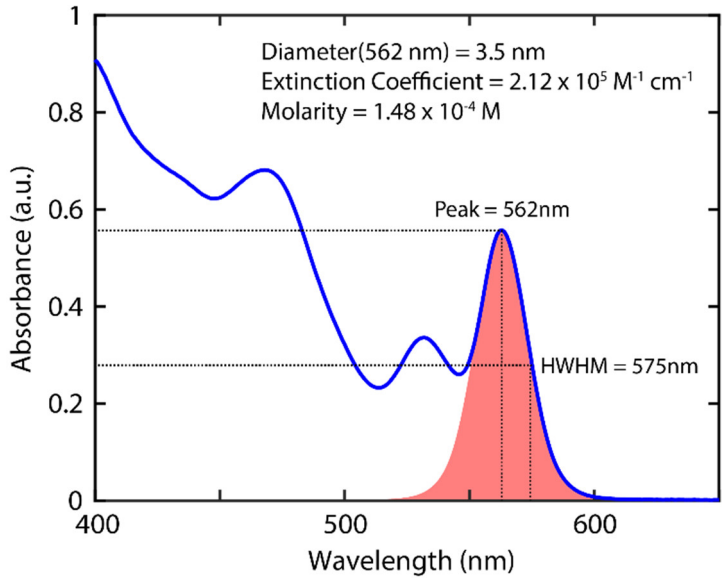

Figure 4.4: Band edge absorption spectrum of as-synthesized CdSe cores. Shown is a typical absorption spectrum of the synthesized cores, this spectrum for 3.5 nm diameter CdSe cores. Values extracted from these absorption spectra are used to determine the size and molarity of the isolated CdSe core quantum dots.

The concentration of the cleaned cores solutions was typically maintained around 0.1 mM for 3.5 nm diameter cores, a size that reliably produces high efficiency core/shell quantum dots. The size and absorption coefficient of the cleaned CdSe cores was determined by using the optical absorption curve previously reported[154] that is based on the position of the E_{1S} optical absorption peak (Figure 4.4). Although the ideal case is a perfectly monodisperse CdSe core sample, each reaction presents a size distribution that the concentration needs to be scaled against, assuming a normal distribution. With isolated and cleaned CdSe cores, the next step is the epitaxial shell growth.

4.3.3: Overgrowth of CdS to Access CdSe/CdS Core/Shell Quantum Dots

The CdS shelling reaction employed is based off a previously reported literature protocol[42] with modifications later detailed in a published protocol[45]. Briefly, at the typical 100 nanomole reaction scale, 6 mL of ODE was loaded into a 50 mL 3-neck round bottom flask and degassed at 110 °C under high vacuum for 1 hour. After degassing, 100 nanomoles of the previously synthesized CdSe cores were added into the reaction flask and thoroughly degassed to remove hexanes. Afterwards, the reaction was placed under Argon and the temperature was increased to 240 °C. Once the reaction reached 240 °C, a slow injection of two equal volume reagent syringes was started, with one syringe containing a previously prepared 0.2 molar $Cd(Oleate)_2$ solution and the other syringe containing a 0.2 molar OctSH in ODE solution, at a rate of 3 mL/hr. The volume of reagents required to achieve certain CdS shell thicknesses (the actual thickness will be slightly less due to a non-quantitative shelling reaction) can be calculated by:

$$r_{CdSe/CdS} = r_{CdSe} + Target\ Number\ of\ Monolayers \times 0.416nm/monolayer \tag{4.1}$$

$$N_{Cd}(moles) = \left(V_{Target}(cm^3) - V_{core}(cm^3)\right) \times \rho_{CdS}\left(\frac{g}{cm^3}\right) \times N_A \times Target\ Moles \times \frac{1}{MW_{CdS}} \tag{4.2}$$

$$Injection\ Volume = \frac{N_{Cd}}{Molarity_{Cd(Oleate)_2}} \tag{4.3}$$

Typically, the shelling reactions are conducted at 100 nanomoles of CdSe cores (Target Moles) and between 4-13 monolayers of CdS (Target Number of Monolayers); however, the reaction can be conducted over a range of concentrations. After the slow injection is started, the reaction temperature was increased to 310 °C to allow the shell to grow for the remainder of the injection. Following the injection, the mixture remained at 310 °C for an additional 10 minutes to consume the remaining excess precursors and then the reaction was cooled to room temperature. The room temperature solution was air-free transferred to an argon filled glovebox for cleaning. The CdSe/CdS quantum dots were precipitated from the reaction mixture using methyl acetate and then resuspended in hexanes. The precipitation and resuspension were repeated another two times, finally suspending the cores in 3 mL of hexanes. Additional cleaning is required to remove the remaining ligand and ODE in solution, but excessive cleaning can result in surface ligand stripping which negatively affects the PLQY of the sample. The resulting CdSe/CdS quantum dot solutions typically were in the 40-50 micromolar concentration range depending on the number of quantum dots lost during the cleaning steps.

4.4: Traditional Characterization of CdSe/CdS Quantum Dots

Consistent with their use in applications that require high optical efficiency, the CdSe/CdS samples are primarily characterized optically through a combination of absorption, photoluminescence (PL), photoluminescence quantum yield (PLQY), and time-resolved PL lifetime (TRPL). Additionally, to ensure consistency the size and shape of the ensembles were analyzed using transmission electron microscopy (TEM).

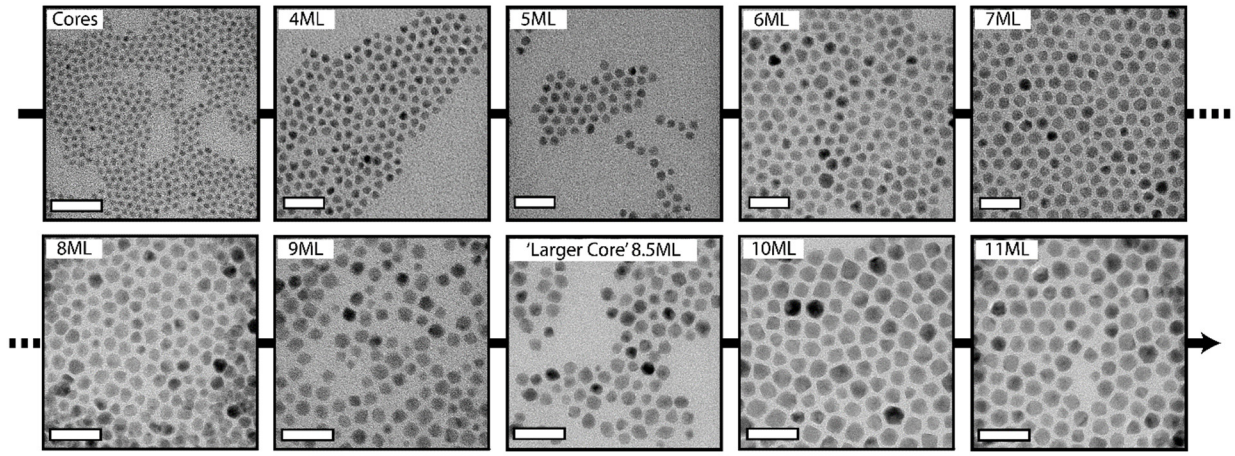

Figure 4.5: Example TEM images of a size series of CdSe/CdS quantum dots. Multiple images like those shown are used to determine the sizing distributions for each sample, ensuring consistency of expected and realized shell growth with each sample labeled with their theoretical shell growth thickness. The scale bar in each image is 25 nm. All the samples except for the one labeled 'Larger Core' 8.5 ML were prepared using the same size CdSe core, 3.5 nm diameter. The sample labeled 'Larger Core' 8.5 ML presented the highest photoluminescent quantum yield of all samples measured, although the cores were slightly larger.

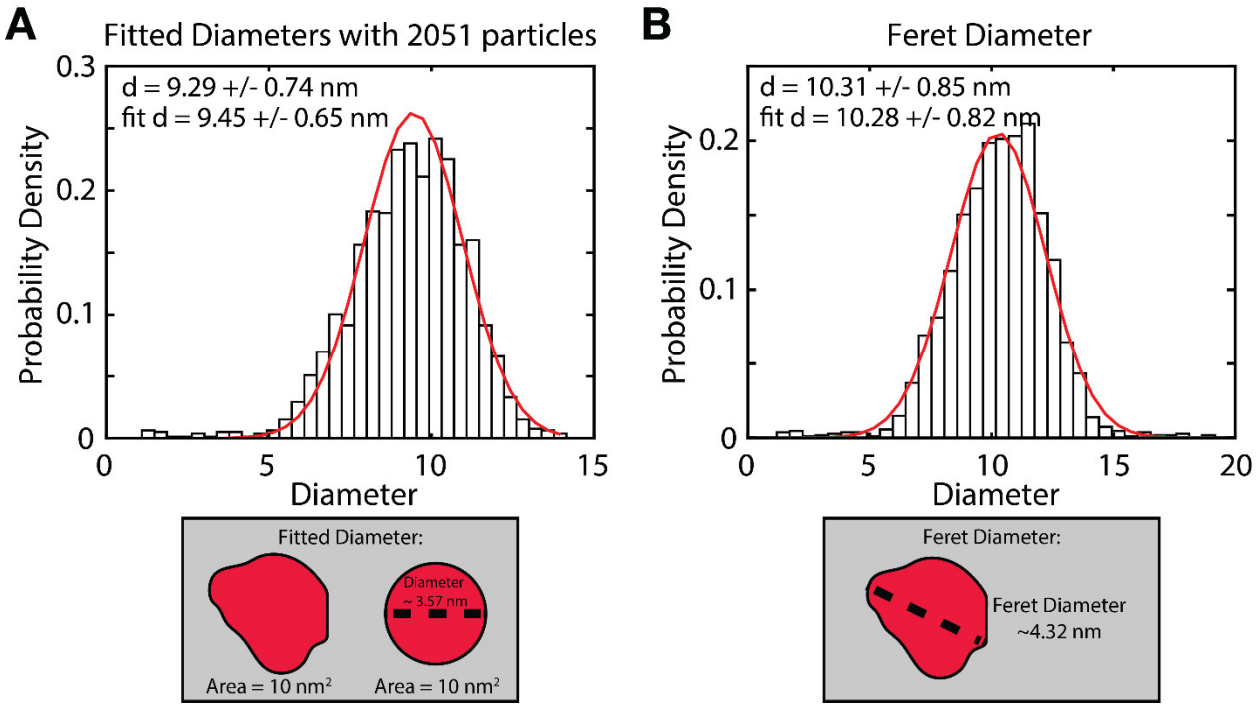

Figure 4.6: Representative sizing diagram for nanoparticle TEM size analysis. Shown are example histograms used to determine the (A) fitted diameter and (B) the feret diameter of the nanocrystal ensemble. Schematic descriptions for the definition of fitted and feret diameter can be found below the respective histograms. The sizing algorithm employed for TEM image analysis has been described elsewhere[143].

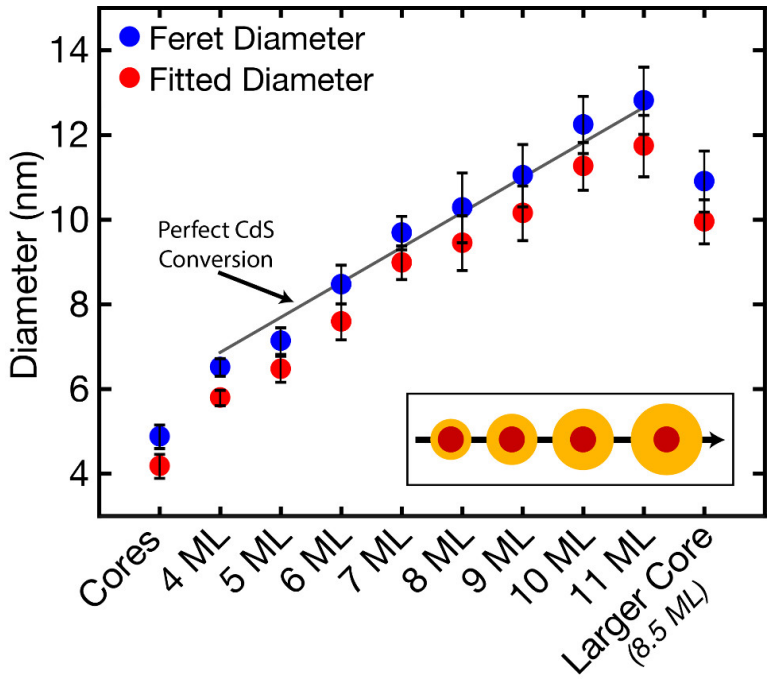

Figure 4.7: Summary of TEM sizing results for the CdSe/CdS particle series analyzed. For each data point hundreds of particles were analyzed using an automated sizing script, with a fitted and feret diameter for each sample along with the standard deviation (±1σ). Due to the faceting that occurs as the shell grows thicker, the determined feret diameter becomes larger than the perfect stoichiometric CdS shell growth although this is an artefact of faceting. The fitted diameter is smaller than the maximum achievable thickness, consistent with the expectations of a non-perfect reaction yield.

For the TEM analysis, samples were prepared by diluting the quantum dot stock solutions in toluene (OD < 0.1) and then drop-casting ~10 μL of the solution onto a TEM grid. All TEM images were taken on a FEI Tecnai T20 S-Twin TEM operating at 200 kV with a LaB_6 filament and a Gatan Orius SC200 camera. A set of the representative TEM micrographs are shown in (Figure 4.5) for CdSe/CdS quantum dots with different CdS shell thicknesses, ranging from CdSe cores to CdSe/CdS quantum dots with 11 monolayers of CdS. To target CdSe/CdS ensembles with different thicknesses, different volumes of precursors are added assuming a stoichiometric growth of CdS shell, but the reaction is not stoichiometric requiring TEM sizing to verify the extent of the reaction. From each sample, the sizing distributions were determined using a custom written MATLAB script[143] measuring several hundreds to thousands of quantum dots (Figure 4.6). Although the shell reaction does not have a perfect conversion as expected, the achieved shell growth is consistent between reactions, and the achieved trend follows a predictable trajectory over the size range of interest (Figure 4.7).

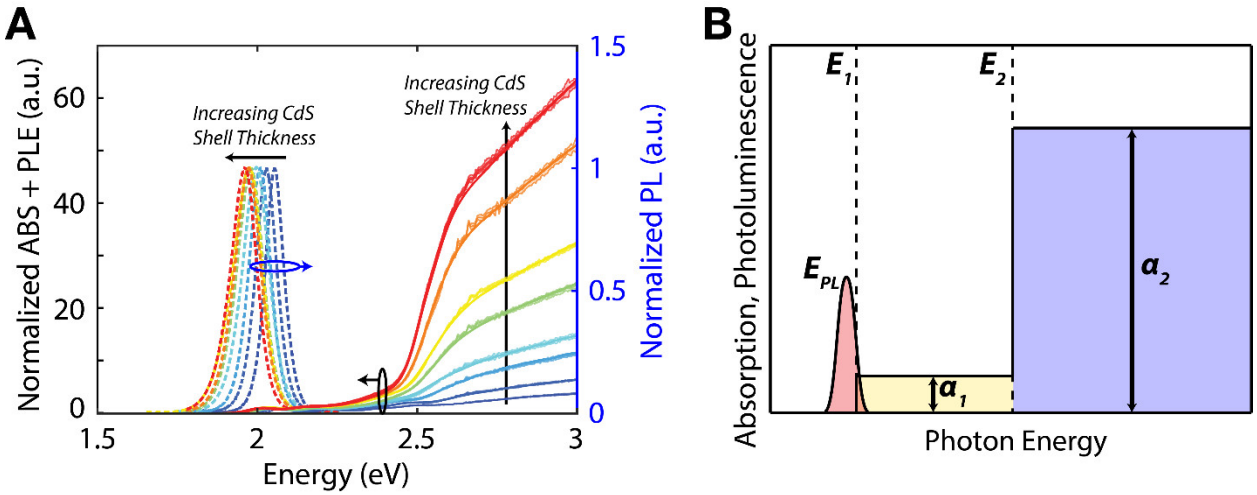

Figure 4.8: Standard optical characterization of CdSe/CdS samples. (A) Shown are the normalized absorption and photoluminescence excitation (PLE) spectra of a size series of CdSe/CdS core/shell quantum dots with the same size CdSe core (3.5 nm diameter) but different CdS shell thickness (4 – 11 monolayers). The absorption and PLE are normalized to each other, displaying a high overlap between the two. The photoluminescence spectra are normalized to each other. (B) Idealized absorption and photoluminescence spectrum for optimal luminophores for luminescent concentrators.

The CdSe/CdS quantum dot samples have distinct optical features that can be reliably measured to understand the ensemble. Steady state absorbance spectra were acquired using a Shimadzu UV-3600 double beam scanning spectrometer on dilute solutions to minimize the influence of scattering in the blue and UV (Figure 4.8). As the thickness of the CdS shell increases, the absorption of the CdS shell dominates the higher-energy absorption region, consistent with the increasing volume fraction of CdS within the quantum dot. Solution phase PL spectra were collected using either a calibrated scanning PMT spectrometer or calibrated CCD spectrometer (Figure 4.8). As expected for a quasi-type II band alignment quantum dot, the PL bandgap of the ensemble redshifts as the shell thickness increases due to the delocalized electron and core-localized hole (Figure 4.8). Consistent with the narrow size distributions of these samples determined from the TEM sizing analysis (Figure 4.7), the ensembles present PL spectra with 25-32 nm PL linewidths depending on the shell thickness (Figure 4.8).

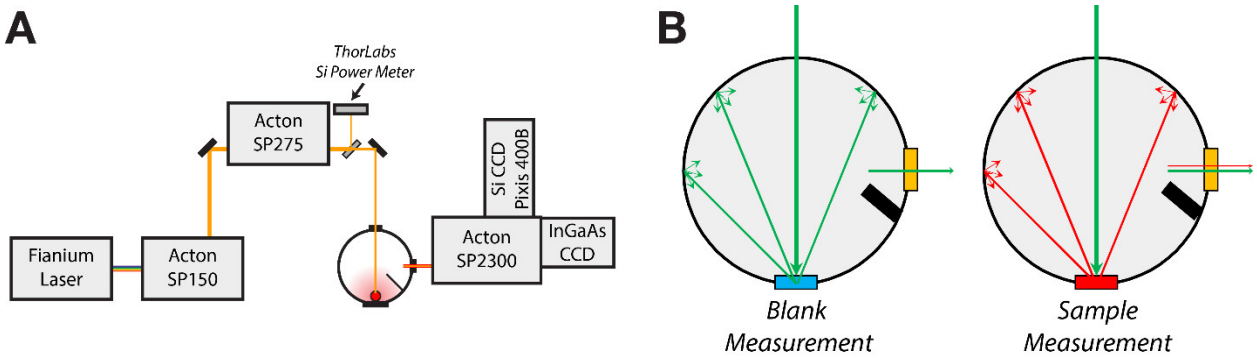

Figure 4.9: Schematic depiction of the home-built integrating sphere setup. (A) Shown is a schematic overview of the integrating sphere setup used to measure quantum yields. A brief description of the beam path follows in the text. (B) Schematic overview of the measurement, requiring the collection of a blank and sample for analysis.

The PLQYs of the ensembles were taken using a home-built integrating sphere setup (Figure 4.9), described more completely elsewhere[155]. Briefly, a Fianium SC450 pulsed supercontinuum laser provides a bright collimated white light source that is monochromated through two monochromators, an Acton Research SP150 and Acton Research SP275. After the two monochromators, the resulting excitation bandwidth is between 0.5 – 1.0 nm depending on the slit widths. The monochromatic light is passed through a beam-splitter and a fraction of the light is collected with a calibrated power meter while most of the light enters a Spectralon integrating sphere. Within the integrating sphere, samples are held using a custom-milled Spectralon holder directly in the beam path. Light exiting the integrating sphere is focused onto the entrance of a SP2300 monochromator and collected using a thermoelectrically cooled Princeton Instruments PIXIS 440B silicon CCD. The setup is corrected for both spectral positions using a combination of neon and mercury wavelength calibration lamps, as well as corrected for sensitivity using a NIST-traceable radiometric calibration lamp from Ocean Optics. An integrating sphere setup can measure PLQYs with uncertainties approaching ±2.5% depending on the spectral position of the PL spectrum.

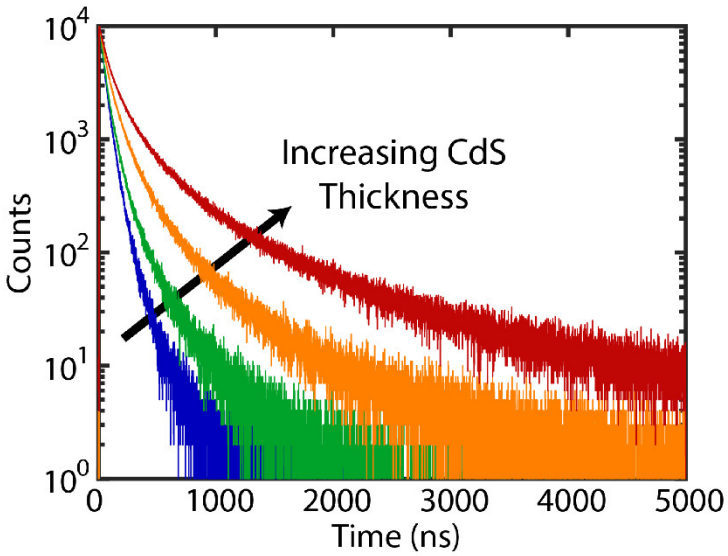

Figure 4.10: Example time-resolved photoluminescence of the CdSe/CdS quantum dots. Shown are a representative set of photoluminescence lifetimes under 407.1 nm pulsed excitation measured for the 8-, 9-, 10-, and 11- monolayer CdSe/CdS quantum dots. Despite presenting high quantum yields (>90%), the photoluminescence lifetimes present multi-exponential decays that are not characteristic of simple two-level systems.

To further resolve the excited state dynamics of the quantum dot samples, the time-resolved photoluminescence (TRPL) measurements were performed using a PicoQuant Fluotime 300 with a PMA 175 detector with either a 407.1 nm pulsed laser diode or a monochromated pulsed Solea supercontinuum laser system with an excitation range of 480-560 nm. The lifetimes were collected using time-correlated single photon counting (TCSPC), measuring the characteristic time that a luminophore stays in its excited state following excitation. From the TRPL measurements of the samples, it is apparent that none present a mono-exponential decay, but instead something more multi-exponential (Figure 4.10). For the discussion that follows a weighted average lifetime using a bi- or tri-exponential fit will be used to compare samples. It is difficult to know the correct fitting

model to use for such decays and likely a distribution of exponentials will most accurately capture the decay; however, care will need to be taken for the interpretation of such a decay fitting for these systems. Consistent with Equation 1.2, the excited state lifetime is determined from a combination of the radiative recombination and non-radiative recombination rates. The combination of these characterization techniques provides a synthetic feedback loop to improve the performance to within a few percent of unity PLQY.

4.5: Measurement of Near-Unity PLQY CdSe/CdS Quantum Dots

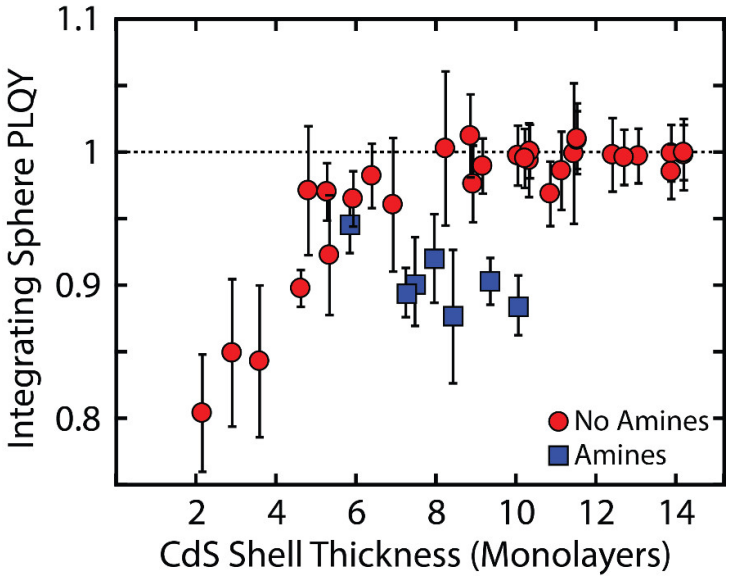

Figure 4.11: Achieved quantum yields for a range of CdSe/CdS quantum dot shell thicknesses. Shown are a representative, not exhaustive, series of CdSe/CdS quantum yields for particles with 3.5±0.2 nm diameter CdSe cores and a range of shell thicknesses. Compared are the differences between the CdS shell growth reaction with and without amines, showing higher efficiencies after 5-monolayers of CdS for reactions without amines. The error bars represent the uncertainty of the integrating sphere quantum yield measurements due to spectral radiance transfer standard required to calibrate the spectral sensitivity of the instrument. Values can be measured to be higher than unity, non-physical for this system, due to artefacts from measurement uncertainty.

The basis of our quantum dot synthesis originated from Chen et al.[42] in which a slow injection of shell precursors allows for the growth of a highly crystalline CdS shell around a monodisperse CdSe core reaching quantum yields up to ~95% while maintaining a highly monodisperse ensemble with regular morphologies. However, in this synthesis there is a substantial decrease in the ensemble PLQY as the CdS shell thickness continues to increase (Figure 4.11), most substantially observed in the reported giant shelled quantum dots, in which the PLQY begins to approach nearly 50%[151–153]. The achieved efficiencies using that synthetic preparation are impressive but insufficient for applications that require minimal losses, encouraging the development of a new synthesis method. While the use of oleylamine in the synthesis maintains uniform size distributions, they can also aid in the undesirable desorption of the Z-type cadmium oleate surface bound ligands[156–159], introducing problematic surface states. By omitting amines from the synthesis, the achievable size-distributions are broader due to the more reactive shell growth conditions, but the radiative efficiency remains high, even exceeding the amine preparation (Figure 4.11), as the surface-bound ligand density remains high. Once the shell thickness exceeds

2 nm, the ensemble PLQY consistently exceeds 90±3%, and after only 4 nm of shell the PLQY tends to exceed 97±3% (Figure 4.11). After a certain shell thickness, the PLQY of samples are indistinguishable within the measurement uncertainty of the integrating sphere measurement, hindering complete characterization of samples.

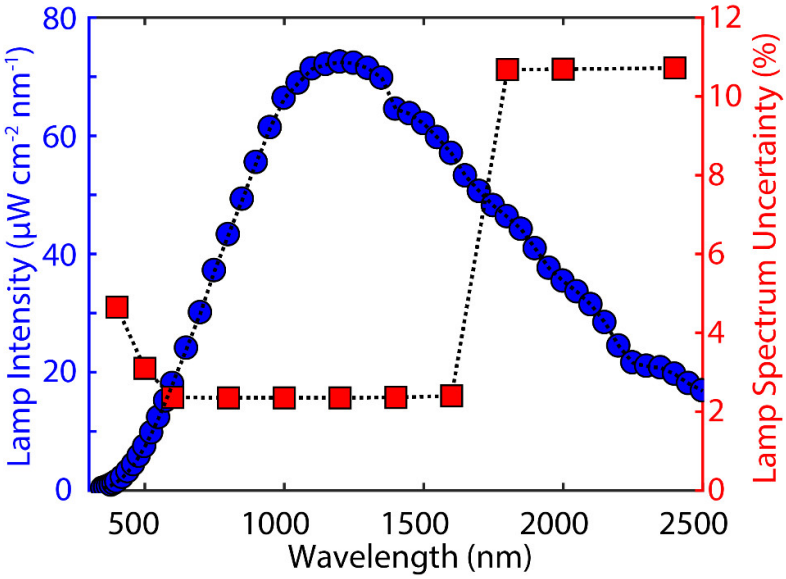

Figure 4.12: Intensity and uncertainty of the spectral radiance transfer standard. Shown is the calibrated intensity and uncertainty of the Ocean Optics HL-3Plus spectral radiance transfer standard over the visible and near-infrared. The light source is used to calibrate the spectral sensitivity of the silicon-CCD cameras used to measure the quantum yield. This calibration standard introduces at least 2.5% relative systematic uncertainty into the integrating sphere quantum yield measurements (i.e. 100±2.5%, 50±1.25%, 1±0.025%, etc.). This systematic uncertainty substantially limit certainty as the quantum yield approaches nearer to unity.

Although a powerful characterization tool for the optical performance of quantum dots, once the ensemble PLQY of a sample is within a few percent of unity, existing measurements techniques are unable to distinguish sample performance sufficiently to provide useful feedback for further synthetic refinement due to measurement uncertainty. The most common measurement PLQY measurement techniques are the relative dye and integrating sphere techniques, which both require a spectral sensitivity calibration that introduces at least 2.5% or more uncertainty[124] as a result of the spectral radiance transfer standard uncertainty alone (Figure 4.12). Unfortunately, this uncertainty limits synthetic refinement when the PLQY approaches near-unity and as such a new measurement technique to overcome this limitation was developed. When a quantum dot is excited by a photon, the absorbed photon promotes a ground-state electron into a higher energy excited state leaving behind a hole. The excited quantum dot then has the potential to either emit a band-edge photon radiatively or lose the excitation through heat by non-radiative recombination pathways. Traditional techniques are sensitive to the radiative events, measuring the number of photons that emerge from the excited nanocrystal ensemble. The ability to count photons becomes increasingly difficult when attempting to count 999 out of 1000 photons compared to 500 or 900 out of 1000 photons. Developing a technique that is sensitive to the infrequent non-radiative recombination of the excited state instead of the very common radiative recombination as the

ensemble quantum yield approaches nearer to unity offers a promising path towards overcoming this measurement limitation.

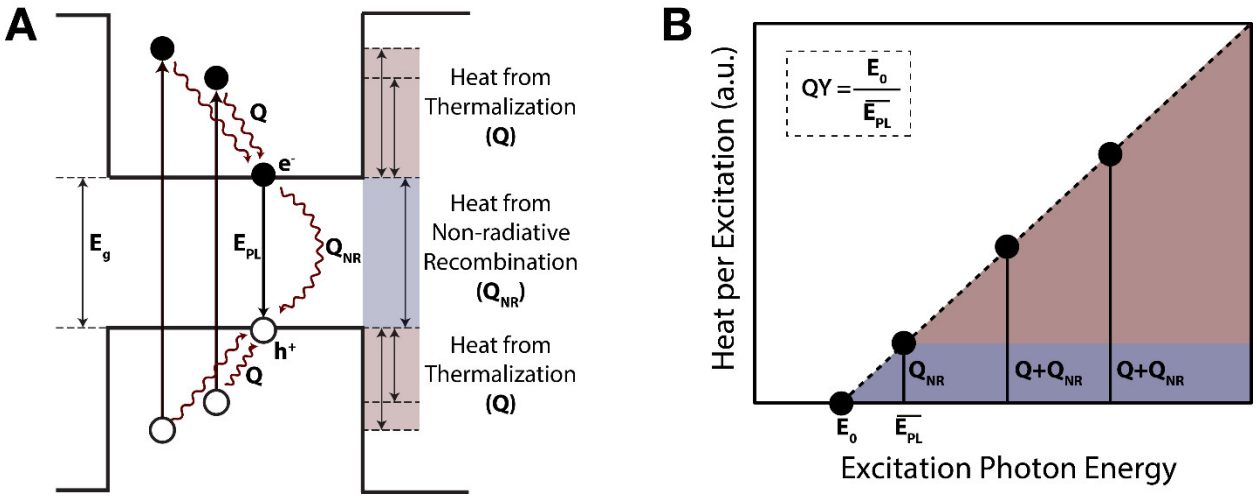

Figure 4.13: Origin of major heat pathways from a photo-excited semiconductor. (A) There are many states that a semiconductor can access when photo-excited, potentially creating hot electrons and/or hot holes. On fast timescales (order of picoseconds or faster) the carriers thermalize to the band edge releasing heat from that thermalization process (Q). Once at the band edge the carriers can recombine radiatively to emit a band edge photon with energy E_{PL} or non-radiatively and releasing additional heat (Q_{NR}). (B) By sweeping the excitation photon energy, the quantum yield can be determined by comparing the measure photoluminescence band gap and the threshold in which no heat is generated by a linear regression.

By looking more closely, during photo-excitation of a semiconductor an absorbed photon excites a ground-state electron into a higher energy excited state leaving behind a hole, and both excited charge carriers relax to the band-edge by releasing excess heat into the host crystal on the picosecond timescale (Figure 4.13). The amount of heat released depends on how much extra excitation energy was present relative to the bandgap. Later, on the order of nanoseconds, the thermalized electron and hole recombine returning the material to its ground state either radiatively or non-radiatively (Figure 4.13). During the non-radiative recombination there is additional heat released that is characteristic of the non-unity PLQY so that quantum dots with a lower PLQY emit more heat. Using a technique to measure the excitation energy dependent heat that is generated, the fraction of emitted heat that originates from non-radiative recombination can be extracted (Figure 4.13). The measurement technique that was developed utilizes photothermal deflection spectroscopy (PDS) and a calibrated CCD to measure the resulting average PL bandgap of the ensemble to measure the excitation energy threshold that results in positive heat generation (Figure 4.13), called photothermal threshold quantum yield (PTQY).

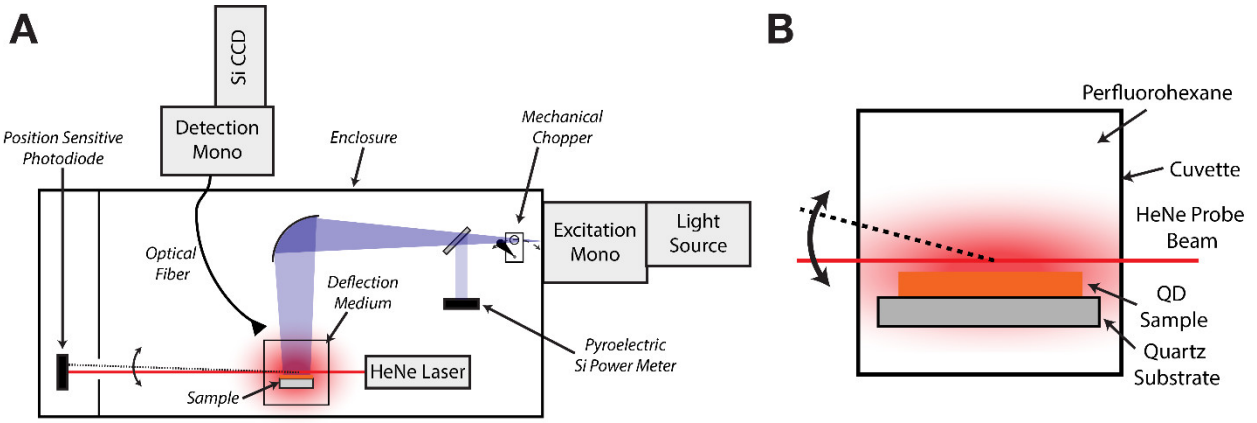

Figure 4.14: Schematic depiction of the photothermal threshold quantum yield instrument. (A) Schematic overview of the key components of the PTQY spectrometer. (B) Schematic zoom-in at the sample to show the sample positioning in the HeNe laser beam path.

A full description of the PTQY instrument can be found in the supporting information elsewhere[45], while a brief overview description follows. The PTQY instrument is built from a modified transverse PDS apparatus used to measure heat generated from films. The transverse PDS[45,160,161] has a custom-milled sample holder to controllably position thin film samples deposited on polished optical quartz substrates with low surface roughness through either spin-coating or drop-casting to ensure a uniform deflection path. The thin film is submerged in a deflection medium, a liquid that has a well-characterized change in refractive index with temperature. Many solvents have a linear change in refractive index over a range of temperatures; however, most measurements for PTQY generate a relatively small amount of heat. To ensure minimal quantum dot perturbation and ensure that the quantum dots remain robustly attached to the quartz substrate perfluorohexane was chosen as the deflection medium for investigating CdSe/CdS quantum dot thin films. Relatively close to the sample, a stable HeNe laser is passed through the deflection medium directly next to the thin film. The HeNe laser position is adjusted to be close to the quantum dot thin film surface, but not graze the surface, minimizing potential measurement complications. When the sample is illuminated the HeNe laser beam is deflected by thermal lensing of the deflection medium as a result of the heat generated, and the deflection angle is measured using a position-sensitive diode (Figure 4.14). The excitation source, for the experimental realization a xenon lamp, is chopped to enable lock-in measurements to measure small deflection angles with certainty (Figure 4.14) from the heat generated. The final main component arm of the PTQY instrument is a fiber-couple silicon CCD detector that is used to measure the average PL bandgap energy emitted from the quantum dot thin film (Figure 4.14). The detection arm has wavelength and sensitivity calibrated to determine the correct shape of the PL spectrum.

With this measurement geometry, the quantum yield is extracted by measuring the ratio of photothermal deflection to the PL as a function of excitation energy. The heat generated from thermalization of carriers and the non-radiative loss are then effectively separated as the slope and intercept of a line (Figure 4.13):

$$I_{PL} = \phi_{exc} \times C_{PL} \times A \times QY \tag{4.4}$$

$$D_{PT} = \phi_{exc} \times C_{PT} \times A \times (E_{exc} - E_{PL} \times QY) \tag{4.5}$$

$$\frac{D_{PT}}{I_{PL}} = C \times (E_{exc} - E_{PL} \times QY) \tag{4.6}$$

In which, I_{PL} is the number of PL photons detected, A is the absorbance, ϕ_{exc} is the excitation flux, D_{PT} is the photothermal deflection voltage, E_{exc} is the average excitation energy, E_{PL} is the average emission energy, C_{PL} is the collection parameter for PL detection, C_{PT} is the photothermal deflection sensitivity, and QY is the quantum yield. By defining E_0 to the excitation energy when $D_{PT}/I_{PL} = 0$, the expression becomes:

$$QY = \frac{E_0}{E_{PL}} \tag{4.7}$$

Therefore, the quantum yield is determined through a ratio of the non-radiative and radiative emission components, both values that can be precisely determined using the PTQY measurement technique.

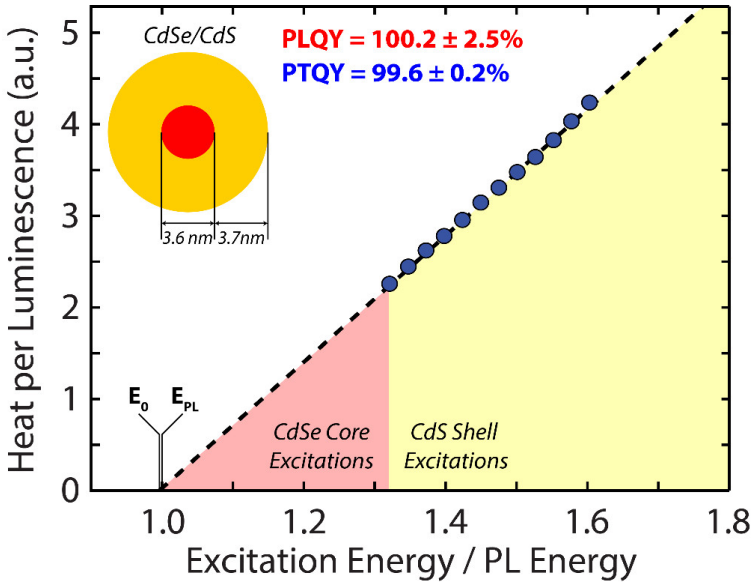

Figure 4.15: Measured quantum yield of the current champion CdSe/CdS sample with PTQY. Shown is the experimental data for the highest quantum yield sample measured to date, a CdSe/CdS core/shell sample with a 3.6 nm diameter CdSe core and 3.7 nm thick CdS shell. The measured PLQY with the integrating sphere setup was determined to be 100.2±2.5%, whereas the quantum yield measured with PTQY was determined to be 99.6±0.2%. Due to small amount of heat generated when exciting the CdSe core, the quantum yield with PTQY was determined by fitting the CdS shell excitations as shown.

Critically, a measurement of the ratio of non-radiative to radiative emission components in PTQY removes the spectral radiance transfer standard dependence that is critical for traditional PLQY measurements. Instead, the measurement only requires the measurement of the excitation energy, E_{ex}, and PL energy, E_{PL}, values that can be determined more accurately than the uncertainties from the spectral radiance transfer standard. As such, by requiring the standard to

determine the correct shape of the PL spectra, there is only 0.0006% introduced to the overall uncertainty of the measurement from the standard. There are other sources of uncertainty that are present, including 0.02% from the detection spectrometer wavelength accuracy and 0.1-0.2% from finite averaging, but the realized version of this measurement technique, even at 0.2%, has nearly 100x less uncertainty than traditional PLQY measurement techniques. The highest QY measured with PTQY[45] was 99.6±0.2%, a value measured for higher energy shell excitations of a 3.6 nm diameter CdSe core with a 3.7 nm thick CdS shell (Figure 4.15). With this measurement technique, CdSe/CdS can be synthetically refined and characterized at efficiencies not accessed previously.

4.6: Characterization of CdSe/CdS Quantum Dots Size Series

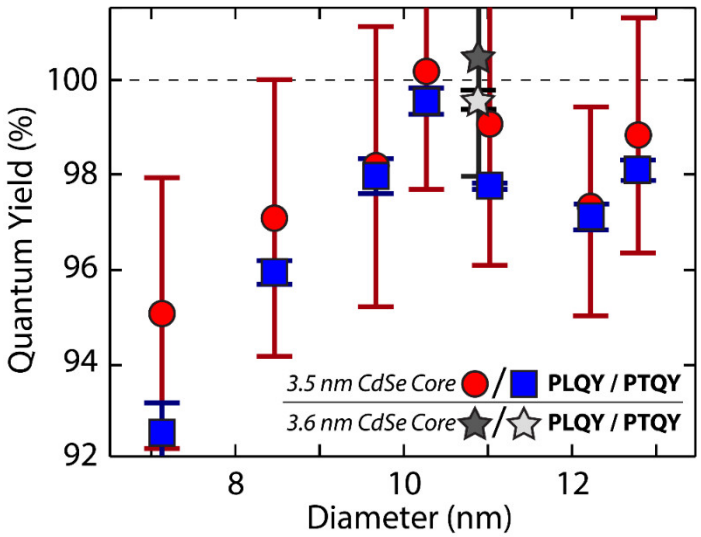

Figure 4.16: Comparison of integrating sphere and photothermal measured quantum yields. Shown is the size series of CdSe/CdS core/shell quantum dots comparing the quantum yield determined using traditional integrating sphere measurements and from photothermal threshold quantum yield for the same samples. Stars represent the highest quantum yield sample (99.6±0.2%) measured, the sample with a comparable but slightly larger core than the remainder of the size series. Error bars represent the measurement uncertainty.

Importantly, the sensitivity of the PTQY measurement technique enables a systematic investigation of high-quality CdSe/CdS when the PLQY surpasses 95%, despite the inability to distinguish the different CdSe/CdS samples near-unity when using the traditional PLQY measurement techniques. From PTQY there is a peak in the quantum yield of the CdSe/CdS samples when the CdS shell thickness is 8±0.5ML (Figure 4.16), a peak that is obscured by the systematic uncertainty of other measurements (Figure 4.11). As a result of this measurement uncertainty, the systematic optimization of CdSe/CdS quantum dots as the efficiency approaches nearer to unity has been hindered but now further optimization is possible using PTQY.

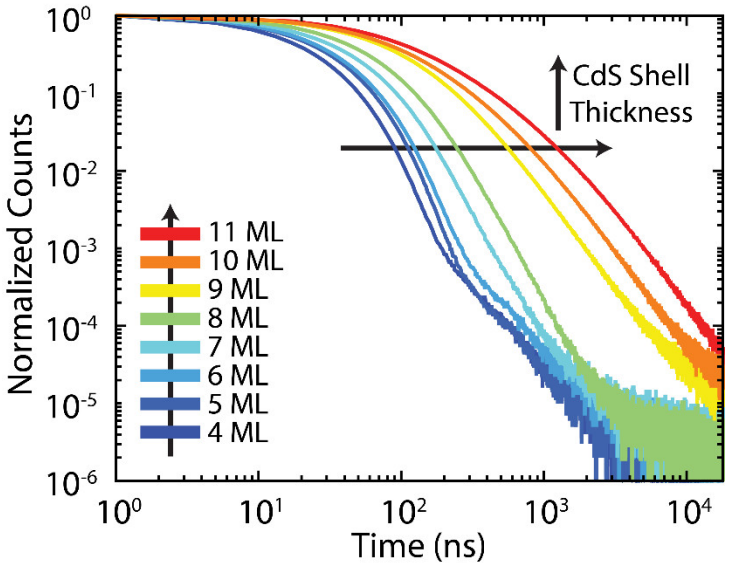

Figure 4.17: Time-resolved photoluminescence lifetimes of the CdSe/CdS size series. Shown is the series of excited state lifetime decays for the CdSe/CdS size series from 4- to 11-monolayer thick CdS shells. Decays are collected at 407.1 nm pulsed excitation with a range of 1 million counts for each sample, shown out to 20 microseconds after then pump excitation to capture the long-lifetime behavior of the quantum dots.

By measuring a series of particles with different shell thickness between 4 and 11ML (Figure 4.8), the origin of the peak in quantum yield can be rationalized through a combination of PTQY (Figure 4.16) and TRPL (Figure 4.17) measurements. When the shell thickness is less than 8ML, there is an insufficient surface passivation[162,163] present consistent with surface hole traps apparent in the TRPL decays as a long tail past ~100 ns (Figure 4.17) resulting in significantly lower efficiencies (Figure 4.16). At and above 8ML thick CdS shells, the TRPL decays are well-fit with a bi-exponential decay (Figure 4.17), but the excited state lifetimes become significantly longer as the shell thicknesses increases. This increasing excited state lifetime is rationalized as the result of the quasi-type II band alignment, in which a thicker shell reduces the overlap between the delocalized electron and core-localized hole. The reduced wavefunction overlap decreases the radiative recombination rate of the CdSe/CdS heterostructure, causing even small non-radiative recombination rates to become more substantial relative to the radiative recombination rate, which decreases the quantum yield.

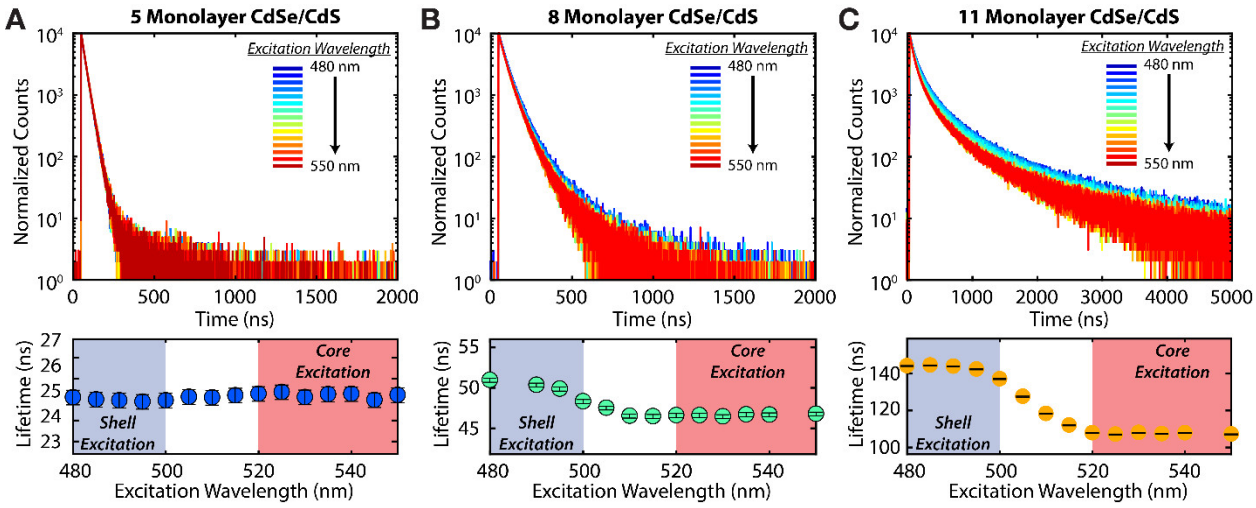

Figure 4.18: Excitation wavelength dependent photoluminescence decay lifetimes. Shown are a set of representative excitation wavelength dependent PL decays for a 5-, 8-, and 11-monolayer CdSe/CdS quantum dot ensembles, all with the same core size but different shell thicknesses. Excitations range from 480 to 550 nm, and the extracted average lifetimes are plotted below each representative plot, showing a distinct difference for shell and core photo-excitations for the 8- and 11-monolayer samples but not for the 5-monolayer sample.

Further, it is important to probe the wavelength-dependent response of the material to distinguish the difference between shell and core excitations with quantum yield measurements and TRPL measurements. For the 5ML CdS shell thickness ensemble, there is no difference in lifetimes measured for core or shell excitations, both are around 25 ns (Figure 4.18). However, for the largest shell thickness ensembles there is a 35% increase, from 110 to 145 ns, in the lifetime for shell excitations relative to core excitations (Figure 4.18).

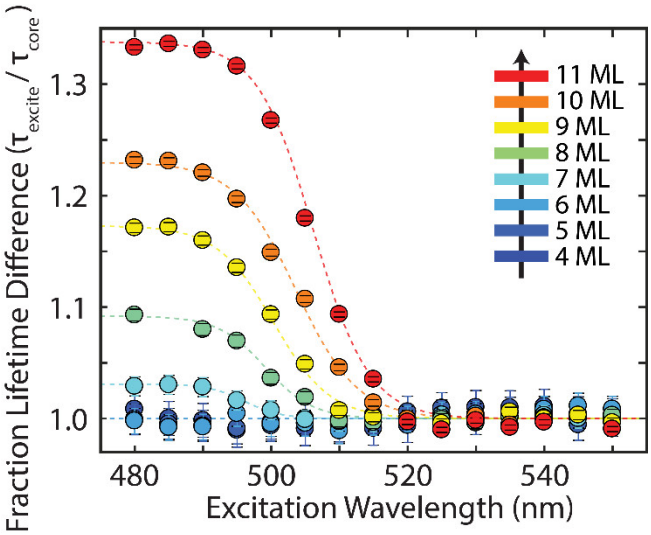

Figure 4.19: Excitation dependent photoluminescence lifetimes normalized to core lifetime. For the size series of CdSe/CdS shell thicknesses from 4- to 11-monolayer CdS shells, the excitation wavelength dependent PL lifetime normalized to the lifetime of the core is shown. There is an increasing difference between shell and core lifetimes with increasing shell thicknesses.

From this, excitations of the core allow both the electron and hole to quickly relax and predominately localize within the core, leading to faster radiative recombination. However, shell excitations in larger shell thickness samples allow the electron to be more easily trapped at the CdS surface in shallow traps and meanwhile the core-localized hole cannot recombine with the electron, leading to longer lifetimes (Figure 4.19). This effect is not problematic for samples with small shell thicknesses but becomes increasingly present with increasing shell thickness (Figure 4.19). This natural separation of charge carriers is problematic to maximizing the overall optical efficiency of a CdSe/CdS sample and is not present in the 8±0.5ML samples.

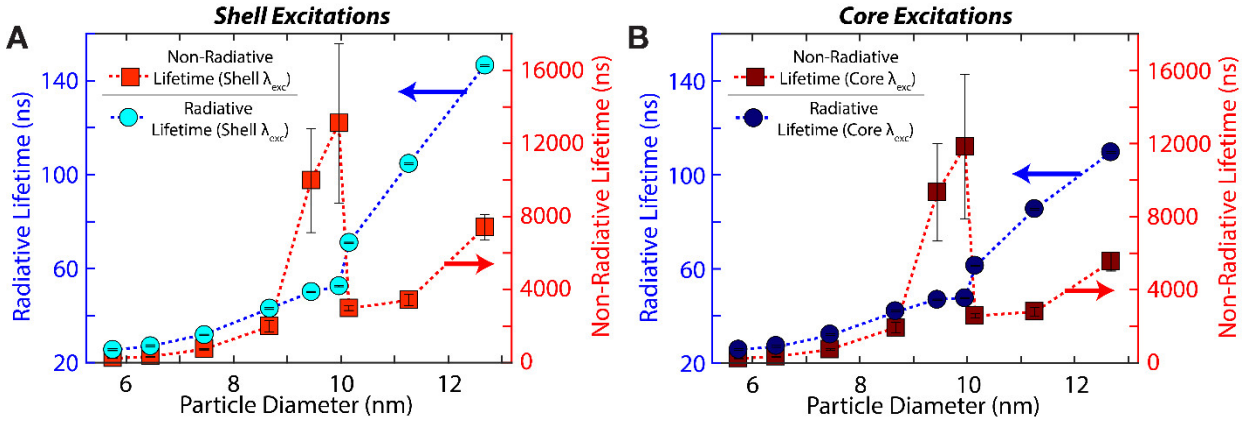

Figure 4.20: Comparison of the radiative and non-radiative lifetimes for the CdSe/CdS series. Extracted non-radiative and radiative lifetimes using a combination of the quantum yield and the average excited state lifetime for (A) shell-based excitations and (B) core-based excitations for each of the CdSe/CdS samples in the size series. Each CdSe/CdS quantum dot ensemble is represented by the average ensemble feret diameter of the ensemble.

While some materials have relatively quick radiative recombination such as the $CsPbX_3$ NCs[43,164], the extended lifetimes of the CdSe/CdS ensembles still have the potential to display PTQYs of 99.6%, suggesting the presence of very slow non-radiative processes, possibly as slow as 2-20 microseconds (Figure 4.20). Impressively, the performance of these materials is comparable to that of rare-earth doped glasses and high-quality passivated thin-films with 99.7%[46] and 99.5%[47] reported quantum yields respectively. This shows that there is no fundamental limitation placed on accessing quantum dots with not only the advantages of high-quality crystalline materials but also the advantages of scalable solution-processed materials. Important to note, measurements with the PTQY technique are on densely packed films, films that can over-sample the lowest efficiency quantum dots in the ensemble. Additionally, efficiencies determined from the shell excitations are lower than the corresponding core excitations due to their natural longer lifetimes. With these considerations in mind, the measurement of a 99.6±0.2% quantum yield further underscores the high quality of these CdSe/CdS quantum dots, promising for the further development of high-efficiency materials.

4.7: Future Directions

It has been shown that colloidal materials can be synthesized that perform as luminophores as efficiently as well-passivated single crystals, but questions remain regarding just how efficient these materials can be. At this point the thermodynamic limit of quantum dot PLQY is not known

and will likely require a concerted effort between experimentalists and theorists. Understanding the upper limits of performance that is achievable in a material system will be very useful for creating a roadmap towards further performance improvements. Synthetically, improvements in both process engineering and characterization as the performance of these materials continues to improve can help to drive the design, synthesis, and understanding of optimized quantum dots. To further this understanding, the influence that individual crystallite defects have on the overall optoelectronic properties of the material is something that has enormous potential and really only becomes possible when there are only a handful of non-interacting defects present in the material. Fully understanding the nature of defects in material systems can help to develop rational methods to overcome their detrimental consequences. Additionally, the PTQY technique can be expanded to optimize different quantum dot systems, including thin film and liquid samples at different temperatures to fully understand these important materials. As the performance improves, these materials offer an appealing platform to test fundamental theories and applications that require materials with near lossless materials, certainly the subject of future work as the performance of these materials improve.

References

1. Kelly, K. L., Coronado, E., Zhao, L. L. & Schatz, G. C. The Optical Properties of Metal Nanoparticles: The Influence of Size, Shape, and Dielectric Environment. *J. Phys. Chem. B* **107**, 668–677 (2003).
2. Murray, C. B., Kagan, C. R. & Bawendi, M. G. Synthesis and Characterization of Monodisperse Nanocrystals and Close-Packed Nanocrystal Assemblies. *Annu. Rev. Mater. Sci.* **30**, 545–610 (2000).
3. Norris, D. J. & Bawendi, M. G. Measurement and assignment of the size-dependent optical spectrum in CdSe quantum dots. *Phys. Rev. B* **53**, 16338–16346 (1996).
4. Kang, M. S., Sahu, A., Norris, D. J. & Frisbie, C. D. Size-Dependent Electrical Transport in CdSe Nanocrystal Thin Films. *Nano Lett.* **10**, 3727–3732 (2010).
5. Ciraci, S., Buldum, A. & Batra, I. P. Quantum effects in electrical and thermal transport through nanowires. *J. Phys. Condens. Matter* **13**, R537–R568 (2001).
6. Park, T.-J., Papaefthymiou, G. C., Viescas, A. J., Moodenbaugh, A. R. & Wong, S. S. Size-Dependent Magnetic Properties of Single-Crystalline Multiferroic $BiFeO_3$ Nanoparticles. *Nano Lett.* **7**, 766–772 (2007).
7. Seo, W. S. *et al.* Size-dependent magnetic properties of colloidal Mn_3O_4 and MnO nanoparticles. *Angew. Chemie - Int. Ed.* **43**, 1115–1117 (2004).
8. Demortière, A. *et al.* Size-dependent properties of magnetic iron oxidenanocrystals. *Nanoscale* **3**, 225–232 (2011).
9. Alivisatos, A. P. Semiconductor Clusters, Nanocrystals, and Quantum Dots. *Science* **271**, 933–937 (1996).
10. Nollet, T. *et al.* Size-Dependent Optical Properties of Colloidal PbS Quantum Dots. *ACS Nano* **3**, 3023–3030 (2009).
11. Mićić, O. I. *et al.* Size-Dependent Spectroscopy of InP Quantum Dots. *J. Phys. Chem. B* **101**, 4904–4912 (1997).
12. Tsuzuki, T. & McCormick, P. G. Synthesis of CdS quantum dots by mechanochemical reaction. *Appl. Phys. A Mater. Sci. Process.* **65**, 607–609 (1997).
13. Lee, L. K. & Ku, P.-C. Fabrication of site-controlled InGaN quantum dots using reactive-ion etching. *Phys. status solidi* **9**, 609–612 (2012).
14. Patra, S., Satpati, B. & Pradhan, S. K. Microstructure characterization of mechanically synthesized ZnS quantum dots. *J. Appl. Phys.* **106**, 034313 (2009).
15. Walavalkar, S. S., Homyk, A. P., Henry, M. D. & Scherer, A. Three-dimensional etching of silicon for the fabrication of low-dimensional and suspended devices. *Nanoscale* **5**, 927 (2013).
16. Bimberg, D. *et al.* Self-organization processes in MBE-grown quantum dot structures. *Thin Solid Films* **267**, 32–36 (1995).
17. Mirin, R. P., Ibbetson, J. P., Nishi, K., Gossard, A. C. & Bowers, J. E. 1.3 μm photoluminescence from InGaAs quantum dots on GaAs. *Appl. Phys. Lett.* **67**, 3795–3797 (1995).
18. Kim, J. Y., Voznyy, O., Zhitomirsky, D. & Sargent, E. H. 25th Anniversary Article: Colloidal Quantum Dot Materials and Devices: A Quarter-Century of Advances. *Adv. Mater.* **25**, 4986–5010 (2013).
19. Zhang, D., Gökce, B. & Barcikowski, S. Laser Synthesis and Processing of Colloids: Fundamentals and Applications. *Chem. Rev.* **117**, 3990–4103 (2017).

20. Pu, Y., Cai, F., Wang, D., Wang, J.-X. & Chen, J.-F. Colloidal Synthesis of Semiconductor Quantum Dots toward Large-Scale Production: A Review. *Ind. Eng. Chem. Res.* **57**, 1790–1802 (2018).
21. Yin, Y. & Alivisatos, A. P. Colloidal nanocrystal synthesis and the organic–inorganic interface. *Nature* **437**, 664–670 (2005).
22. Jin, R., Zeng, C., Zhou, M. & Chen, Y. Atomically Precise Colloidal Metal Nanoclusters and Nanoparticles: Fundamentals and Opportunities. *Chem. Rev.* **116**, 10346–10413 (2016).
23. Kovalenko, M. V., Scheele, M. & Talapin, D. V. Colloidal Nanocrystals with Molecular Metal Chalcogenide Surface Ligands. *Science* **324**, 1417–1420 (2009).
24. Kovalenko, M. V., Bodnarchuk, M. I., Zaumseil, J., Lee, J.-S. & Talapin, D. V. Expanding the Chemical Versatility of Colloidal Nanocrystals Capped with Molecular Metal Chalcogenide Ligands. *J. Am. Chem. Soc.* **132**, 10085–10092 (2010).
25. Nag, A. *et al.* Metal-free Inorganic Ligands for Colloidal Nanocrystals: S^{2-}, HS^{-}, Se^{2-}, HSe^{-}, Te^{2-}, HTe^{-}, TeS_3^{2-}, OH^{-}, and NH^{2-} as Surface Ligands. *J. Am. Chem. Soc.* **133**, 10612–10620 (2011).
26. Bockelmann, U. & Egeler, T. Electron relaxation in quantum dots by means of Auger processes. *Phys. Rev. B* **46**, 15574–15577 (1992).
27. Nozik, A. J. Spectroscopy and Hot Electron Relaxation Dynamics in Semiconductor Quantum Wells and Quantum Dots. *Annu. Rev. Phys. Chem.* **52**, 193–231 (2001).
28. Kambhampati, P. Hot Exciton Relaxation Dynamics in Semiconductor Quantum Dots: Radiationless Transitions on the Nanoscale. *J. Phys. Chem. C* **115**, 22089–22109 (2011).
29. Bockelmann, U. Exciton relaxation and radiative recombination in semiconductor quantum dots. *Phys. Rev. B* **48**, 17637–17640 (1993).
30. Crooker, S. A., Barrick, T., Hollingsworth, J. A. & Klimov, V. I. Multiple temperature regimes of radiative decay in CdSe nanocrystal quantum dots: Intrinsic limits to the dark-exciton lifetime. *Appl. Phys. Lett.* **82**, 2793–2795 (2003).
31. Ellingson, R. J. *et al.* Highly Efficient Multiple Exciton Generation in Colloidal PbSe and PbS Quantum Dots. *Nano Lett.* **5**, 865–871 (2005).
32. Nozik, A. J. Multiple exciton generation in semiconductor quantum dots. *Chem. Phys. Lett.* **457**, 3–11 (2008).
33. Wegh, R. T., Donker, H., Oskam, K. D. & Meijerink, A. Visible Quantum Cutting in $LiGdF_4:Eu^{3+}$ Through Downconversion. *Science* **283**, 663–666 (1999).
34. van der Ende, B. M., Aarts, L. & Meijerink, A. Near-Infrared Quantum Cutting for Photovoltaics. *Adv. Mater.* **21**, 3073–3077 (2009).
35. Milonni, P. W. Why spontaneous emission? *Am. J. Phys.* **52**, 340–343 (1984).
36. van Driel, A. F. *et al.* Frequency-Dependent Spontaneous Emission Rate from CdSe and CdTe Nanocrystals: Influence of Dark States. *Phys. Rev. Lett.* **95**, 236804 (2005).
37. Miyakawa, T. & Dexter, D. L. Phonon Sidebands, Multiphonon Relaxation of Excited States, and Phonon-Assisted Energy Transfer between Ions in Solids. *Phys. Rev. B* **1**, 2961–2969 (1970).
38. Egorov, S. A., Rabani, E. & Berne, B. J. Nonradiative relaxation processes in condensed phases: Quantum versus classical baths. *J. Chem. Phys.* **110**, 5238–5248 (1999).
39. Robinson, J. T. *et al.* Ultrasmall Reduced Graphene Oxide with High Near-Infrared Absorbance for Photothermal Therapy. *J. Am. Chem. Soc.* **133**, 6825–6831 (2011).
40. Neumann, O. *et al.* Solar Vapor Generation Enabled by Nanoparticles. *ACS Nano* **7**, 42–49 (2013).

41. De Nolf, K. *et al.* Binding and Packing in Two-Component Colloidal Quantum Dot Ligand Shells: Linear versus Branched Carboxylates. *J. Am. Chem. Soc.* **139**, 3456–3464 (2017).
42. Chen, O. *et al.* Compact high-quality CdSe-CdS core-shell nanocrystals with narrow emission linewidths and suppressed blinking. *Nat. Mater.* **12**, 445–51 (2013).
43. Koscher, B. A., Swabeck, J. K., Bronstein, N. D. & Alivisatos, A. P. Essentially Trap-Free CsPbBr3 Colloidal Nanocrystals by Postsynthetic Thiocyanate Surface Treatment. *J. Am. Chem. Soc.* **139**, 6566–6569 (2017).
44. Nenon, D. P. *et al.* Design Principles for Trap-Free CsPbX 3 Nanocrystals: Enumerating and Eliminating Surface Halide Vacancies with Softer Lewis Bases. *J. Am. Chem. Soc.* **140**, 17760–17772 (2018).
45. Hanifi, D. A. *et al.* Redefining near-unity luminescence in quantum dots with photothermal threshold quantum yield. *Science* **363**, 1199–1202 (2019).
46. Kushida, T. & Geusic, J. E. Optical Refrigeration in Nd-Doped Yttrium Aluminum Garnet. *Phys. Rev. Lett.* **21**, 1172–1175 (1968).
47. Schnitzer, I., Yablonovitch, E., Caneau, C. & Gmitter, T. J. Ultrahigh spontaneous emission quantum efficiency, 99.7% internally and 72% externally, from AlGaAs/GaAs/AlGaAs double heterostructures. *Appl. Phys. Lett.* **62**, 131–133 (1993).
48. Kwon, S. G. & Hyeon, T. Formation Mechanisms of Uniform Nanocrystals via Hot-Injection and Heat-Up Methods. *Small* **7**, 2685–2702 (2011).
49. Yin, Y. Formation of Hollow Nanocrystals Through the Nanoscale Kirkendall Effect. *Science* **304**, 711–714 (2004).
50. Wang, W., Dahl, M. & Yin, Y. Hollow Nanocrystals through the Nanoscale Kirkendall Effect. *Chem. Mater.* **25**, 1179–1189 (2013).
51. Sun, Y. & Xia, Y. Alloying and Dealloying Processes Involved in the Preparation of Metal Nanoshells through a Galvanic Replacement Reaction. *Nano Lett.* **3**, 1569–1572 (2003).
52. Zhang, H. *et al.* Synthesis of Pd−Pt Bimetallic Nanocrystals with a Concave Structure through a Bromide-Induced Galvanic Replacement Reaction. *J. Am. Chem. Soc.* **133**, 6078–6089 (2011).
53. Son, D. H. Cation Exchange Reactions in Ionic Nanocrystals. *Science* **306**, 1009–1012 (2004).
54. Rivest, J. B. & Jain, P. K. Cation exchange on the nanoscale: An emerging technique for new material synthesis, device fabrication, and chemical sensing. *Chem. Soc. Rev.* **42**, 89–96 (2013).
55. Koscher, B. A., Bronstein, N. D., Olshansky, J. H., Bekenstein, Y. & Alivisatos, A. P. Surface- vs Diffusion-Limited Mechanisms of Anion Exchange in $CsPbBr_3$ Nanocrystal Cubes Revealed through Kinetic Studies. *J. Am. Chem. Soc.* **138**, 12065–12068 (2016).
56. Baumann, S. F., Brindley, P. K. & Smith, S. D. Reaction zone microstructure in a Ti_3Al + Nb/SiC composite. *Metall. Trans. A* **21**, 1559–1569 (1990).
57. Rai, A., Park, K., Zhou, L. & Zachariah, M. R. Understanding the mechanism of aluminium nanoparticle oxidation. *Combust. Theory Model.* **10**, 843–859 (2006).
58. Helfferich, F. Ion-Exchange Kinetics. V. Ion Exchange Accompanied by Reactions. *J. Phys. Chem.* **69**, 1178–1187 (1965).
59. Beberwyck, B. J. & Alivisatos, A. P. Ion Exchange Synthesis of III–V Nanocrystals. *J. Am. Chem. Soc.* **134**, 19977–19980 (2012).
60. Beberwyck, B. J., Surendranath, Y. & Alivisatos, A. P. Cation exchange: A versatile tool for nanomaterials synthesis. *J. Phys. Chem. C* **117**, 19759–19770 (2013).

61. Luther, J. M., Zheng, H., Sadtler, B. & Alivisatos, A. P. Synthesis of PbS Nanorods and Other Ionic Nanocrystals of Complex Morphology by Sequential Cation Exchange Reactions. *J. Am. Chem. Soc.* **131**, 16851–16857 (2009).
62. Pietryga, J. M. *et al.* Utilizing the Lability of Lead Selenide to Produce Heterostructured Nanocrystals with Bright, Stable Infrared Emission. *J. Am. Chem. Soc.* **130**, 4879–4885 (2008).
63. van der Stam, W. *et al.* Luminescent $CuInS_2$ Quantum Dots by Partial Cation Exchange in $Cu_{2-x}S$ Nanocrystals. *Chem. Mater.* **27**, 621–628 (2015).
64. De Trizio, L. *et al.* $Cu_{3-x}P$ Nanocrystals as a Material Platform for Near-Infrared Plasmonics and Cation Exchange Reactions. *Chem. Mater.* **27**, 1120–1128 (2015).
65. Routzahn, A. L. & Jain, P. K. Single-Nanocrystal Reaction Trajectories Reveal Sharp Cooperative Transitions. *Nano Lett.* **14**, 987–992 (2014).
66. Park, J., Zheng, H., Jun, Y. & Alivisatos, A. P. Hetero-Epitaxial Anion Exchange Yields Single-Crystalline Hollow Nanoparticles. *J. Am. Chem. Soc.* **131**, 13943–13945 (2009).
67. Song, J. *et al.* Quantum Dot Light-Emitting Diodes Based on Inorganic Perovskite Cesium Lead Halides ($CsPbX_3$). *Adv. Mater.* **27**, 7162–7167 (2015).
68. Swarnkar, A. *et al.* Colloidal $CsPbBr_3$ Perovskite Nanocrystals: Luminescence beyond Traditional Quantum Dots. *Angew. Chemie Int. Ed.* **54**, 15424–15428 (2015).
69. Protesescu, L. *et al.* Nanocrystals of Cesium Lead Halide Perovskites (CsPbX 3 , X = Cl, Br, and I): Novel Optoelectronic Materials Showing Bright Emission with Wide Color Gamut. *Nano Lett.* **15**, 3692–3696 (2015).
70. Liu, Y., Xiao, H. & Goddard, W. A. Two-Dimensional Halide Perovskites: Tuning Electronic Activities of Defects. *Nano Lett.* **16**, 3335–3340 (2016).
71. ten Brinck, S. & Infante, I. Surface Termination, Morphology, and Bright Photoluminescence of Cesium Lead Halide Perovskite Nanocrystals. *ACS Energy Lett.* **1**, 1266–1272 (2016).
72. Manser, J. S., Christians, J. A. & Kamat, P. V. Intriguing Optoelectronic Properties of Metal Halide Perovskites. *Chem. Rev.* **116**, 12956–13008 (2016).
73. Sharma, S., Weiden, N. & Weiss, A. Phase Diagrams of Quasibinary Systems of the Type: ABX 3 — A′BX 3 ; ABX 3 — AB′X 3 , and ABX 3 — ABX′ 3 ; X = Halogen. *Zeitschrift für Phys. Chemie* **175**, 63–80 (1992).
74. Akkerman, Q. A. *et al.* Tuning the Optical Properties of Cesium Lead Halide Perovskite Nanocrystals by Anion Exchange Reactions. *J. Am. Chem. Soc.* **137**, 10276–10281 (2015).
75. Nedelcu, G. *et al.* Fast Anion-Exchange in Highly Luminescent Nanocrystals of Cesium Lead Halide Perovskites ($CsPbX_3$, X = Cl, Br, I). *Nano Lett.* **15**, 5635–5640 (2015).
76. Katan, C., Mercier, N. & Even, J. Quantum and Dielectric Confinement Effects in Lower-Dimensional Hybrid Perovskite Semiconductors. *Chem. Rev.* **119**, 3140–3192 (2019).
77. Mizusaki, J., Aria, K. & Fueki, K. Ionic conduction of the perovskite-type halides. *Solid State Ionics* **11**, 203–211 (1983).
78. Yang, T.-Y., Gregori, G., Pellet, N., Grätzel, M. & Maier, J. The Significance of Ion Conduction in a Hybrid Organic-Inorganic Lead-Iodide-Based Perovskite Photosensitizer. *Angew. Chemie Int. Ed.* **54**, 7905–7910 (2015).
79. Bekenstein, Y., Koscher, B. A., Eaton, S. W., Yang, P. & Alivisatos, A. P. Highly Luminescent Colloidal Nanoplates of Perovskite Cesium Lead Halide and Their Oriented Assemblies. *J. Am. Chem. Soc.* **137**, 16008–16011 (2015).
80. Creutz, S. E., Crites, E. N., De Siena, M. C. & Gamelin, D. R. Anion Exchange in Cesium

Lead Halide Perovskite Nanocrystals and Thin Films Using Trimethylsilyl Halide Reagents. *Chem. Mater.* **30**, 4887–4891 (2018).
81. Park, Y. S., Guo, S., Makarov, N. S. & Klimov, V. I. Room Temperature Single-Photon Emission from Individual Perovskite Quantum Dots. *ACS Nano* **9**, 10386–10393 (2015).
82. Dastidar, S. *et al.* High Chloride Doping Levels Stabilize the Perovskite Phase of Cesium Lead Iodide. *Nano Lett.* **16**, 3563–3570 (2016).
83. Nagabhushana, G. P., Shivaramaiah, R. & Navrotsky, A. Direct calorimetric verification of thermodynamic instability of lead halide hybrid perovskites. *Proc. Natl. Acad. Sci.* **113**, 7717–7721 (2016).
84. Lai, M. *et al.* Intrinsic anion diffusivity in lead halide perovskites is facilitated by a soft lattice. *Proc. Natl. Acad. Sci.* **115**, 11929–11934 (2018).
85. Pellet, N., Teuscher, J., Maier, J. & Grätzel, M. Transforming Hybrid Organic Inorganic Perovskites by Rapid Halide Exchange. *Chem. Mater.* **27**, 2181–2188 (2015).
86. Anderson, B. D. & Tracy, J. B. Nanoparticle conversion chemistry: Kirkendall effect, galvanic exchange, and anion exchange. *Nanoscale* **6**, 12195–12216 (2014).
87. Helfferich, F. G. *Kinetics of Multistep Reactions, 2nd ed.; Green, N. J. B., Ed.; Comprehensive Chemical Kinetics 40*. (Elsevier, 2004).
88. Ravi, V. K., Markad, G. B. & Nag, A. Band Edge Energies and Excitonic Transition Probabilities of Colloidal CsPbX 3 (X = Cl, Br, I) Perovskite Nanocrystals. *ACS Energy Lett.* **3**, 665–671 (2016).
89. Hu, F. *et al.* Superior Optical Properties of Perovskite Nanocrystals as Single Photon Emitters. *ACS Nano* **9**, 12410–12416 (2015).
90. Liu, M., Johnston, M. B. & Snaith, H. J. Efficient planar heterojunction perovskite solar cells by vapour deposition. *Nature* **501**, 395–398 (2013).
91. Jeon, N. J. *et al.* Compositional engineering of perovskite materials for high-performance solar cells. *Nature* **517**, 476–480 (2015).
92. Dou, L. *et al.* Solution-processed hybrid perovskite photodetectors with high detectivity. *Nat. Commun.* **5**, 5404 (2014).
93. Fang, Y. & Huang, J. Resolving weak light of sub-picowatt per square centimeter by hybrid perovskite photodetectors enabled by noise reduction. *Adv. Mater.* **27**, 2804–2810 (2015).
94. Wang, J. *et al.* Interfacial Control Toward Efficient and Low-Voltage Perovskite Light-Emitting Diodes. *Adv. Mater.* **27**, 2311–2316 (2015).
95. Jaramillo-Quintero, O. A., Sanchez, R. S., Rincon, M. & Mora-Sero, I. Bright Visible-Infrared Light Emitting Diodes Based on Hybrid Halide Perovskite with Spiro-OMeTAD as a Hole-Injecting Layer. *J. Phys. Chem. Lett.* **6**, 1883–1890 (2015).
96. Kang, J. & Wang, L.-W. High Defect Tolerance in Lead Halide Perovskite $CsPbBr_3$. *J. Phys. Chem. Lett.* **8**, 489–493 (2017).
97. Pan, J. *et al.* Highly Efficient Perovskite-Quantum-Dot Light-Emitting Diodes by Surface Engineering. *Adv. Mater.* **28**, 8718–8725 (2016).
98. Kim, Y. *et al.* Efficient Luminescence from Perovskite Quantum Dot Solids. *ACS Appl. Mater. Interfaces* **7**, 25007–25013 (2015).
99. Wehrenfennig, C., Liu, M., Snaith, H. J., Johnston, M. B. & Herz, L. M. Homogeneous Emission Line Broadening in the Organo Lead Halide Perovskite $CH_3NH_3PbI_{3-x}Cl_x$. *J. Phys. Chem. Lett.* **5**, 1300–1306 (2014).
100. De Roo, J. *et al.* Highly Dynamic Ligand Binding and Light Absorption Coefficient of Cesium Lead Bromide Perovskite Nanocrystals. *ACS Nano* **10**, 2071–2081 (2016).

101. Moreels, I. *et al.* Size-tunable, bright, and stable PbS quantum dots: A surface chemistry study. *ACS Nano* **5**, 2004–2012 (2011).
102. Moyen, E., Jun, H., Kim, H. & Jang, J. Surface Engineering of Room Temperature-Grown Inorganic Perovskite Quantum Dots for Highly Efficient Inverted Light-Emitting Diodes. *ACS Appl. Mater. Interfaces* **10**, 42647–42656 (2018).
103. Tan, Y. *et al.* Highly Luminescent and Stable Perovskite Nanocrystals with Octylphosphonic Acid as a Ligand for Efficient Light-Emitting Diodes. *ACS Appl. Mater. Interfaces* **10**, 3784–3792 (2018).
104. Di Stasio, F., Christodoulou, S., Huo, N. & Konstantatos, G. Near-Unity Photoluminescence Quantum Yield in $CsPbBr_3$ Nanocrystal Solid-State Films via Postsynthesis Treatment with Lead Bromide. *Chem. Mater.* **29**, 7663–7667 (2017).
105. Ahmed, T., Seth, S. & Samanta, A. Boosting the Photoluminescence of CsPbX3 (X = Cl, Br, I) Perovskite Nanocrystals Covering a Wide Wavelength Range by Postsynthetic Treatment with Tetrafluoroborate Salts. *Chem. Mater.* **30**, 3633–3637 (2018).
106. Yoon, J. *et al.* GaAs photovoltaics and optoelectronics using releasable multilayer epitaxial assemblies. *Nature* **465**, 329–333 (2010).
107. Yablonovitch, E., Gmitter, T., Harbison, J. P. & Bhat, R. Extreme selectivity in the lift-off of epitaxial GaAs films. *Appl. Phys. Lett.* **51**, 2222–2224 (2012).
108. Liu, Z. *et al.* Ligand Mediated Transformation of Cesium Lead Bromide Perovskite Nanocrystals to Lead Depleted Cs_4PbBr_6 Nanocrystals. *J. Am. Chem. Soc.* **139**, 5309–5312 (2017).
109. Udayabhaskararao, T. *et al.* A Mechanistic Study of Phase Transformation in Perovskite Nanocrystals Driven by Ligand Passivation. *Chem. Mater.* **30**, 84–93 (2018).
110. Cottingham, P. & Brutchey, R. L. On the crystal structure of colloidally prepared $CsPbBr_3$ quantum dots. *Chem. Commun.* **52**, 5246–5249 (2016).
111. Ravi, V. K. *et al.* Origin of the Substitution Mechanism for the Binding of Organic Ligands on the Surface of $CsPbBr_3$ Perovskite Nanocubes. *J. Phys. Chem. Lett.* **8**, 4988–4994 (2017).
112. Fafarman, A. T. *et al.* Thiocyanate-Capped Nanocrystal Colloids: Vibrational Reporter of Surface Chemistry and Solution-Based Route to Enhanced Coupling in Nanocrystal Solids. *J. Am. Chem. Soc.* **133**, 15753–15761 (2011).
113. Wang, Q. *et al.* Scaling behavior of moisture-induced grain degradation in polycrystalline hybrid perovskite thin films. *Energy Environ. Sci.* **10**, 516–522 (2017).
114. Son, D. *et al.* Self-formed grain boundary healing layer for highly efficient $CH_3NH_3PbI_3$ perovskite solar cells. *Nat. Energy* **1**, 16081 (2016).
115. Merdasa, A. *et al.* Super-Resolution Luminescence Microspectroscopy Reveals the Mechanism of Photoinduced Degradation in $CH_3NH_3PbI_3$ Perovskite Nanocrystals. *J. Phys. Chem. C* **120**, 10711–10719 (2016).
116. Hauwiller, M. R. *et al.* Unraveling Kinetically-Driven Mechanisms of Gold Nanocrystal Shape Transformations Using Graphene Liquid Cell Electron Microscopy. *Nano Lett.* **18**, 5731–5737 (2018).
117. Ye, X. *et al.* Single-particle mapping of nonequilibrium nanocrystal transformations. *Science* **354**, 874–877 (2016).
118. Lewis, L. N. On the mechanism of metal colloid catalyzed hydrosilylation: proposed explanations for electronic effects and oxygen cocatalysis. *J. Am. Chem. Soc.* **112**, 5998–6004 (1990).

119. Aoyagi, Y. *et al.* Molecular layer etching of GaAs. *Appl. Phys. Lett.* **60**, 968–970 (1992).
120. Pearson, R. G. Hard and soft acids and bases, HSAB, part 1: Fundamental principles. *J. Chem. Educ.* **45**, 581 (1968).
121. Dong, A. *et al.* A Generalized Ligand-Exchange Strategy Enabling Sequential Surface Functionalization of Colloidal Nanocrystals. *J. Am. Chem. Soc.* **133**, 998–1006 (2011).
122. Brown, P. R. *et al.* Energy Level Modification in Lead Sulfide Quantum Dot Thin Films through Ligand Exchange. *ACS Nano* **8**, 5863–5872 (2014).
123. Magde, D., Wong, R. & Seybold, P. G. Fluorescence Quantum Yields and Their Relation to Lifetimes of Rhodamine 6G and Fluorescein in Nine Solvents: Improved Absolute Standards for Quantum Yields¶. *Photochem. Photobiol.* **75**, 327 (2002).
124. Resch-Genger, U., Grabolle, M., Cavaliere-Jaricot, S., Nitschke, R. & Nann, T. Quantum dots versus organic dyes as fluorescent labels. *Nat. Methods* **5**, 763–775 (2008).
125. Wilson, L. R. & Richards, B. S. Measurement method for photoluminescent quantum yields of fluorescent organic dyes in polymethyl methacrylate for luminescent solar concentrators. *Appl. Opt.* **48**, 212 (2009).
126. Zhang, Y. *et al.* Molecular Oxygen Induced in-Gap States in PbS Quantum Dots. *ACS Nano* **9**, 10445–10452 (2015).
127. Nagpal, P. & Klimov, V. I. Role of mid-gap states in charge transport and photoconductivity in semiconductor nanocrystal films. *Nat. Commun.* **2**, 486 (2011).
128. Zherebetskyy, D. & Wang, L.-W. In-Gap States in Electronic Structure of Nonpolar Surfaces of Insulating Metal Oxides. *Adv. Mater. Interfaces* **1**, 1300131 (2014).
129. Kairdolf, B. A. *et al.* Semiconductor Quantum Dots for Bioimaging and Biodiagnostic Applications. *Annu. Rev. Anal. Chem.* **6**, 143–162 (2013).
130. Hong, G. *et al.* In Vivo Fluorescence Imaging with Ag_2S Quantum Dots in the Second Near-Infrared Region. *Angew. Chemie Int. Ed.* **51**, 9818–9821 (2012).
131. Shirasaki, Y., Supran, G. J., Bawendi, M. G. & Bulović, V. Emergence of colloidal quantum-dot light-emitting technologies. *Nat. Photonics* **7**, 13–23 (2013).
132. Wu, Y.-R., Lin, Y.-Y., Huang, H.-H. & Singh, J. Electronic and optical properties of InGaN quantum dot based light emitters for solid state lighting. *J. Appl. Phys.* **105**, 013117 (2009).
133. Baek, J., Allen, P. M., Bawendi, M. G. & Jensen, K. F. Investigation of indium phosphide nanocrystal synthesis using a high-temperature and high-pressure continuous flow microreactor. *Angew. Chemie - Int. Ed.* **50**, 627–630 (2011).
134. Zhang, F. *et al.* Brightly Luminescent and Color-Tunable Colloidal $CH_3NH_3PbX_3$ (X = Br, I, Cl) Quantum Dots: Potential Alternatives for Display Technology. *ACS Nano* **9**, 4533–4542 (2015).
135. Sheik-Bahae, M. & Epstein, R. I. Optical refrigeration. *Nat. Photonics* **1**, 693–699 (2007).
136. Zhang, S., Zhukovskyi, M., Janko, B. & Kuno, M. K. Evaluation of $CsPbBr_3$ nanocrystals for laser cooling. in *Photonic Heat Engines: Science and Applications* (eds. Epstein, R. I., Seletskiy, D. V. & Sheik-Bahae, M.) **1093604**, 3 (SPIE, 2019).
137. Lenert, A. *et al.* A nanophotonic solar thermophotovoltaic device. *Nat. Nanotechnol.* **9**, 126–130 (2014).
138. Licciulli, A. *et al.* The challenge of high-performance selective emitters for thermophotovoltaic applications. *Semicond. Sci. Technol.* **18**, S174–S183 (2003).
139. Zhong, T. *et al.* Nanophotonic rare-earth quantum memory with optically controlled retrieval. *Science* **357**, 1392–1395 (2017).
140. Xiao, T. P., Chen, K., Santhanam, P., Fan, S. & Yablonovitch, E. Electroluminescent

refrigeration by ultra-efficient GaAs light-emitting diodes. *J. Appl. Phys.* **123**, 173104 (2018).
141. Gutierrez, G. D., Coropceanu, I., Bawendi, M. G. & Swager, T. M. A Low Reabsorbing Luminescent Solar Concentrator Employing π-Conjugated Polymers. *Adv. Mater.* **28**, 497–501 (2016).
142. Needell, D. R. *et al.* Design Criteria for Micro-Optical Tandem Luminescent Solar Concentrators. *IEEE J. Photovoltaics* **8**, 1560–1567 (2018).
143. Bronstein, N. D. *et al.* Quantum Dot Luminescent Concentrator Cavity Exhibiting 30-fold Concentration. *ACS Photonics* **2**, 1576–1583 (2015).
144. Meinardi, F. *et al.* Highly efficient large-area colourless luminescent solar concentrators using heavy-metal-free colloidal quantum dots. *Nat. Nanotechnol.* **10**, 878–885 (2015).
145. Song, H.-J. *et al.* Performance Limits of Luminescent Solar Concentrators Tested with Seed/Quantum-Well Quantum Dots in a Selective-Reflector-Based Optical Cavity. *Nano Lett.* **18**, 395–404 (2018).
146. Klimov, V. I., Baker, T. A., Lim, J., Velizhanin, K. A. & McDaniel, H. Quality Factor of Luminescent Solar Concentrators and Practical Concentration Limits Attainable with Semiconductor Quantum Dots. *ACS Photonics* **3**, 1138–1148 (2016).
147. Yablonovitch, E. Thermodynamics of the fluorescent planar concentrator. *J. Opt. Soc. Am.* **70**, 1362 (1980).
148. Bronstein, N. D. *et al.* Luminescent solar concentration with semiconductor nanorods and transfer-printed micro-silicon solar cells. *ACS Nano* **8**, 44–53 (2014).
149. Peng, X. *et al.* Shape control of CdSe nanocrystals. *Nature* **404**, 59–61 (2000).
150. Shieh, F., Saunders, A. E. & Korgel, B. A. General Shape Control of Colloidal CdS, CdSe, CdTe Quantum Rods and Quantum Rod Heterostructures. *J. Phys. Chem. B* **109**, 8538–8542 (2005).
151. Christodoulou, S. *et al.* Synthesis of highly luminescent wurtzite CdSe/CdS giant-shell nanocrystals using a fast continuous injection route. *J. Mater. Chem. C* **2**, 3439 (2014).
152. Htoon, H. *et al.* Highly Emissive Multiexcitons in Steady-State Photoluminescence of Individual "Giant" CdSe/CdS Core/Shell Nanocrystals. *Nano Lett.* **10**, 2401–2407 (2010).
153. Chen, Y. *et al.* "Giant" Multishell CdSe Nanocrystal Quantum Dots with Suppressed Blinking. *J. Am. Chem. Soc.* **130**, 5026–5027 (2008).
154. Carbone, L. *et al.* Synthesis and Micrometer-Scale Assembly of Colloidal CdSe/CdS Nanorods Prepared by a Seeded Growth Approach. *Nano Lett.* **7**, 2942–2950 (2007).
155. Bronstein, N. D. Material and Optical Design Rules for High Performance Luminescent Solar Concentrators. *UC Berkeley Electronic Theses and Dissertations* (2015).
156. Voznyy, O. Mobile Surface Traps in CdSe Nanocrystals with Carboxylic Acid Ligands. *J. Phys. Chem. C* **115**, 15927–15932 (2011).
157. Hassinen, A. *et al.* Short-Chain Alcohols Strip X-Type Ligands and Quench the Luminescence of PbSe and CdSe Quantum Dots, Acetonitrile Does Not. *J. Am. Chem. Soc.* **134**, 20705–20712 (2012).
158. Anderson, N. C., Hendricks, M. P., Choi, J. J. & Owen, J. S. Ligand Exchange and the Stoichiometry of Metal Chalcogenide Nanocrystals: Spectroscopic Observation of Facile Metal-Carboxylate Displacement and Binding. *J. Am. Chem. Soc.* **135**, 18536–18548 (2013).
159. Jones, M., Lo, S. S. & Scholes, G. D. Quantitative modeling of the role of surface traps in CdSe/CdS/ZnS nanocrystal photoluminescence decay dynamics. *Proc. Natl. Acad. Sci.* **106**,

3011–3016 (2009).
160. Jackson, W. B., Amer, N. M., Boccara, A. C. & Fournier, D. Photothermal deflection spectroscopy and detection. *Appl. Opt.* **20**, 1333 (1981).
161. Buchaca-Domingo, E. *et al.* Direct Correlation of Charge Transfer Absorption with Molecular Donor:Acceptor Interfacial Area via Photothermal Deflection Spectroscopy. *J. Am. Chem. Soc.* **137**, 5256–5259 (2015).
162. Montanarella, F., Biondi, M., Hinterding, S. O. M., Vanmaekelbergh, D. & Rabouw, F. T. Reversible Charge-Carrier Trapping Slows Förster Energy Transfer in CdSe/CdS Quantum-Dot Solids. *Nano Lett.* **18**, 5867–5874 (2018).
163. Rabouw, F. T. *et al.* Delayed Exciton Emission and Its Relation to Blinking in CdSe Quantum Dots. *Nano Lett.* **15**, 7718–7725 (2015).
164. Becker, M. A. *et al.* Bright triplet excitons in caesium lead halide perovskites. *Nature* **553**, 189–193 (2018).